ESPOO 2007 VTT PUBLICATIONS 666

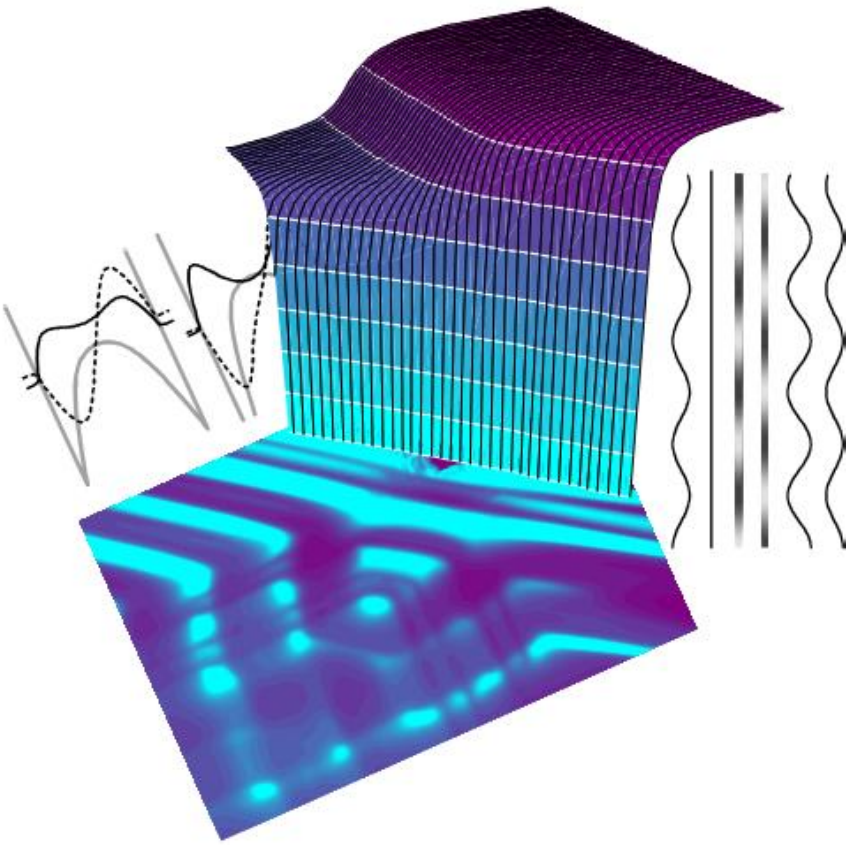

Mika Prunnila

Single and many-band effects in electron transport and energy relaxation in semiconductors

VTT PUBLICATIONS 666

Single and many-band effects in electron transport and energy relaxation in semiconductors

Mika Prunnila

Dissertation for the degree of Doctor of Science in Technology to be presented with due permission of the Department of Electrical and Communications Engineering for public examination and debate in Large Seminar Hall of Micronova at Helsinki University of Technology (Espoo, Finland) on the 19th of December, 2007, at 12 o'clock noon.

ISBN 978-951-38-7065-2 (soft back ed.)
ISSN 1235-0621 (soft back ed.)

ISBN 978-951-38-7066-9 (URL: http://www.vtt.fi/publications/index.jsp)
ISSN 1455-0849 (URL: http://www.vtt.fi/publications/index.jsp)

Copyright © VTT 2007

JULKAISIJA – UTGIVARE – PUBLISHER

VTT, Vuorimiehentie 3, PL 1000, 02044 VTT
puh. vaihde 020 722 111, faksi 020 722 4374

VTT, Bergsmansvägen 3, PB 1000, 02044 VTT
tel. växel 020 722 111, fax 020 722 4374

VTT Technical Research Centre of Finland, Vuorimiehentie 3, P.O. Box 1000, FI-02044 VTT, Finland
phone internat. +358 20 722 111, fax + 358 20 722 4374

VTT, Tietotie 3, PL 1000, 02044 VTT
puh. vaihde 020 722 111, faksi 020 722 7012

VTT, Datavägen 3, PB 1000, 02044 VTT
tel. växel 020 722 111, fax 020 722 7012

VTT Technical Research Centre of Finland, Tietotie 3, P.O. Box 1000, FI-02044 VTT, Finland
phone internat. +358 20 722 111, fax +358 20 722 7012

Edita Prima Oy, Helsinki 2007

Prunnila, Mika. Single and many-band effects in electron transport and energy relaxation in semiconductors [Yhden ja monen vyön ilmiöitä sähkönkuljetuksessa ja elektronien energia-relaksaatiossa puolijohteissa]. Espoo 2007. VTT Publications 666. 68 p. + app. 49 p.

Keywords two-dimensional electron gas, mobility, many-valley systems, electron-phonon interaction, SOI

Abstract

In this Thesis different aspects of band degree of freedom are explored in 2D electron transport and electron-phonon (*e-ph*) energy relaxation in 2D and 3D electron systems. Here the bands of interest are the conduction band valleys of many-valley semiconductors and spatial sub-bands of two-dimensional-electron gas in a quantum well.

The experimental studies of electronic transport focus on double-gate SiO_2-Si-SiO_2 quantum well field-effect-transistors (FETs), which are fabricated utilizing silicon-on-insulator structures and wafer bonding. Double-gate FETs are intensively explored at the moment due to their prospects in microelectronics. The inclusion of a back gate electrode provides means to adjust the electron wave functions and the occupancy of the spatial 2D sub-bands. The contrast between single and two-sub-band transport is studied in low temperature conductivity/mobility and magneto transport. For example, the conductivity shows significant drop at the threshold of the second spatial sub-band due to inter-sub-band coupling and sub-band delocalization effect is observed at symmetric well potential. At room temperature several sub-bands are inevitably populated and the most relevant observed effect is the mobility enhancement towards symmetric quantum well potential. This mobility enhancement is one of the benefits of double-gate FETs in comparison to similar single-gate FETs.

In the studies of *e-ph* energy relaxation we focus on the case where the phonons cannot directly couple the bands of the electron system. If the e-ph matrix elements depend on the band index then the band degree of freedom plays an important role. We developed a mean field theory, which allows elastic inter and intra-band scattering and also Coulomb interaction. Our model reproduces the long wavelength single-band energy loss rate results found in the literature. In the multi-band regime we find a set of new results, which suggest that the energy loss rate is strongly enhanced if the phonons couple asymmetrically to different bands and the single-band interaction is strongly screened. The effect is tested experimentally in heavily doped n-type Si samples by low temperature heating experiments. We find good agreement between the theory and experiment. Our findings enable a design of a novel electron-phonon heat switch.

Prunnila, Mika. Single and many-band effects in electron transport and energy relaxation in semiconductors [Yhden ja monen vyön ilmiöitä sähkönkuljetuksessa ja elektronien energiarelaksaatiossa puolijohteissa]. Espoo 2007. VTT Publications 666. 68 s. + liitt. 49 s.

Avainsanat two-dimensional electron gas, mobility, many-valley systems, electron-phonon interaction, SOI

Tiivistelmä

Työssä tutkitaan elektronien energiavöistä aiheutuvan vapausasteen vaikutuksia 2D-kuljetusilmiöissä ja elektroni-fononi (*e-ph*) -energiarelaksaatiossa 2D- ja 3D-elektronikaasuissa. Tutkimukset keskittyvät lähinnä johtovyön laaksoihin monen vyön puolijohteissa sekä kvanttikaivojen 2D-alivöihin.

Kuljetusilmiöiden kokeelliset tutkimukset keskittyvät erityisesti SiO_2-Si-SiO_2-kvanttikaivoon perustuvaan kenttäefektitransistoriin (FET), jossa on kaksi hilaelektrodia ja joka on valmistettu SOI-kiekolle suoraliittämistekniikalla. Kaksoishilalliset FET-komponentit ovat tällä hetkellä suuren mielenkiinnon kohteena johtuen niiden potentiaalisista sovelluksista mikroelektroniikassa. Nämä komponentit ovat myös erinomaisia 2D-kuljetusilmiöiden laboratorioita, sillä kaksi hilaa mahdollistavat spatiaalisten alivöiden ja elektronien aaltofunktioiden sähköisen kontrollin. Työssä tutkitaan yhden ja kahden alivyön efektejä matalissa lämpötiloissa. Alivöiden välinen kytkentä heijastuu voimakkaasti Si-kvanttikaivon johtavuuteen ja galvanomagneettisiin kuljetuskertoimiin. Huoneen lämpötilassa useat alivyöt ovat miehitettyinä, ja oleellisin havaittu ilmiö on kokonaisliikkuvuuden kasvaminen, kun kvanttikaivon efektiivinen potentiaali asetetaan symmetriseksi ulkoisilla hiloilla. Havaittu liikkuvuuden kasvaminen on yksi ominaisuus, joka tekee tutkituista FET-rakenteista houkuttelevia sovellusten kannalta.

Elektronien energiarelaksaatiossa tutkimme tapausta, jossa fononit eivät kytke elektronikaasun vöitä. Tällöin vyöindeksillä on merkitystä vain, jos *e-ph*-matriisielementit riippuvat vyöindeksistä. Väitöskirjassa kehitetään *e-ph*-energiarelaksaatioteoria, joka sallii vöiden sisäisen ja vöiden välisen elastisen sironnan sekä varauksenkuljettajien välisen vuorovaikutuksen. Tämä teoria antaa erikoistapauksena kirjallisuudessa esiintyvät yhden vyön tapaukset. Monen vyön tapauksessa havaitaan *e-ph*-relaksaation voimakas kasvu, jos fononit kytkeytyvät asymmetrisesti eri vöihin ja yhdenvyönkytkentä on voimakkaasti varjostettu. Teoriaa testataan kokeellisesti n-tyyppisesti seostetussa piissä lämmittämällä elektroneja matalissa lämpötiloissa. Teoria ja kokeet antavat yhtenevän lämpötilavasteen elektroneille. Löydökset mahdollistavat esimerkiksi uudentyyppisen lämpökytkimen suunnittelun.

Preface

This Thesis consists of a selection of my publications and an overview part, where I view these publications under common title. The work has been carried out during the period 2003 - 2007 at VTT (Technical Research Centre of Finland) in Espoo, Finland. This work was initiated at the Microelectronics division of VTT Information Technology. At the end of 2005 VTT Microelectronics was "split" into few units and as a result I finished my Thesis at the VTT Micro and Nanoelectronics (MAN) centre. This work has been partially funded by the GETA graduate school, the Academy of Finland and EU. VTT is acknowledged for internal funding.

First of all, I wish to thank the Instructor Prof. Jouni Ahopelto for his guidance and support. I also would like to thank him for introducing the world of semiconductors and microelectronics to me. This Thesis is a result of collaboration, and I wish to thank the co-authors of the appended papers, Francisco Gamiz, Kimmo Henttinen, Pasi Kivinen, Hiroyuki Sakaki, Alexander Savin, and Päivi Törmä for fruitful collaboration. Professor Hiroyuki Sakaki and Prof. Francisco Gamiz are also acknowledged for their great hospitality during my visits in their research groups in Tokyo and Granada, respectively. The Supervisor Prof. Jukka Tulkki is acknowledged for valuable comments on the manuscript of the overview part and also for helping with many practical issues related to doctoral dissertation.

I would like to thank the Nanoelectronics team (at VTT MAN), Sanna Arpiainen, Tomi Haatainen, Jani Kivioja, Merja Markkanen, Tapio Mäkelä and our team leader Päivi Majander for help and support. I especially wish to acknowledge clean room technician Merja Markkanen for her skilful and significant contribution in the fabrication of the devices, which are explored in this Thesis. Also I would like to thank Dr. Jani Kivioja for numerous fruitful and enjoyable discussions on various scientific and non-scientific issues. Ilkka Suni is thanked for support and acknowledged for scientific attitude. Hannu Ronkainen, Dr. Simo Eränen and Prof. Hannu Kattelus are acknowledged for many useful advice regarding device processing. Furthermore, I wish to thank Prof. Jukka Pekola (and his research group at the Low Temperature Laboratory) for lending various articles required in low temperature experiments. I think that I have returned all items, at least the solid ones.

There are also many others who have helped me in various ways during these years, especially, at VTT. I will try my best in listing all of them: Tommi Riekkinen, Antti Tolkki, Tapani Vehmas, James Dekker, Hannu Luoto, Meeri Partanen, Harri Pohjonen, Tommi Suni, Sami Vähänen, Risto Hautakoski, Harri Ilmari, Harri Sillanpää, and Kristiina Rutanen. Probably I forgot many. Don't be offended if your name didn't appear, I'm still grateful!

I would also like to thank all my friends for generating many memorable and fun activities outside the "office". There is nothing more relaxing than to hold a bachelor party to a guy who is *NOT* getting married, at least not in the predictable near future.

Some of us did get married on the way. And finally, and most of all, I wish to express my gratitude to my wife Eeva for her unconditional love and support. Furthermore, I wish to thank our nine-month-old daughter Elsa *a.k.a* Muhku for many cheerful moments and also for (relatively) good behavior.

Espoo, November, 2007

Mika Prunnila

List of publications

This Thesis consists of an overview and following publications:

I M. Prunnila, J. Ahopelto, and F. Gamiz, *Electron mobility in ultrathin silicon-on-insulator layers at 4.2 K*, Applied Physics Letters **84**, 2298–2300 (2004).

II M. Prunnila, J. Ahopelto, K. Henttinen and F. Gamiz, *Gate bias symmetry dependency of electron mobility and prospect of velocity modulation in double-gate silicon-on-insulator transistors*, Applied Physics Letters **85**, 5442–5444 (2004).

III M. Prunnila, J. Ahopelto, and H. Sakaki, *Transport properties of double-gate SiO_2–Si–SiO_2 quantum well*, physica status solidi (a) **202**, 970–976 (2005).

IV M. Prunnila, J. Ahopelto, and F. Gamiz, *Electron mobility and magneto transport study of ultra-thin channel double-gate Si MOSFETs*, Solid-State Electronics **49**, 1516–1521 (2005).

V M. Prunnila and J. Ahopelto, *Two sub-band conductivity of Si quantum well*, Physica E **32**, 281–284 (2006).

VI M. Prunnila, P. Kivinen, A. Savin, P. Törmä, and J. Ahopelto, *Intervalley-scattering-induced electron-phonon energy relaxation in many-valley semiconductors at low temperatures*, Physical Review Letters **95**, 206602 (2005).

VII M. Prunnila, *Electron–acoustic-phonon energy-loss rate in multicomponent electron systems with symmetric and asymmetric coupling constants*, Physical Review B **75**, 165322 (2007).

These appended Papers are referred to by their roman numericals in the overview part.

Author's contribution

All the devices, which are studied in the appended Papers, and their fabrication processes have been designed by the Author. He has actively participated to the device fabrication: most of the device processing has been done in collaboration with clean room technician Merja Markkanen and the Author. The devices have been fabricated in the clean-room of VTT at Micronova. All electrical characterization including the operation of the related low temperature apparatus have been performed by the Author, except the ones reported in Paper VI. The theoretical derivations in Papers VI and VII are done by the Author. He has also written all appended Papers.

Contents

Appendices of this publication are not included in the PDF version. Please order the printed version to get the complete publication (http://www.vtt.fi/publications/index.jsp).

Chapter 1

Introduction

A free electron can be described by its momentum and spin. Conduction electrons in semiconductor devices have one extra degree of freedom, namely conduction band or valley index, which arises from the presence of the atomic lattice of the semiconductor. The atomic lattice also determines the effective mass of the electron. On the other hand, if the effective dimensions of the semiconductor device are tuned by confining electrons by external fields and/or structural manipulation down to the length scale of the de Broglie wave length, then the electronic motion is spatially quantized leading to existence of spatial sub-bands and sub-band index degree of freedom. If such confinement is created in one spatial dimension (and the electrons are allowed to move freely in the remaining two), then the system is referred as two dimensional electron gas (2DEG) and the confining potential as a quantum well. Multiple conduction band valleys and/or 2D sub-bands are present in many basic solid-state electronics devices. One example is the bulk Si metal-oxide-semiconductor-field-effect-transistor (MOSFET), where the transistor channel can be sub-10 nm-thick due to effective confining potential arising from the gate oxide barrier and electrostatic field of the gate electrode. The thin channel and many-valley conduction band of Si leads to coexistence spatial sub-band and valley degrees of freedom.

Due to thermal excitation several spatial sub-bands and all conduction band valleys are occupied in the channel of n-type Si MOSFET at room temperature. Note, however, that the qualitative operation of this device by no means relays on such multi-band effects, but on electrostatics and the energy gap between the valence band and the conduction band. At low temperatures typically only single 2D spatial sub-band in the transistor channel is populated. Furthermore, if the crystal orientation of the Si-gate oxide interface is the standard (001), then only two equivalent conduction band valleys are occupied making the conduction band index degree of freedom irrelevant in most cases. In other words, at low temperatures the electron system in the channel of single-gate (001) Si MOSFET is a relatively ideal 2DEG whose electron density can

be controlled by a gate electrode. These are the reasons why Si MOSFETs have been broadly utilized as a laboratory for 2D physics. [1] Heterostructure FETs based on III-V compound semiconductors provide some benefits in comparison to Si MOSFETs. [2] For example, due lattice-matched interfaces (and modulation doping) the electrons can move several orders of magnitude longer distances without scattering in III-V based FETs in comparison to Si MOSFETs. Furthermore, advanced epitaxial techniques of compound semiconductors have enabled realization of double-gate and/or bi-layer structures where the population of spatial sub-bands can be easily controlled.

The quantum well system of interest in this Thesis is a SiO_2-Si-SiO_2 heterostructure, where single crystalline Si film is sandwiched between amorphous SiO_2 layers. This structure is provided by the silicon-on-insulator (SOI) technology [3, 4]. The SiO_2-Si-SiO_2 quantum well is a unique material system with strong electronic (and optical) confinement, many-valley conduction band and indirect energy gap. However, above all, the SiO_2-Si-SiO_2 structure enables insertion of both a metallic top gate and back gate electrodes. This provides a double-gate SiO_2-Si-SiO_2 FET geometry, where spatial low temperature sub-band population can be adjusted in the spirit of III-V couterparts. Furthermore, the high break-down field of the SiO_2 barriers enable carrier density control in a broad range. Si-based double-gate FETs are also attractive devices from the viewpoint of microelectronics industry. They are regarded as a promising solution to the problems faced when the device length is down-scaled into sub-50 nm regime due to superior electrostatic gate control of the transistor channel charge. [4, 5]

The electronic transport studies of this Thesis are focused on single-gate (Paper I) and double-gate (Papers II–V) SiO_2-Si-SiO_2 FETs. Fabrication of these devices exploit wafer bonding techniques, which enables utilization of thermal SiO_2 layers and results in excellent electronic properties. For example, for a 17 nm-thick double-gate Si quantum well we observe a maximum low temperature mobility above 2 m^2/Vs. This value is comparable to maximum mobilities found in high-mobility bulk Si MOSFETs. When the quantum well thickness is below $\sim$ 20 nm the presence of two Si-SiO_2 interfaces start to degrade the mobility [I]. The double-gate geometry enables control of the population of the spatial sub-bands even at modest electron densities if the Si well thickness is above $\sim$ 10 nm and at the low temperature side the focus is on single and two spatial sub-band effects. The contrast between these two ranges of 2D transport is significant. Population of the second spatial sub-band can be recognized in conductivity/mobility [V], Hall effect [III] and high-field magneto transport [III, IV]. For example, the conductivity/mobility shows a significant drop at the threshold of the second spatial sub-band, which is due to inter-sub-band coupling. At high electron densities with two populated spatial sub-bands and asymmetric effective quantum well potential the Coulomb interaction pushes the electron wave functions related to different sub-bands against different Si-SiO_2 interfaces.

When the effective potential is made symmetric (by adjusting the double-gate bias) the wave functions delocalize across the Si well and we observe a drop in the conductivity [V], which is similar to the resistance resonance effect of bi-layer quantum wells [6–8]. At room temperature several sub-bands are inevitably populated and the most relevant observed effect is a smooth mobility enhancement towards symmetric quantum well potential. [II, IV] This mobility enhancement, sometimes referred as the volume inversion effect, is due to double-gate field adjustment of electron wave functions. It follows mainly from minimization of surface roughness matrix elements and phonon form factors. The mobility enhancement is another benefit, in addition of boosting the gate control, of double-gate FETs in comparison to similar single-gate FETs.

Besides electron transport the band degree of freedom plays a role in electron energy relaxation as well, which is the second subject of this Thesis (Papers VI and VII). Electron gas cools itself by radiating phonons and the more phonon-radiative transitions are allowed the more efficient is the cooling. Therefore, if band index (valley or sub-band index) degree of freedom provides a larger phase space for such transitions one intuitively expects enhancement of phonon cooling when many bands are present in comparison to single-band case. [9] However, this is not of interest in this Thesis. We consider more exotic case where the band index does not directly provide such extra phase space, but still enhancement can occur if the phonons couple differently to different bands and single-band coupling is strongly screened due to electron-electron interaction. Here we develop a theory for this type of electron-phonon (*e-ph*) energy loss rate. [VI, VII] The theory allows elastic inter and intra-band scattering. Our model reproduces the long wavelength single-band *e-ph* energy loss rate results found in the literature. [9–12] In the multi-band regime we find a strong enhancement of the energy loss rate if phonons couple asymmetrically to different bands. A canonical example of such many-band *e-ph* energy loss occurs when conduction band electrons in a many-valley semiconductor radiate long wavelength acoustic phonons. The effect is experimentally explored in heavily doped n-type Si samples at low temperatures. [VI]

This outline is organized as follows: first we introduce the experimental methods in Chapter 2. We briefly outline the device fabrication and characterization procedures used in the appended Papers. Then in Chapter 3 we discuss basic physical properties of many-band systems focusing on many-valley semiconductors and quantum wells. The main results of this Thesis are given in Chapters 4 and 5. The former deals with transport in quantum wells (Papers I–V) and the latter outlines many-band *e-ph* energy relaxation in 2D and 3D systems (Papers VI and VII). As 2D transport in quantum wells and *e-ph* energy relaxation are quite broad subjects of their own these Chapters begin with a brief introduction to the respective topics. Finally, we conclude and summarize the Thesis in Chapter 6.

Chapter 2

Experimental methods

The solid-state device structures that are investigated in this Thesis are SiO_2-Si-SiO_2 quantum wells and heavily doped n-type Si films. The former structures are a single-gate (Paper I) and double-gate (Papers II–V) metal-oxide-semiconductor-field-effect-transistors (MOSFET) where thin ($\sim$ 5–20 nm) single-crystalline Si channel is sandwiched between amorphous SiO_2 layers. The doped films are sub-100 nm-thick metallic Si:P layers, which are utilized in electron-phonon (*e-ph*) energy loss rate studies of Paper VI. All devices are based on the silicon-on-insulator (SOI) structure. [3, 4] They are fabricated on the top Si layer of a SOI wafer by applying the standard procedures of microfabrication. [13, 14] In this part of the Thesis we will first sketch the fabrication processes and describe the physical device structures. Then we introduce the methods that are used in the electrical characterization of the fabricated devices.

2.1 Device fabrication and structures

The starting material for all devices is a commercial 100 mm diameter SOI wafer with (001) Si top layer. The SOI wafers utilized here are fabricated by the so-called smart-cut process [15] by SOITEC company.

2.1.1 SiO_2-Si-SiO_2 quantum wells

The flow of the fabrication process for the quantum well devices is schematically depicted in Fig. 2.1. Details for steps (a)–(i) in the Figure are given below:

(a) Thermal dry oxide (SiO_2) is grown at 1000 °C. The oxide thickness is 84 nm. This layer will serve as the back gate oxide or as a "new" buried oxide (BOX).

(b) The oxidized SOI wafer is bonded to heavily doped n-type Si wafer, which will serve as a "metallic" back gate. The wafer bonding is performed by dropping one wafer

on the other in vacuum. The bonded interface is strengthened by annealing in wet oxidizing ambient at 1100 °C for two hours, which produces a $\sim$ 830 nm oxide around the wafer stack.

(c) The oxide on the back side of the SOI handle wafer is removed by plasma etching (CHF_3/CF_4/He plasma) and the whole handle wafer is stripped in 25% tetramethyl ammonium hydroxide (TMAH) solution at 80 °C. The "old" BOX layer is stripped in a buffered hydrofluoric acid (BHF) and as a result we have a SOI wafer with heavily doped handle.

(d) Thin stack oxide is grown at 1000 °C and nitride (SiN) layer is deposited by low pressure chemical vapor deposition (LPCVD). The nitride is patterned utilizing UV-lithography[1] and SF_6/O_2 plasma etching. Local oxidation of Si (LOCOS) is performed: the SOI layer is fully oxidized in the regions which are not covered by the nitride. This step defines the active areas of the devices, which are bounded by the field oxide regions.

(e) The nitride layer and the stack oxide are stripped by plasma etching and BHF, respectively. Another LOCOS step is perform in order to make the areas where the actual quantum well channels reside thinner than the contact regions.

(f) Gate oxide is grown by thermal dry oxidation at 1000 °C resulting in 45 nm oxide. Next poly silicon top gate electrode is deposited by LPCVD. The gate layer is ion implanted by high dose of As in order to provide metallic conduction. The gate is patterned with UV-lithography and Cl_2/He plasma etching.

(g) The contact regions are implanted with high dose of As while the gate electrode masks the quantum well channel.

(h) A 500 nm-thick oxide is deposited by CVD. The implanted doses are activated and diffused by annealing at 950 °C for 30 min in nitrogen ambient.

(i) Contact windows are opened and Al is deposited by sputtering. The Al metallization is then patterned and the device is annealed in N_2/H_2 ambient at 425 °C for 30 min.

This Thesis involves three batches of quantum well devices: two double-gate batches (B and F) and one single-gate batch. The above description fits to the double-gate devices of batch F. Devices of batch B differ very little from F. The major difference between these batches is the definition of the active areas [Fig. 2.1(d)]. For batch B the active area definition is performed by mesa etching instead of LOCOS. The double-gate devices of batch B and F are explored in Papers II–V. Prior to batches B and F a batch of single-gate FETs was fabricated. The fabrication process of these devices follows steps (d)–(i) (with mesa etching). Properties of the single-gate devices are reported in Paper I.

Figure 2.2(a–b) shows cross-sectional transmission electron microscopy (TEM) images of a fabricated device (batch B). The recessed channel structure resulting from the second

[1] All lateral patterning is performed with UV-lithography.

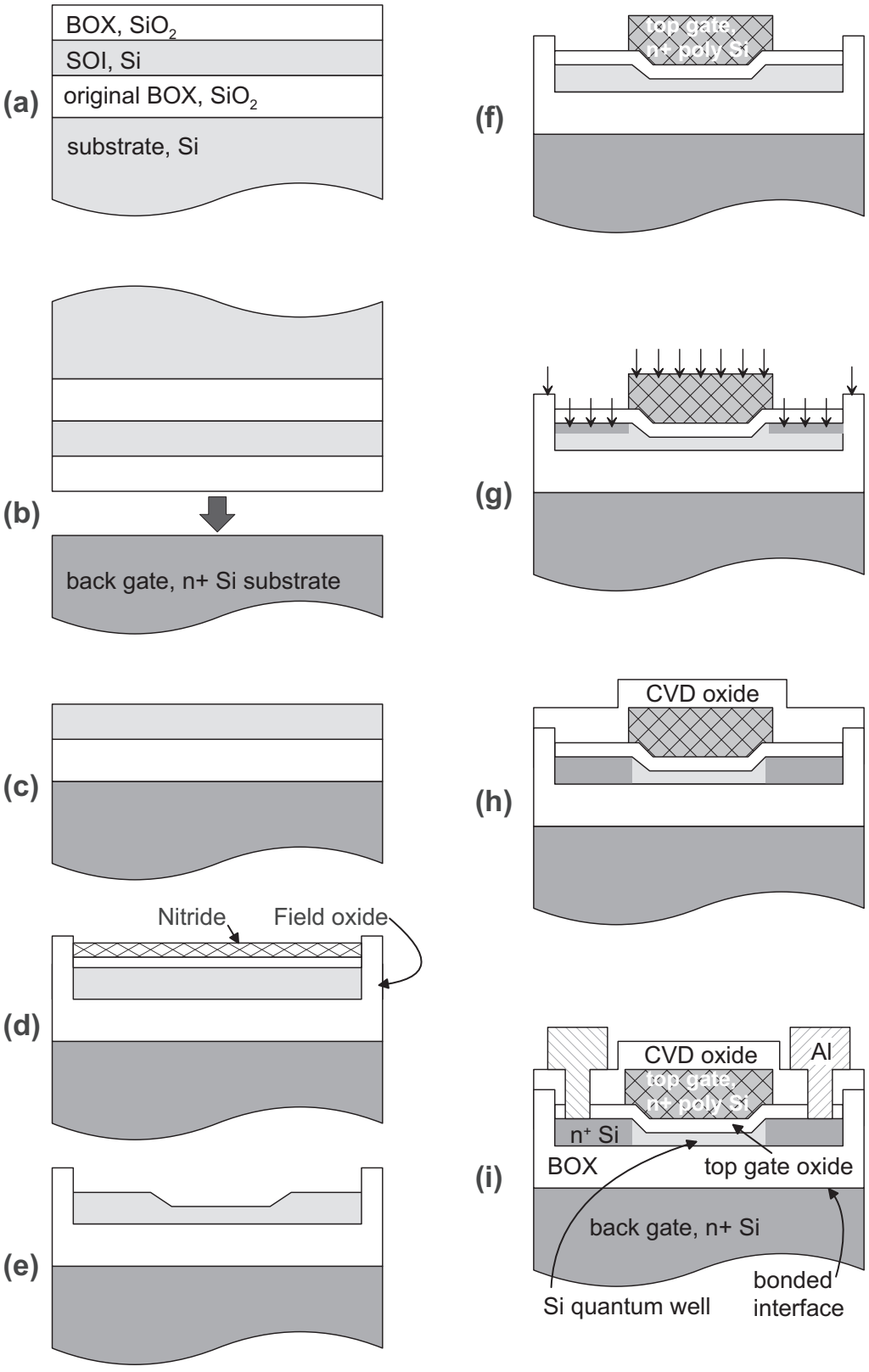

Figure 2.1: *Schematic illustration of the fabrication of the double-gate Si quantum well FET samples. See Sec. 2.1.1 for details.*

LOCOS performed in step (e) and the poly-crystalline structure of the top gate electrode is evident from Fig. 2.2(a). This type structure is favorable in order to have small source/drain series resistance arising from the n^+ contacts. The high resolution image [Fig. 2.2(b)] reveals the crystalline structure of the Si quantum well and amorphous gate oxides. All experimental results given in this Thesis are measured from large lateral size Hall-bar devices depicted in Fig. 2.2(c).

The SOI wafer fabrication process of SOITEC company generates some long length scale variation to the SOI film thickness.(see Paper I) This variation is ~ 10 nm, which is of the same magnitude as the targeted Si well thickness $t_w = 5$–20 nm. Therefore, the SOI thickness was always mapped with scanning photo reflectance prior to gate oxide growth as described in Paper I. If the Si well thickness $t_{W,0}$ is known before oxidation and the thickness of the oxide t_{OX} is measured then the final t_W can be unambiguously determined by noting that stoichiometric SiO_2 has 46% of Si (in volume), i.e., $t_W \simeq t_{W,0} - 0.46 \times t_{OX}$. [13] However, the cleaning step performed before gate oxide process etches a thin layer of silicon. The thickness of this layer is ~ 2 nm, but it may slightly vary from batch to batch leading to some uncertainty in t_W. The t_W obtained from TEM analysis was utilized to circumvent this problem.

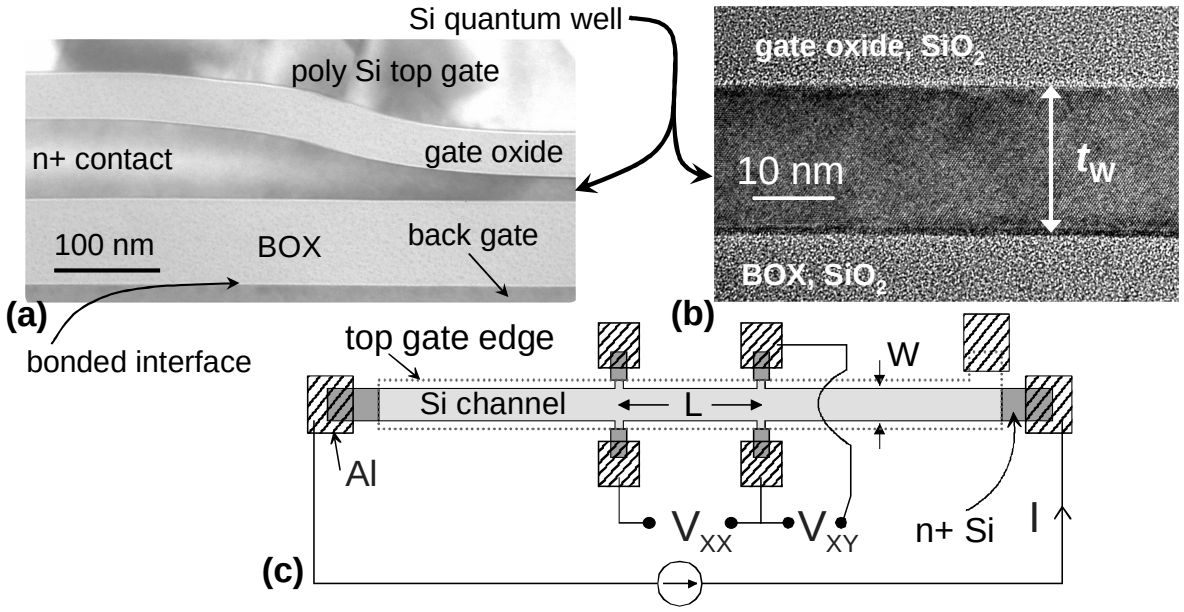

Figure 2.2: *(a) TEM image of a double-gate Si quantum well FET illustrating the recessed channel structure (batch B device). (b) High-resolution TEM image of the Si well. Well thickness $t_W \approx 18$ nm. (c) Schematic illustration of the lateral device geometry ($L/W = 4$, $W = 100$ μm) used in the measurements including the external circuitry.*

2.1.2 n^+ Si films

The cross-section of the n^+ silicon samples of the electron-phonon coupling measurements of Paper VI is identical to the n^+ source/drain contact regions of the double-gate transistors (see Figs. 2.1 and 2.2). The fabrication utilizes mesa etching to define the lateral geometry of the films and steps (g) and (i) (see above). The Si films are implanted with different doses of P in order to vary the concentration of charge carriers. The selected doses and subsequent high temperature annealing produce active doping (electron) concentrations in the range $3.5 - 16 \times 10^{25}$ m^{-3}, which is enough to make Si a metallic conductor (see Sec. 3.1.1).

Lateral sample geometry together with biasing circuits in the experiments is depicted in Fig. 2.3. The Figure contains also a Table of sample parameters. The mean free path is determined from $l_e = v_F\tau$, where the relaxation time τ is calculated from 4.2 (while the electron density n_e and resistivity $\rho_e = 1/\sigma$ are determined experimentally). Small n^+ Si–Al contacts are used in electron temperature determination as will be described below.

2.2 Device characterization

2.2.1 Electrical measurements

The electronic properties of the fabricated devices are measured using DC and lock-in techniques. The diagonal, $\rho_{xx} = (L/W)\,V_{xx}/I$, and non-diagonal/Hall, $\rho_{xy} = V_{xy}/I$, components of sheet resistance were obtained by adopting standard four-point measure-

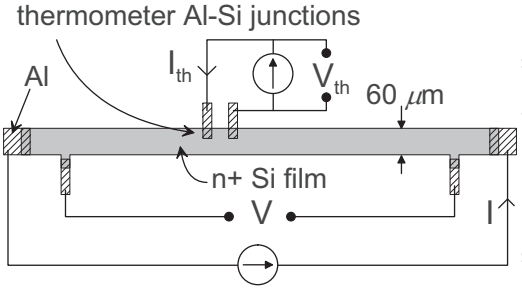

Sample	n_e (10^{25} m^{-3})	ρ_e (10^{-5} Ωm)	l_e (nm)	d (nm)
A	3.5	1.04	5.06	70
F	6.7	0.63	5.42	58
G	12.0	0.51	4.54	58
H	16.0	0.44	4.34	58

Figure 2.3: *(left panel) Schematic illustration of the n^+ Si sample geometry and the measurement circuitry. In the experiments the ∼9500 μm long n^+ Si film is heated with a DC current I while the electron temperature is determined using current biased Al-n^+ Si-Al contacts. (right panel) The characteristics of the films: n_e - carrier concentration, $\rho_e = 1/\sigma$ - 1.5 K resistivity, l_e - electron mean free path, d - n^+ Si film thickness. All samples have 400 nm thick buried oxide layer. After Paper VI.*

ments. Voltage V_{xy} results from perpendicular magnetic field, which is produced with NbTi superconducting solenoid. In the case of the Si quantum wells the resistivity measurements [see Fig. 2.2(c)] were performed with DC techniques at 4.2 K and at 300 K. In detail, the linear transport coefficients $\rho_{xx,xy}$ were obtained by applying few current[2] values and then performing linear fitting to $V_{xx,xy} = \rho_{xx,xy}I + O$ to remove possible offset O resulting from, e.g., buffer amplifiers. In the sub-4.2 K case lock-in techniques were adopted to obtain $\rho_{xx,xy}$. In these measurements the DC excitations and resulting responses are replaced by small amplitude AC signals. The lock-in scheme enables utilization of low signal levels even in the presence of noise. The lock-in amplifiers that are used in detecting the system response are phase locked to reference signal, which also provides the excitation (here basically the current).Frequency of the reference signal was set below 20 Hz in order to minimize the effects arising from stray capacitances.

The characterization of the Si wells involves also (differential) gate-to-channel capacitance measurements. Capacitance can be conveniently measured with lock-in technique by applying an AC voltage and detecting the current component that is in 90 degrees phase shift with respect to the voltage. Gate capacitance is measured as a function of a gate voltage, which requires relatively high DC gate bias under the small AC excitation. Therefore, the gate capacitance measurements were performed with Agilent 4294A precision impedance analyzer. The gate-to-channel capacitance is utilized in determining the total carrier density n_e at $T = 300$ K by numerical integration. In order to connect the measured capacitance to physical carrier density in the Si channel the capacitance must be free from components arising from substrate (or second gate in double-gate structures). This is why it is precisely the gate-to-channel capacitance that is measured and not, e.g., the total gate capacitance or gate-to-ground capacitance. This type of technique is sometimes referred as split-capacitance voltage measurement. [16]

The measurements of the n^+ Si films aim to determination of thermal electron-phonon response, i.e., the rise of the electron temperature T_e in the Si film vs. uniform input DC power density $P = VI/Volume = \rho_e J^2$ (J being the current density). The input power is determined again by four point measurement as depicted in Fig. 2.3. The local electron temperature is measured by the tunnel junction method described below.

2.2.2 Sample cooling and temperature

The devices are characterized at room temperature ($T = 300$ K) and at low temperatures. Low temperature measurements utilize various refrigeration techniques, such as,

[2]Even though we declare here that current is applied quantity we always also measure the current when determining $\rho_{xx,xy}$, i.e., the value of the current is not based on a known bias resistor and applied voltage.

immersion to liquid helium, ^{3}He sorption cryostats and dilution refrigerator based on ^{3}He/^{4}He mixture. The immersion produces substrate temperature of $T = 4.2$ K. ^{3}He sorption cryostats enable base temperatures down to ~ 250 mK and ^{3}He/^{4}He dilution refrigerators can provide temperatures as low as few tens of mK. A detailed description of these standard refrigeration techniques can be found, e.g., in the text book of F. Pobell [17].

In the sub-4.2 K measurements the substrates of the devices are mounted to the metallic sample holder of the cryostat. The substrate temperature in these experiments is determined by calibrated RuO_2 thermometers of the sample holder. In the *e-ph* thermal coupling experiments reported in Paper VI (see also Sections 5.1 and 5.3) the electrons are heated above the substrate temperature by electric current I as depicted in Fig. 2.3. The increase in the electron temperature due to this heating is measured by n^+ Si-superconducting Al contacts. Due to the Schottky barrier (and possible native oxide residuals) the behavior of these contacts resemble those of normal metal-insulator-superconductor (NIS) junctions. Thanks to the superconducting gap the current voltage characteristics of the NIS junctions provide good sensitivity to the electron temperature of the normal electrode and, at the same time, thermal isolation. These properties make NIS junctions attractive electron thermometers and they have been broadly used in various experiments. [18] The electron thermometers are calibrated against the sample holder thermometer by slowly adjusting the cryostat temperature. An example of such calibration curve is shown in Fig. 2.4. Similar, electrically isolated, tunnel junction thermometers were also utilized to monitor the substrate over-heating on the top of the chip in the *e-ph* coupling measurements (they are omitted from Fig. 2.3 for the sake of clarity).

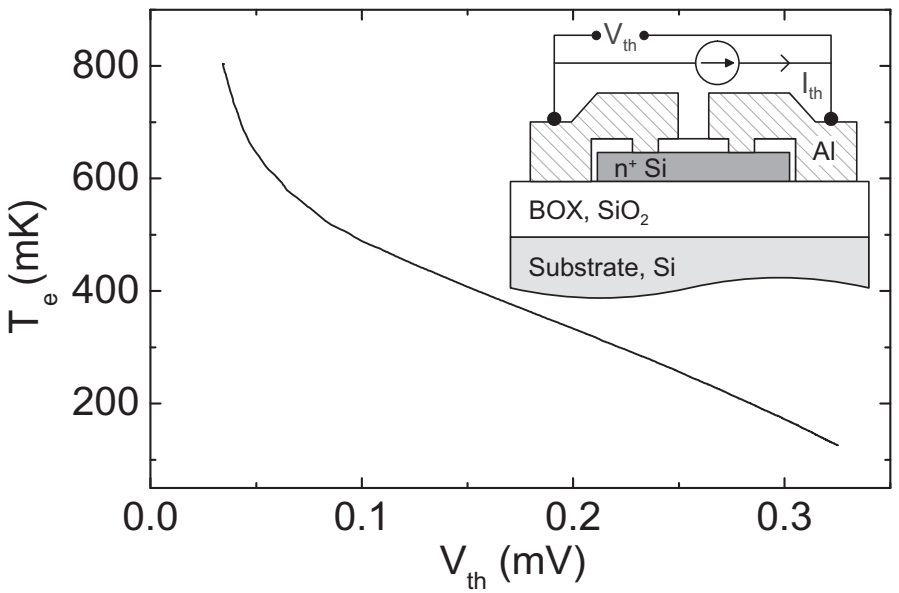

Figure 2.4: *Calibration curve of the n^+ Si - Al double junction thermometer depicted in the inset. The junction area is $6 \times 6\ \mu m^2$ and the current bias $I_{th} = 1\ nA$.*

Chapter 3

Basics of single and many-band systems

In this part of the Thesis we review some basic properties of single and many-band electron systems formed in the conduction band of semiconductors. First we introduce the electron systems that are relevant to this work, namely, many-valley semiconductors and 2D sub-bands in quantum wells. Then we discuss about elastic scattering mechanisms and phonon scattering in the framework of golden rule formula and, finally, discuss screening.

3.1 Bulk semiconductors and quantum wells

3.1.1 Preliminary concepts

Periodic crystal gives rise to energy bands, i.e., allowed energy $\mathcal{E}$ versus wave vector $\boldsymbol{k}$ relationships $\mathcal{E} = \mathcal{E}_{l\boldsymbol{k}}$, where l is the band or (valley) index.[1] Close to the conduction band edge (low energies) the electron dynamics can be typically approximated using the effective mass model [19]

$$\mathcal{E}_{l\boldsymbol{k}} = \hbar\boldsymbol{k}\frac{1}{2m}\hbar\boldsymbol{k} + E_l, \tag{3.1}$$

where m is the effective mass tensor (the free electron mass is denoted by m_e), which in general depends on the band index. The energy E_l is the conduction band edge energy. It is customary to measure the energy from the respective band edge. This is achieved by substitution $\mathcal{E}_{l\boldsymbol{k}} \longrightarrow \mathcal{E}_{l\boldsymbol{k}} - E_l$. For isotropic s-symmetric band the energy vs. wave vector relationship can be approximated by scalar effective mass m, whence $\mathcal{E}_{\boldsymbol{k}} = \hbar^2\boldsymbol{k}^2/2m$, which differs from classical kinetic energy of a free electron only by the appearance of the effective mass instead of m_e. The isotropic description works, for example, for

[1] As momentum is defined by $\boldsymbol{p} = \hbar\boldsymbol{k}$ typically $\boldsymbol{k}$ is also loosely referred as momentum.

GaAs ($m \approx 0.067m_e$), which has single conduction band minimum at Γ point in the first Brillouin zone of reciprocal space ($\boldsymbol{k}$-space origin). This makes GaAs a single-valley (or single-band) semiconductor. In many-valley semiconductors, such as Si, Ge or AlAs, the conduction band edge consists of several equivalent minima. In Si the bottom of the conduction band is close to the X-point and it has six-fold degeneracy. This degeneracy is visualized in Fig. 3.1, where the constant energy ellipsoids in the vicinity of the Si conduction band edge are shown in $\boldsymbol{k}$-space (reciprocal space). The shift of the minima from the Γ point along the [100] axes is approximately $k_0 = 0.85(2\pi/a)$ ($a = 0.5431$ nm is the lattice constant). [21] All the Si valleys have similar dispersion relations. For example, the dispersion relation for the [001] valleys is

$$\mathcal{E}_{\boldsymbol{k}} = \frac{\hbar^2 k_z^2}{2m_l} + \frac{\hbar^2(k_x^2 + k_y^2)}{2m_t}, \tag{3.2}$$

where the transverse mass $m_t = 0.191m_e$ and the longitudinal mass $m_l = 0.916m_e$.

Momentum $\boldsymbol{k}$ and band index l are quantum numbers, which describe the state of electron. The actual quantum mechanical wave function can be considered as a product of a so-called Bloch part, which has periodicity of the crystal lattice, and long wave length envelope wave function, which in 3D systems is a "free electron" plane wave $\exp(i\boldsymbol{k} \cdot \boldsymbol{r})$. Often the knowledge of the envelope wave function is enough to understand the properties of the system. If the electrons are confined in a narrow potential well then the electron motion is quantized in the dimension perpendicular to the well layer (z-direction). Now the envelope wave function differs from simple plane wave along z-coordinate, momentum k_z is now longer a good quantum number and discrete 2D sub-band energies E_n appear. This kind of system is referred as two-dimensional electron

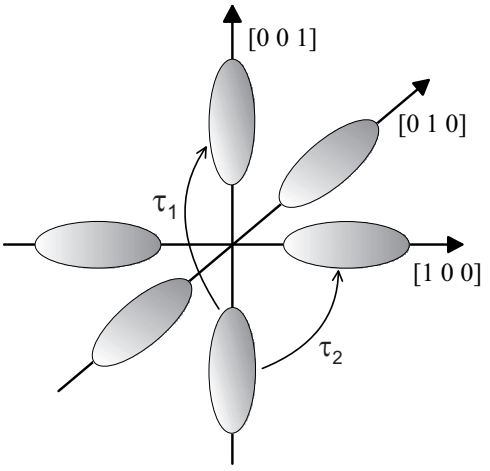

Figure 3.1: *Schematic illustration of the constant energy ellipsoids of Si conduction band valleys. For a detailed band structure see, e.g., Ref. [20]. We have also included (for future purposes) scattering rates $1/\tau_1$ and $1/\tau_2$ that couple the different classes of the valleys.*

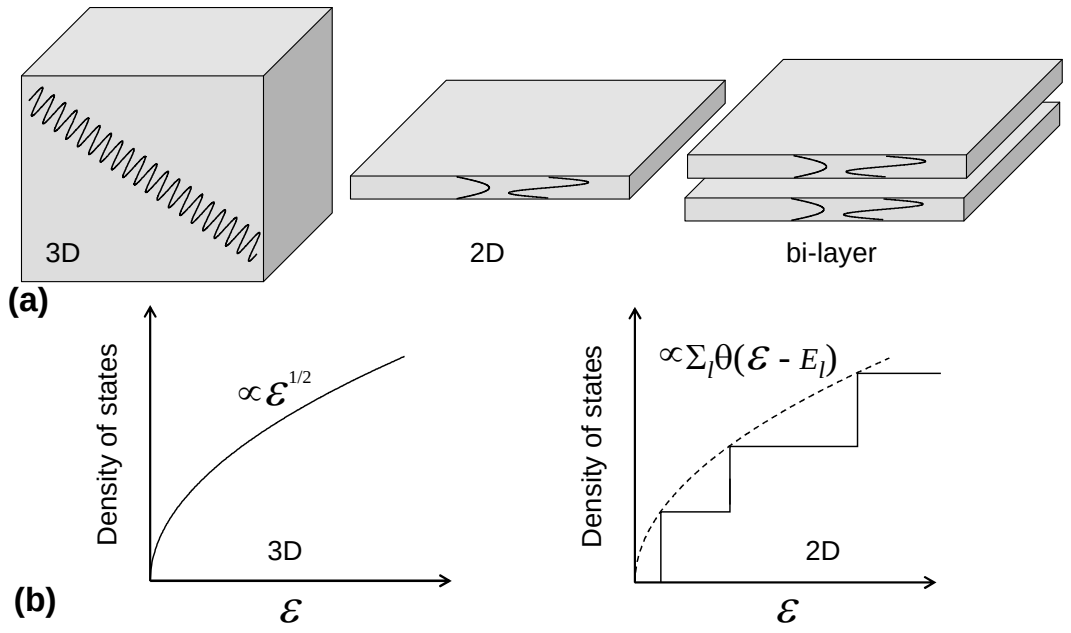

Figure 3.2: *(a) Illustration of 3D, 2D and bi-layer electron systems and envelope wave functions. (b) Single-band and multi-sub-band density of states in 3D and 2D, respectively [see Eq. (3.4)].*

gas (2DEG) and the potential well is referred as a quantum well. [1] The envelope wave functions and related energies E_n can be determined from Schrödinger-like equation (see next Sub-section). The dispersion relations in 2DEG are given by $\mathcal{E}_{n\boldsymbol{k}_\parallel} = E_n + \hbar\boldsymbol{k}_\parallel \frac{1}{2} m_\parallel^{-1} \hbar\boldsymbol{k}_\parallel$, where $m_\parallel$ ($\boldsymbol{k}_\parallel$) is the effective mass (wave vector) in the plane of 2DEG. As in 3D, the dispersion relations are often referred to the threshold E_n by substitution $\mathcal{E}_{n\boldsymbol{k}_\parallel} \longrightarrow \mathcal{E}_{n\boldsymbol{k}_\parallel} - E_n$. Note that the properties of the 2DEG and, therefore, also $\mathcal{E}_{n\boldsymbol{k}_\parallel}$ should obviously depend also on the band index if the 2DEG is formed in a many-valley semiconductor.[2] The notations are simplified if we define a general band index $l = (b, n)$, where b refers to the $\boldsymbol{k}$-space band index and n to spatial sub-band, and permit that in Eq. (3.1) $\boldsymbol{k}$ is either the 3D momentum or 2D momentum $\boldsymbol{k}_\parallel$. Now the dimensionality $d = 2, 3$ of the electron system is revealed by the context or some parameter which depends on d. Many-valley based 2DEGs with single spatial sub-band can be considered as 2D multi-layer layer systems with full spatial overlap. On the other hand, if two 2DEGs are brought in close proximity we have a similar situation, but now the bands are separated spatially. In the case of two layers these kind of systems are referred as bi-layers. 3D, 2D and bi-layer electron systems are illustrated in Fig. 3.2(a).

In electronic devices and systems we are eventually interested in measurable proper-

[2] Confinement can also create coupling between the bands. Discussion of such effects in the case of Si MOSFETs can be found, e.g., from Ref. [22]. We will come back to this so called valley-splitting effect in Sec. 4.2.3.

ties such as electron density, current, or heat flux. These quantities are obtained from microscopic variables taking into account all occupied electron states, which is done by summing over such states. The summation is changed into integral over quasi continuos part of $\boldsymbol{k}$ or related energy according to [2, 19]

$$\frac{1}{V_e}\sum_{states} = \frac{1}{V_e}\sum_l \sum_{\boldsymbol{k}} \longrightarrow \sum_l \int \frac{d^d k_l}{(2\pi)^d} = \sum_l \int d\mathcal{E}_{l\boldsymbol{k}} \nu_l(\mathcal{E}_{l\boldsymbol{k}}) = \int d\mathcal{E}\nu(\mathcal{E}). \tag{3.3}$$

Here V_e is the d-dimensional volume of the electron system. The two latter equalities introduce the important density of states functions $\nu_l(\mathcal{E})$ and $\nu(\mathcal{E}) = \sum_l \nu_l(\mathcal{E})$. These are the density of states per band and the total density of states, respectively. The density of states describes the number of states per unit energy per unit volume around energy $\mathcal{E}$. For an ideal parabolic systems $\nu_l(\mathcal{E})$ is given by [2]

$$\nu_l(\mathcal{E}) = 2 \times \frac{m_{de}}{2\pi\hbar^2}\left(\frac{2m_{de}\left(\mathcal{E}-E_l\right)}{\pi^2\hbar^2}\right)^{\frac{d-2}{2}} \theta\left(\mathcal{E}-E_l\right), \tag{3.4}$$

where $\theta(x)$ is the step function, the factor 2 arises from spin degeneracy and m_{de} is the density of states mass. In isotropic systems $m_{de} = m$, whereas, for example, in bulk Si $m_{de} = \left(m_l m_t^2\right)^{1/3} \approx 0.32 m_e$ [l refers to longitudinal as in Eq. (3.2)]. [23] Energy dependency of the density of states is illustrated in Fig. 3.2(b).

One important quantity of interest is the total electron density n_e. At thermal equilibrium the average occupation of an electron state is given by the Fermi-Dirac distribution function $f^0(\mathcal{E}) = 1/\left[1 + e^{(\mathcal{E}-\mathcal{E}_F)/k_B T}\right]$, where $\mathcal{E}_F$ is the Fermi energy[3] and T is the temperature of the electron system. [24] The electron density is now obtained by operating the integral of Eq. (3.3) to $f^0(\mathcal{E})$ giving

$$n_e = 2 \times \sum_l \frac{m_{de} k_B T}{2\pi\hbar^2}\left(\frac{2m_{de}k_B T}{\pi^2\hbar^2}\right)^{\frac{d-2}{2}} \Gamma(d/2) I^F_{\frac{d-2}{2}}\left(\frac{\mathcal{E}_F - E_l}{k_B T}\right), \tag{3.5a}$$

$$I^F_j(x) = \frac{1}{\Gamma(j+1)}\int_0^\infty dt \frac{t^j}{1+e^{t-x}}, \tag{3.5b}$$

where $\Gamma(x)$ is the Gamma function [25]. Note that in 2D n_e has a closed form expression because the Fermi integral $I^F_0(x) = \ln\left(1+e^x\right)$. Closed form expressions for n_e exist also for $d = 2, 3$ in two important special cases: at the limit of Fermi statistics (low temperatures, $\frac{\mathcal{E}_F - E_l}{k_B T} \gg 1$) and Boltzmann statistics (high temperatures, $\frac{\mathcal{E}_F - E_l}{k_B T} \ll -1$). At these limits $f^0(\mathcal{E}+E_l)$ tend to a step function $\theta\left(\mathcal{E} - (\mathcal{E}_F - E_l)\right)$ and to an exponential function $\exp(\frac{\mathcal{E}_F - E_l}{k_B T})$, respectively, whence the electron density is given by

$$n_e = \begin{cases} 2\times \sum_l \frac{m_{de}}{2\pi\hbar^2}\left(\frac{2m_{de}}{\pi^2\hbar^2}\right)^{\frac{d-2}{2}} \frac{d}{2}\left(\mathcal{E}_F - E_l\right)^{d/2}, & \frac{\mathcal{E}_F - E_l}{k_B T} \gg 1 \\ 2\times \sum_l \frac{m_{de}k_B T}{2\pi\hbar^2}\left(\frac{2m_{de}k_B T}{\pi^2\hbar^2}\right)^{\frac{d-2}{2}} \Gamma(d/2)\exp\left(\frac{\mathcal{E}_F - E_l}{k_B T}\right), & \frac{\mathcal{E}_F - E_l}{k_B T} \ll -1 \end{cases} \tag{3.6}$$

[3] We follow the widespread practice of semiconductor literature where the Fermi energy is equivalent to the chemical potential at all temperatures.

At the low temperature limit the density can be written as $n_e = 2 \times \eta_l (2/3\pi^2)^{d-2} k_F^d / 4\pi$ (η_l is the number of equivalent bands), where the Fermi wave vector $k_F = \sqrt{2 m_{de} \frac{\mathcal{E}_F - E_l}{\hbar^2}}$. Fermi velocity $v_F = \hbar k_F / 2 m_{de}$ gives the speed of the electrons at Fermi surface (or average speed if $m_{de} \neq m$). This is a useful quantity as it, e.g., links the mean distance between collisions (mean free path) l_e to the scattering rate τ^{-1}according to $l_e = v_F \tau$.

The expressions for n_e have an "unknown parameter" $\mathcal{E}_F$. In intrinsic (un-doped) systems the value of $\mathcal{E}_F(T)$ is basically determined by the existence of the valence band, which resides the gap energy E_g (1.1 eV for Si) below the conduction band edge. In other words, electrons are thermally excited from the valence band to the conduction band. This leaves empty electron states in the valence band, which are referred as holes. Holes behave as if they were positively charged electrons and their contribution to all processes must be taken into account if their density n_h is sufficiently large. In intrinsic system $\mathcal{E}_F$ is in the middle of the energy gap at low T resulting in exponentially small $n_{e,h}$ [26] and, therefore, insulating behavior as $T \to 0$. Additional electrons/holes can be introduced to the conduction/valence band by impurity doping. A single donor atom has, e.g., one extra electron which is not contributing to the crystal bonds of the host lattice. Similarly acceptor atom requires one extra electron for crystal bonds creating a hole. Good dopants are such that the energy level of the additional carrier is close to the respective band edge (few meV – few tens of meV). Thus, the carrier is relatively weakly bound to the impurity atom and introduction of large quantities of such impurities adjusts $\mathcal{E}_F$, n_e and n_h. If the donor consentration N_D is very high and acceptor concentration $N_A \sim 0$, then the low temperature Fermi level is above the conduction band edge resulting $N_D \sim n_e$ and $n_h = 0$. [27] The opposite case is realized with high N_A, whence $N_A \sim n_h$ and $n_e = 0$. If the Fermi level is above (below) the conduction (valence) band edge the semiconductor behaves like a metallic conductor, which is the case for the highly doped n-type samples in Paper VI. In 2DEGs (Papers I–V) the carrier density is controlled by external gate electrodes as will be discussed below. Note that in this Thesis we study systems where the acceptor consentration N_A and/or n_h is negligible and, therefore, holes are be excluded from all considerations.

3.1.2 2D sub-bands and charge control in quantum wells

Canonical example of 2D electron system is the one in bulk MOSFET channel where the quantum well is formed due to external gate potential and the potential barrier at the Si-SiO_2 interface. [1, 28] Another type of quantum wells are compound semiconductor heterostructure quantum wells. [2] In this work the quantum well is a Si layer, which is sandwiched in SiO_2 (see Fig. 2.2). This type of system resembles both bulk MOSFET and heterostructure system. The eigen energies E_n of the discrete spectrum and envelope

wave functions are solved from the effective mass Schrödinger equation [29, 30]

$$\left(-\frac{\hbar^2}{2}\frac{\partial}{\partial z}\frac{1}{m_z}\frac{\partial}{\partial z}+V_{eff}(z)\right)\psi_n(z)=E_n\psi_n(z), \tag{3.7}$$

where $V_{eff}(z)$ is the effective potential felt by the electron gas. This form of the effective mass Schrödinger equation requires that the effective mass is isotropic in the plane of the 2DEG. More general form can be found from Refs. [28, 31]. The isotropy condition is fulfilled in the case of the [001] valleys (see Fig. 3.1). Their eigen energies (E_n) are also lower than those of the other valleys (E_n') due to heavier perpendicular mass $m_z = m_l$ and, therefore, at low temperatures typically only the [001] valleys are occupied. The total electron wave functions normalized to area A are now $\left|n\boldsymbol{k}_\parallel\right\rangle = \Psi_n(z,\boldsymbol{r}_\parallel) = \psi_n(z)A^{-1/2}\exp(i\boldsymbol{k}_\parallel\cdot\boldsymbol{r}_\parallel)$.

The effective potential $V_{eff}(z)$ in Eq. (3.7) consist of a potential due to the band edge $V_b(z)$, external gates $V_{ext}(z)$ and electron-electron interactions $V_{ee}(z)$. Here we take into account only direct Coulomb interactions (Hartree approximation) whence $V_{ee}(z)$ is given by the Poisson equation and

$$V_{eff}(z) = V_b(z)+V_{ext}(z)+V_{ee}(z) \tag{3.8a}$$

$$\frac{\partial}{\partial z}\varepsilon_b\frac{\partial}{\partial z}V_{ee}(z) = -e^2n(z). \tag{3.8b}$$

Here ε_b is the background dielectric constant and $n(z)=\sum_l N_l\left|\psi_n(z)\right|^2$ is the electron distribution. The factors N_l are the sub-band densities per unit area given by the elements of the sum in Eq. (3.5a). Device cross section, $V_{eff}(z)$ and $n(z)$ are schematically illustrated in Fig. 3.3. The conduction band offset between Si and SiO_2 is several eV and, therefore, the electron wave functions have very small (negligible) penetration into SiO_2.

Equations (3.7) and (3.8) can be solved numerically (self-consistently) in order to find the electron wave functions and the sub-band structure. Figure 3.4 shows results of such calculations for a symmetric effective well potential defined by gate bias $V_{\mathrm{BG}} = V_{\mathrm{TG}}t_{\mathrm{BOX}}/t_{\mathrm{OX}}$. Figures 3.4(a) and (b) show the electron wave functions and $V_{eff}(z)$ in a SiO_2-Si-SiO_2 quantum well with $t_W = 14$ nm at $T = 1$ K. Only two spatial sub-bands are populated and they originate from the Si valleys who reside along [001] direction, i.e., $m_z = m_l$ and $m_{||} = m_t$. The shape of $V_{eff}(z)$ inside the Si well is due to Coulomb interaction [$V_{ee}(z)$]. Note that the barrier increases in the middle of the well as a function of the carrier density and well width. Therefore, at high n_e and/or sufficiently large t_W the system is driven towards spatially separated bi-layer. We have followed the convention where the lowest symmetric sub-band is referred as bonding sub-band (ψ_{B}) and the second sub-band the anti-bonding sub-band (ψ_{AB}). These wave functions are related to sub-band densities n_{B} and n_{AB}, respectively. Left vertical axis of Fig. 3.5 shows experimental densities n_{B}, n_{AB} and $n_e = n_{\mathrm{B}} + n_{\mathrm{AB}}$ as a function of the top gate

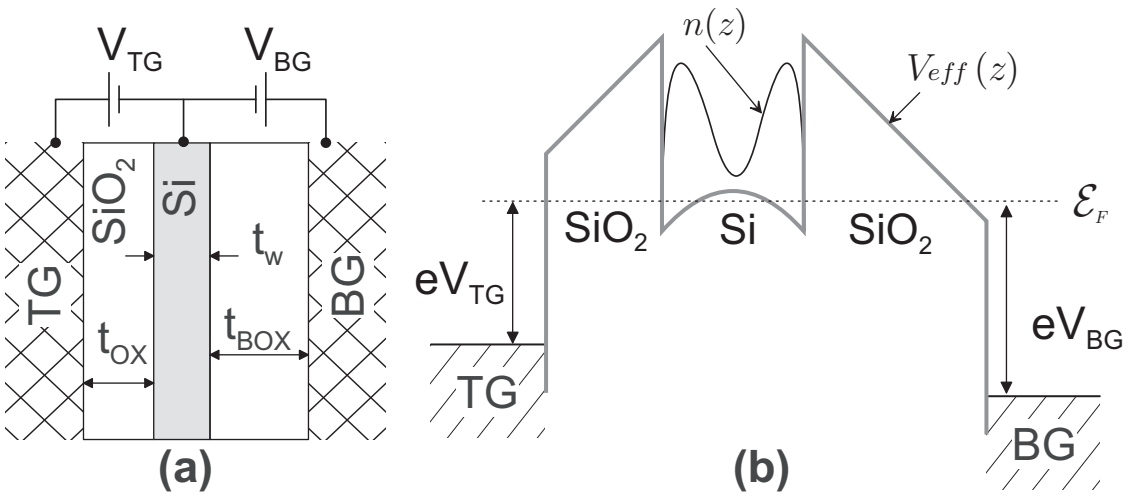

Figure 3.3: *(a) Schematic cross-section of a double-gate Si quantum well and gate biasing. (b) Illustration of the energy band diagram of the device together with the electron distribution $n(z)$. See also Figs. 2.2 and 2.1.*

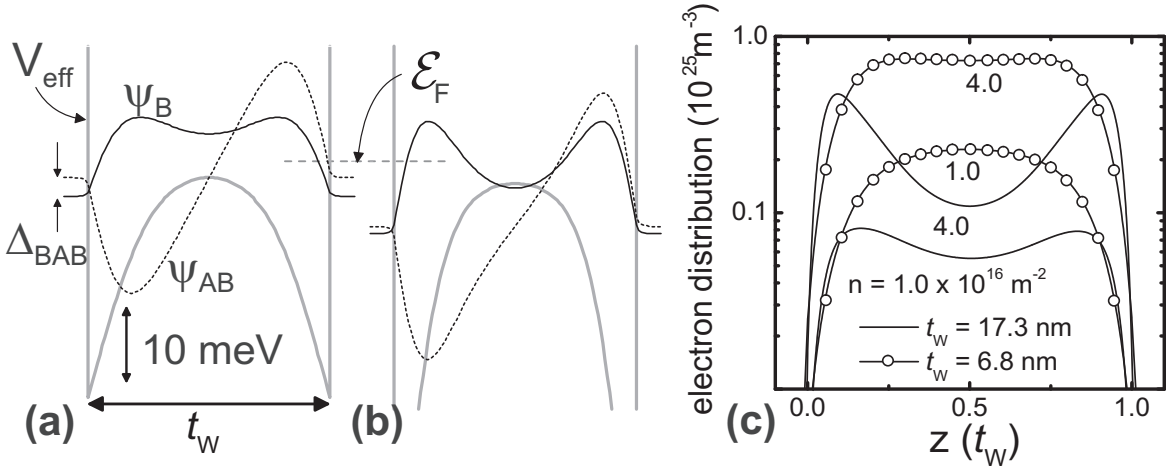

Figure 3.4: *(a),(b) Self-consistent bonding Ψ_B and anti-bonding Ψ_{AB} electron wave functions together with the effective potential V_{eff} in the 14 nm thick Si well at balanced gate bias within the Hartree approximation at 1 K. The wave functions are offset so that $\Psi_{B,AB} = 0$ is equal to the corresponding eigen energy $E_{B,AB}$. The total electron density is (a) $n_e = 1.0 \times 10^{16}$ m^{-2} and (b) $n_e = 2.8 \times 10^{16}$ m^{-2}. (c) Self-consistently calculated multi-sub-band electron distributions $n(z)$ in the Si well at different electron density values at symmetric gate bias at 300 K. After Papers IV and V.*

voltage $V_{\rm TG}$ along the balanced gate bias line. The right vertical axis shows the bonding anti-bonding energy gap $\Delta_{\rm BAB} = \mathcal{E}_{AB} - \mathcal{E}_B$, which is obtained by substituting $n_{\rm B}$ and $n_{\rm AB}$ to Eq. (3.6) with mass $m_{de} = m_{\rm t}$ and valley degeneracy of two. The slope $V_{\rm TG}$ vs. $n_e = n_{\rm B} + n_{\rm AB}$ in Fig. 3.5 corresponds accurately to the total gate capacitance, i.e., $n_e/e = C_{\rm TG}V_{\rm TG} + C_{\rm BG}V_{\rm BG}$, where $C_{TG} = \frac{\varepsilon_0\varepsilon_{ox}}{t_{OX}}$ and $C_{BG} = \frac{\varepsilon_0\varepsilon_{ox}}{t_{BOX}}$ are the geometrical capacitances of the top gate and back gate oxides (per unit area), respectively. This type of linear relationship requires a relatively high positive bias at both gate electrodes as is experimentally demonstrated in Fig. 3.6, which shows normalized room temperature $C_{\rm TG}(V_{\rm TG}, V_{\rm BG}) = e\partial n_e(V_{\rm TG}, V_{\rm BG})/\partial V_{TG}$. When V_{TG} is below zero and V_{BG} is sufficiently high C_{TG} is below unity (but finite) because the electron gas is pushed against the Si-BOX interface while the Si-OX interface is depleted.

3.2 Scattering mechanisms and screening

In this Thesis we deal with phenomena that require knowledge of transition rates between different states of the electron system (or coupled electron-phonon system). The microscopic transition probability per unit time or the scattering rate can be calculated from the golden rule formula [32]

$$W_{f,i} = W_{i\to f} = \frac{2\pi}{\hbar} \left|\langle f| H |i\rangle\right|^2 \delta(\mathcal{E}_i - \mathcal{E}_f), \tag{3.9}$$

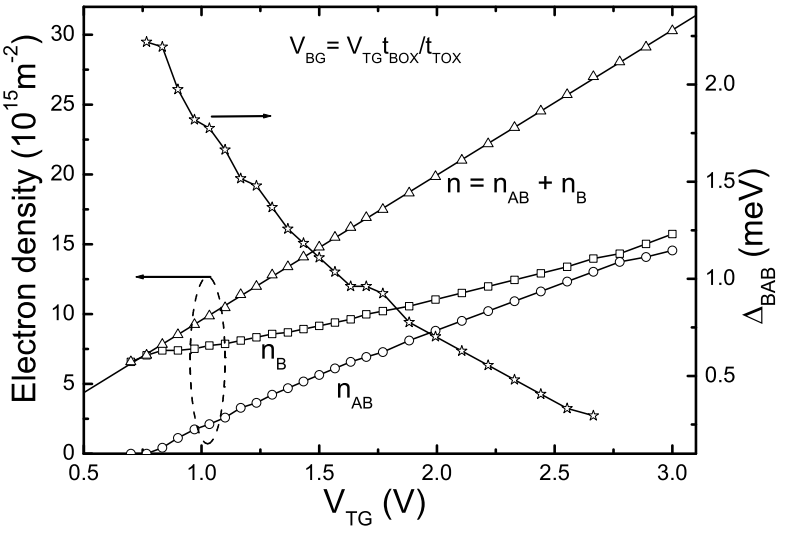

Figure 3.5: *Left axis: Experimental total electron density (n) and sub-band densities (n_B, n_{AB}) as a function of the top gate voltage along the balanced gate line of a 14 nm thick Si well at 270 mK (device F-E42). Right axis: Sub-band energy spacing calculated by substituting n_B and n_{AB} to Eq. (3.6). The densities are determined from the Shubnikov-de Haas oscillations, which are described in Section 4.2.3. After Paper V.*

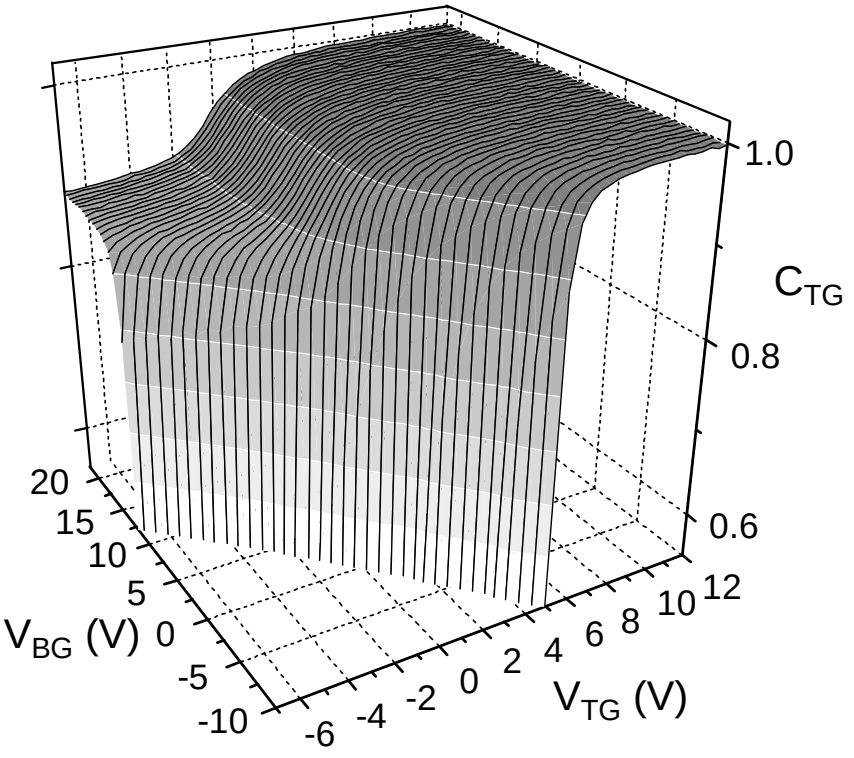

Figure 3.6: *Normalized top gate capacitance of a 17 nm-thick device with $t_{OX} \approx 42$ nm and $t_{BOX} \approx 82$ nm. Data measured at 300 K.*

where $|i\rangle$ is the initial state with energy $\mathcal{E}_i$ and $|f\rangle$ is the final state with energy $\mathcal{E}_f$. Operator H describes the interaction or perturbation which causes the transition $i \to f$.

3.2.1 Elastic scattering

In elastic scattering H is a static potential. Now the states $|i\rangle$ in Eq. (3.9) are (single-particle) electronic states and $|\langle f|\, H\, |i\rangle|^2$ is the square of scattering matrix element $M_{f,i} = M_{i \longrightarrow f} = \int d^3r \Psi_f^*(\mathbf{r}) H \Psi_i(\mathbf{r})$. In this Section we focus on quasi 2D electron systems in quantum wells (see, e.g., Ref. [33] for bulk systems). The relevant elastic scattering mechanisms in quantum wells are charged impurity (Coulomb) scattering and surface roughness scattering. For the former mechanism H is simply the Coulomb interaction potential. If the scattering charges form an infinitely thin plane at z_0 with uncorrelated lateral distance and average 2D density N_C then the total Coulomb scattering overlap integral is given by [1, 34]

$$\left|M^C_{n,n'}(\boldsymbol{q})\right|^2 = N_C V_2^2(q) \left| \int dz \widetilde{G}_{\boldsymbol{q}}(z, z_0) \psi_n^*(z) \psi_{n'}(z) \right|^2, \tag{3.10}$$

where

$$V_d(\boldsymbol{q}) = e^2/4\varepsilon_b \times (2/q)^{d-1} \tag{3.11}$$

is the d-dimensional Fourier transform of the Coulomb interaction (here $d = 2$) and ε_b is the "background" dielectric constant. The momentum $\boldsymbol{q} = \boldsymbol{k}' - \boldsymbol{k}$ describes the momentum transfer in the 2D plane. Normalized Green's function $\widetilde{G}_{\boldsymbol{q}}(z, z_0)$ is the Fourier transform of the electrostatic Green's function $G_{\boldsymbol{q}}(z, z_0)$ divided by $V_2(\boldsymbol{q})$. The Green's function $G_{\boldsymbol{q}}(z, z_0)$ can be solved from Poisson's equation with δ-function source term. For example, for uniform media we have $\widetilde{G}_{\boldsymbol{q}}(z, z_0) = \exp(-q\,|z - z_0|)$. On the other hand, if we are dealing with a system consisting of two different materials with dielectric constants ε_1 and ε_2 joint at $z = 0$ the Green's function $\widetilde{G}_{\boldsymbol{q}}(z, z_0) = \frac{1}{2}(\varepsilon_1 + \varepsilon_2)\varepsilon_2^{-1} \exp(-q\,|z - z_0|) + \frac{1}{2}(\varepsilon_2 - \varepsilon_1)\varepsilon_2^{-1} \exp(-q\,|z + z_0|)$ and $\varepsilon_b = (\varepsilon_1 + \varepsilon_2)/2$. Note that here the latter term gives rise to the so-called image charge effect. This type Green's function can be utilized in inversion layer calculations by substituting $\varepsilon_{1,2} = \varepsilon_{\mathrm{ox,Si}}$. In principle analytical solution for $\widetilde{G}_{\boldsymbol{q}}(z, z_0)$ can be found in a multilayered material. However, even for three layers the functional form of $\widetilde{G}_{\boldsymbol{q}}(z, z_0)$ is rather complicated. [35]

Surface roughness can be described by roughness amplitude $\Delta(\boldsymbol{r})$. Following Ando [36] the perturbation Hamiltonian can be written as $H = V_0\,[\theta(z) - \theta(z - \Delta(\boldsymbol{r}))]$, where V_0 is the potential step due to band offset at the interface (fluctuating interface resides at $z = 0$). The overlap integral is $\int d^2r dz \Psi_n^*(\mathbf{r}, z) H \Psi_{n'}(\mathbf{r}, z) \simeq V_0 \int d^2r \Delta(\boldsymbol{r}) \Psi_n^*(\mathbf{r}, 0) \Psi_{n'}(\mathbf{r}, 0)$ and the square of the matrix element is

$$\left|M_{n,n'}^{SR}(\boldsymbol{q})\right|^2 = V_0^2\,|\Delta(\boldsymbol{q})|^2\,|\psi_n^*(0)\psi_{n'}(0)|^2\,. \tag{3.12}$$

Here $|\Delta(\boldsymbol{q})|^2$ is the power spectrum of the surface roughness. Assuming that for all occupied 2D sub-bands $V_0 \gg E_n$ applies [E_n being the eigen energy in Eq. (3.7)] we can find an analytical approximation for $\psi_n(z)$ close to $z = 0$ [1]. This limiting form is $\psi_n(z) \propto V_0^{-1} \partial\psi_n(0)/\partial z$ which cancels out V_0 and Eq. (3.12) reduces to

$$\left|M_{n,n'}^{SR}(\boldsymbol{q})\right|^2 = |\Delta(\boldsymbol{q})|^2 \left|\frac{\hbar^2}{2m_z} \frac{\partial\psi_n^*(0)}{\partial z} \frac{\partial\psi_{n'}(0)}{\partial z}\right|^2, \tag{3.13}$$

as originally proposed in Ref. [37]. Note that this form of $\left|M_{n,n'}^{SR}(\boldsymbol{q})\right|^2$ gives the well-known average effective field dependency $M_{n,n}^{SR}(\boldsymbol{q}) = \Delta(\boldsymbol{q})\,\langle V_{eff}(z)/\partial z\rangle$ in the case of single interface quantum wells, such as bulk inversion layers and modulation doped heterostructures [38].

In the early works the correlation of the surface roughness at the Si-SiO_2 interface was assumed Gaussian [1]. However, Goodnick *et al.* [39] showed that the roughness is better described by exponential correlation, which leads to power spectrum

$$|\Delta(\boldsymbol{q})|^2 = \frac{\pi\Delta^2 L_c^2}{(1 + q^2L^2/2)^{3/2}}, \tag{3.14}$$

where Δ and L_c are the rms amplitude and the correlation length, respectively. Typical values for Δ and L_c are ~ 0.1 nm and ~ 10 nm, respectively. [1, 39, 40]

3.2.2 Phonon scattering

Phonons are quanta of lattice vibrations. They introduce a spatially and temporarily varying lattice displacement and strain. This strain alters the lattice potential seen by the electrons, which is the source of the electron-phonon interaction. Now the initial $|i\rangle$ and final states $|f\rangle$, which are coupled due to this interaction, consist of phonon states and electronic states. The golden rule expression for the *e-ph* scattering rate between these states is given by [33]

$$W^{\pm\boldsymbol{q}}_{l\boldsymbol{k},l'\boldsymbol{k}'} = \frac{2\pi}{\hbar}\left|\mathcal{M}^{\pm\boldsymbol{q}}_{l\boldsymbol{k},l'\boldsymbol{k}'}\right|^2 (N_{\boldsymbol{q}} + \frac{1}{2} \pm \frac{1}{2})\delta(\mathcal{E}_{l\boldsymbol{k}} - \mathcal{E}_{l'\boldsymbol{k}'} \pm \hbar\omega), \tag{3.15}$$

where $\boldsymbol{q}$ ($\omega = \omega_{\boldsymbol{q}}$) is the phonon wave vector (frequency) and $N_{\boldsymbol{q}}$ is the average of the phonon occupation number. All expression which depend on the wave vector $\boldsymbol{q}$ also depend on the phonon mode index, but this is not written explicitly for the sake of clarity. Electron quantum numbers $l'\boldsymbol{k}'$ ($l\boldsymbol{k}$) correspond to the initial (final) state. In equilibrium $N_{\boldsymbol{q}}$ is given by the Bose-Einstein distribution $N_{\boldsymbol{q}} = N_{T_{ph}}(\omega) = [\exp(\hbar\omega/k_B T_{ph}) - 1]^{-1}$, where T_{ph} is the phonon temperature. [24] The plus and minus sign in Eq. (3.15) correspond to phonon emission and absorption processes, respectively. The single-particle *e-ph* matrix element is defined by

$$\mathcal{M}^{-\boldsymbol{q}}_{l\boldsymbol{k},l'\boldsymbol{k}'} = \int d^3r \Psi^*_{l\boldsymbol{k}}(\boldsymbol{r}) V_{\boldsymbol{q}}(\boldsymbol{r}) \Psi_{l'\boldsymbol{k}'}(\boldsymbol{r}) = \left(\mathcal{M}^{+\boldsymbol{q}}_{l'\boldsymbol{k}',l\boldsymbol{k}}\right)^*, \tag{3.16}$$

where $\Psi_{l\boldsymbol{k}}(\boldsymbol{r})$ is the electron wave function. The interaction potential $V_{\boldsymbol{q}}(\boldsymbol{r})$ depends on the phonon system and also on the "choice" of $\Psi_{l\boldsymbol{k}}(\boldsymbol{r})$. [33] Here we work in a picture where $\Psi_{l\boldsymbol{k}}(\boldsymbol{r})$ is the envelope wave function and, therefore, $V_{\boldsymbol{q}}(\boldsymbol{r})$ is defined by such "macroscopic" effects as the deformation potential coupling and/or piezo electric potential. In this picture the part of $V_{\boldsymbol{q}}(\boldsymbol{r})$ which is due to deformation potential coupling depends on the point or region in the Brillouin zone, i.e., it depends on $\boldsymbol{k}$-space band index. The potential $V_{\boldsymbol{q}}(\boldsymbol{r})$ is proportional to the complex conjugate of strain of a quantum eigen mode of lattice displacement. In the case of bulk continuum (volume V_{ph}) the eigen modes are of the form $\boldsymbol{u} = \sqrt{\hbar/2\rho\omega V_{ph}}\boldsymbol{e}_{\boldsymbol{q}} \exp(i\,\boldsymbol{q}\cdot\boldsymbol{r}) = \boldsymbol{u}_{\boldsymbol{q}} \exp(i\,\boldsymbol{q}\cdot\boldsymbol{r})$, where $\boldsymbol{e}_{\boldsymbol{q}}$ is polarization vector ($|\boldsymbol{e}_{\boldsymbol{q}}| = 1$) and ρ is the mass density of the crystal. We follow the notations of Papers VI and VII and define the strain component vector as $\boldsymbol{\epsilon} = \begin{bmatrix} \epsilon_{xx} & \epsilon_{yy} & \epsilon_{zz} & \epsilon_{xy} & \epsilon_{xz} & \epsilon_{yz} \end{bmatrix}^T$, where $\epsilon_{\alpha\beta} = \frac{1}{2}(\partial u_\alpha/\partial\beta + \partial u_\beta/\partial\alpha)$ are the symmetric strain components of displacement. Now the Fourier components of $\boldsymbol{\epsilon}$ can be written as

$$\boldsymbol{\epsilon}_{\boldsymbol{q}} = iq\widehat{S}\boldsymbol{u}_{\boldsymbol{q}}, \tag{3.17}$$

where the conversion matrix is defined by

$$\widehat{S} = \frac{1}{2}\begin{bmatrix} 2\widetilde{q}_x & 0 & 0 \\ 0 & 2\widetilde{q}_y & 0 \\ 0 & 0 & 2\widetilde{q}_z \\ \widetilde{q}_y & \widetilde{q}_x & 0 \\ \widetilde{q}_z & 0 & \widetilde{q}_x \\ 0 & \widetilde{q}_z & \widetilde{q}_y \end{bmatrix}. \tag{3.18}$$

Here $\widetilde{q}_i = q_i/q$ are components of propagation direction vector. If we assume deformation potential type of interaction the potential shifts due to strain can be written as

$$\delta \boldsymbol{v}_{\boldsymbol{q}} = \widehat{\Xi}\boldsymbol{\epsilon}_{\boldsymbol{q}} = iq\widehat{\Xi}\widehat{S}\boldsymbol{u}_{\boldsymbol{q}}, \tag{3.19}$$

where $\widehat{\Xi}$ is the deformation potential matrix consisting of the deformation potential constants and $\{\delta \boldsymbol{v}_{\boldsymbol{q}}\}_b$ is the band shift for band b. For example, in the case of conduction band of Si [41] $\widehat{\Xi}$ can be written as

$$\widehat{\Xi} = \begin{pmatrix} \Xi_d+\Xi_u & \Xi_d & \Xi_d & 0 & 0 & 0 \\ \Xi_d & \Xi_d+\Xi_u & \Xi_d & 0 & 0 & 0 \\ \Xi_d & \Xi_d & \Xi_d+\Xi_u & 0 & 0 & 0 \\ \Xi_d+\Xi_u & \Xi_d & \Xi_d & 0 & 0 & 0 \\ \Xi_d & \Xi_d+\Xi_u & \Xi_d & 0 & 0 & 0 \\ \Xi_d & \Xi_d & \Xi_d+\Xi_u & 0 & 0 & 0 \end{pmatrix}, \tag{3.20}$$

where $\Xi_{d(u)}$ are the dilatational (uniaxial) deformation potential constants.

The scattering potential for the $\boldsymbol{k}$-space band b is now $V_{\boldsymbol{q}}(\boldsymbol{r}) = \left\{\delta \boldsymbol{v}^*_{\boldsymbol{q}}\right\}_b \exp(-i\boldsymbol{q}\cdot\boldsymbol{r})$. If we split the band index l in Eq. (3.16) as $l = (n, b)$, where n describes spatial 2D sub-band and b is again the $\boldsymbol{k}$-space band index, we find

$$\mathcal{M}^{-\boldsymbol{q}}_{l\boldsymbol{k},l'\boldsymbol{k}'} = \begin{cases} \delta_{\boldsymbol{k}'-\boldsymbol{k},\boldsymbol{q}} \left(\mathcal{M}^{\boldsymbol{q}}_{b,b'}\right)^*, & \text{3D} \\ \delta_{\boldsymbol{k}'_{\shortparallel}-\boldsymbol{k}_{\shortparallel},\boldsymbol{q}_{\shortparallel}} \left(\mathcal{M}^{\boldsymbol{q}}_{b,b'}\mathcal{F}_{n,n'}\right)^*, & \text{2D} \end{cases} \tag{3.21a}$$

$$\mathcal{M}^{\boldsymbol{q}}_{b,b'} = \left\{\delta \boldsymbol{v}_{\boldsymbol{q}}\right\}_b \delta_{b,b'} \tag{3.21b}$$

where the $\delta-$factors arise from the spatial integration over free electron states and give the rule of momentum conservation.[4] The *e-ph* form factor $\mathcal{F}_{n,n'}$ is defined by 1D overlap integral

$$\mathcal{F}_{n,n'} = \int dz \psi^*_n(z) e^{iq_z z} \psi_{n'}(z). \tag{3.22}$$

If $\psi_n(z)$ are plane wave electron states then the 2D matrix elements are equal with the 3D ones, i.e., the *e-ph* form factor gives the conservation of z-direction momentum.

[4]Note that as we have written Eq. (3.21a) for the envelope wavefunctions we have $\mathcal{M}^{\boldsymbol{q}}_{b,b'} = 0$ if $b \neq b'$.

3.2.3 Density response and screening

The response of all electrons to a perturbation, which is the source of scattering, plays an important role. This response together with electron-electron interaction affects the overall perturbation felt by the electron gas. In other words, the bare perturbation and matrix elements are screened, which typically tends to reduce the transition rate of Eq. (3.9). A common approach is to assume that the electronic system can be described with the response of the non-interacting system under the external field plus the induced field of all electrons ignoring all cross-correlations. This method is a standard mean field approach, which is often referred as the random phase approximation (RPA).[5]

In the case of a single band under external field (perturbation), which couples to the system through a potential $v_{ext}(\boldsymbol{q},\omega)$, the dielectric function can be defined as $\varepsilon(\boldsymbol{q},\omega) = v^{eff}(\boldsymbol{q},\omega)/v^{ext}(\boldsymbol{q},\omega)$, where $v^{eff}(\boldsymbol{q},\omega)$ is the screened mean field potential, which is the sum of the external and induced potentials. The matrix elements are screened in a similar fashion and in the many-band case the screened matrix elements are given by

$$M^{\rm scr}_{mm'}(\boldsymbol{q},\omega) = \sum_{nn'} M_{nn'}(\boldsymbol{q},\omega)[\varepsilon^{-1}(\boldsymbol{q},\omega)]_{nn'mm'}, \tag{3.23}$$

where the RPA dielectric function can be written as

$$\varepsilon_{nn'mm'}(\boldsymbol{q},\omega) = \delta_{nm}\delta_{n'm'} - V_{nn'mm'}(\boldsymbol{q})\chi^0_{mm'}(\boldsymbol{q},\omega). \tag{3.24}$$

Here $\chi^0_{mm'}(\boldsymbol{q},\omega)$ is the density response function of non-interacting electron system and element $V_{ii'jj'}(\boldsymbol{q})$ describes the electron-electron Coulomb interaction. For a strictly 2D or 3D system $V_{nn'mm'}(\boldsymbol{q}) = V_d(\boldsymbol{q})$ [see Eq. (3.11)]. Finite span of the electron wave functions in z-direction in quantum wells introduces the Coulomb form factors $F_{nn'mm'}(\boldsymbol{q})$[34, 44]

$$V_{nn'mm'}(\boldsymbol{q}) = F_{nn'mm'}(\boldsymbol{q})V_2(\boldsymbol{q}), \tag{3.25a}$$

$$F_{nn'mm'}(\boldsymbol{q}) = \int dz \int dz' \widetilde{G}_{\boldsymbol{q}}(z,z')\psi^*_n(z)\psi_{n'}(z)\psi^*_m(z')\psi_{m'}(z'), \tag{3.25b}$$

where $\widetilde{G}_{\boldsymbol{q}}(z,z')$ is the electrostatic Green's function, which was already discussed in connection with the Coulomb matrix elements, and $\psi_j(z)$ are the solutions of Eq. (3.7). In the long wavelength limit and/or zero coupling between the bands Eq. (3.24) can be simplified to matrix relation (see, e.g., Refs. [34, 45–47])

$$\widehat{\varepsilon}(\boldsymbol{q},\omega) = \widehat{1} - \widehat{V}\widehat{\chi}^0(\boldsymbol{q},\omega). \tag{3.26}$$

[5] RPA and screening in 3D systems is broadly discussed, e.g., in Refs. [42, 43]. Transparent analysis of 2D sub-bands can be found from Refs. [34, 44]. RPA typically works best at high densities, but also generally speaking it provides a useful tool to investigate interacting electron gas. Further discussion about the range of validity of the RPA can be found from Refs. [42, 43].

The elements $\widehat{V}_{ij} = V_{ij} = V_d(\boldsymbol{q})F_d^{ij}(\boldsymbol{q})$, where in 2D (3D) $F_{d=2}^{ij}(\boldsymbol{q}) = F_{iijj}(\boldsymbol{q})$ ($F_{d=3}^{ij}(\boldsymbol{q}) = 1$). Note that if the electron system consists of fully overlapping 2D/3D sub-systems or two 2DEG layers separated by distance z_0, then the Coulomb form factor can be written as $F_d^{ij}(\boldsymbol{q}) = \left[\delta_{ij} + (1-\delta_{ij})\exp(-qz_0)\right]^{3-d}$ (provided that $1/q$ greatly exceeds the width of the individual layers in 2D).

The polarization function of a clean non-interacting system is defined by [34, 43]

$$\chi_{ij}^0(\boldsymbol{q},\omega) = \lim_{\alpha\longrightarrow 0^+} V_e^{-1}\sum_{\boldsymbol{k}} \frac{f^0\left(\mathcal{E}_{i\boldsymbol{k}}\right) - f^0\left(\mathcal{E}_{j\boldsymbol{k}+\boldsymbol{q}}\right)}{\hbar\omega + \mathcal{E}_{i\boldsymbol{k}} - \mathcal{E}_{j\boldsymbol{k}+\boldsymbol{q}} - i\hbar\alpha}, \tag{3.27}$$

V_e being the d-dimensional volume of the electron system. The well-known zero-Kelvin expressions for diagonal terms $\chi_{ii}^0(\boldsymbol{q},\omega)$ were first obtained by Lindhard [48] in 3D and by Stern in 2D [49]. Expressions for the non-diagonal terms in 2D can be found, e.g., from Refs. [50, 51]. We will often encounter a symmetric form of χ_{ij}^0 where the diagonal χ_d and and off-diagonal χ_{od} elements are equal, respectively. In this case we write $\chi_{ij}^0(\boldsymbol{q},\omega)$ in matrix form as

$$\widehat{\chi}^0(\boldsymbol{q},\omega) = \chi_0^0(\boldsymbol{q},\omega)\widehat{1} + \chi_1^0(\boldsymbol{q},\omega)\widehat{Q}_A, \tag{3.28}$$

where $\widehat{Q}_A = \widehat{1} - \widehat{Q}_S$ with $\{\widehat{Q}_S\}_{ij} = 1/L$ (L is the number of bands) and these matrices have a useful property $\widehat{Q}_i\widehat{Q}_j = \delta_{ij}\widehat{Q}_i$. The functions $\chi_0^0(\boldsymbol{q},\omega)$ and $\chi_1^0(\boldsymbol{q},\omega)$ are defined through relations $\chi_0^0 = \chi_d + (L-1)\chi_{od}$ and $\chi_1^0 = -L\chi_{od}$.

Diagonal terms $\chi_{ii}^0(\boldsymbol{q},\omega)$ of Eq. (3.27) at $T = 0$ can be approximated by a useful and illustrative small-$\boldsymbol{q}$ formula

$$\chi^0(\boldsymbol{q},\omega) \equiv \chi_{ii}^0(\boldsymbol{q},\omega) \simeq -\nu(\varepsilon_F)\left[1 + i\frac{\omega}{qv_F}K_d\left((\frac{\omega}{qv_F} + \frac{q}{2k_F})^2 - \frac{2\hbar\omega}{\varepsilon_F}\right)\right], \tag{3.29}$$

where $K_d(x) = (\pi/2)^{d-2}\theta\left(1-x\right)\left(1-x\right)^{(d-3)/2}$ and all variables are evaluated at the Fermi level ε_F of the particular band. The static diagonal response $\chi^0(\boldsymbol{q}) = \chi^0(\boldsymbol{q},0)$ is given by [48, 49]

$$\chi^0(\boldsymbol{q}) = -\nu(\varepsilon_F) \times \begin{cases} \left[\frac{1}{2} + \frac{x^2-1}{4x}\ln\left|\frac{x-1}{x+1}\right|\right], & \text{3D} \\ \left[1 - \mathrm{Re}\sqrt{1-x^{-2}}\right], & \text{2D} \end{cases} \tag{3.30}$$

where $x = \frac{q}{2k_F}$. For $x \ll 1$ the response function $\chi^0(\boldsymbol{q}) = -\nu$. Whereas, in the opposite limit it goes to zero. Finite temperature and/or disorder smears the sharp features of (especially 2D) $\chi_{ij}^0(\boldsymbol{q},\omega)$ and $\chi_{ij}^0(\boldsymbol{q},0)$.[6] The finite temperature correction can be calculated from $\chi_{ij}^0(\boldsymbol{q},\omega)\big|_{T=0}$ by the method of Maldaque. [53] In the limit of Boltzmann statistics [$f^0\left(\mathcal{E}\right) \simeq e^{-(\mathcal{E}-\mathcal{E}_F)/k_BT}$] the static diagonal polarizability is given by ($d = 2, 3$) [54, 55]

$$\begin{aligned} \chi^0(\boldsymbol{q}) &= \frac{n}{k_BT}g_1(x), \\ g_1(x) &= \frac{4\sqrt{\pi}}{x}e^{-x^2}\int_0^x dt e^{t^2}, \end{aligned} \tag{3.31}$$

[6] Note that the effects of disorder and temperature are not additive. [52]

where $x = q\lambda$ and $\lambda = (2\pi\hbar^2/mk_BT)^{1/2}$ is the thermal wave length ($n = n_i$). The static polarizabilities of Eqs.(3.30) and (3.31) are plotted in Fig. 3.7.

In addition of broadening effects the disorder slows down the response of the electrons, i.e., disorder affects the dynamical properties of polarizability. The effect of disorder can be phenomenologically taken into account by Mermin's relaxation time approach [56], where the disorder included in a phenomenological relaxation rate $\gamma = 1/\tau$. In a multi-band system one should distinguish between intra-sub-system and inter-sub-system scattering rates, which we denote by γ_0 and γ_1, respectively. For L equivalent bands the total scattering rate is given by $1/\tau = \gamma = \gamma_0 + (L-1)\gamma_1$. Components of Eq. (3.28) in the diffusive (hydrodynamic) limit $\omega\tau, ql_e \ll 1$ are given by the many-band version of Mermin's relaxation time response function [57]

$$\chi_0^0(\boldsymbol{q},\omega) = -\nu\frac{iD_0q^2}{\omega + iD_0q^2}, \tag{3.32a}$$

$$\chi_1^0(\boldsymbol{q},\omega) = \chi^0(\boldsymbol{q},\omega)\frac{\omega}{iD_0q^2}\frac{i\overline{\gamma}}{(\omega + i\overline{\gamma}) + iD_0q^2}, \tag{3.32b}$$

where $D_0 = \frac{1}{d}v_F^2\tau = \frac{1}{d}v_F l_e$ is the diffusion constant and $\overline{\gamma} = \frac{L}{2}\gamma_1$is the total elastic inter-valley/band scattering rate.

If we assume single (or degenerate) band and $F_d(\boldsymbol{q}) = 1$ then from Eq. (3.24) we obtain the the standard RPA dielectric function $\varepsilon(\boldsymbol{q},\omega) = 1 - V(\boldsymbol{q})\chi^0(\boldsymbol{q},\omega)$. If we consider the static limit [Eq. (3.30)] and further assume $\frac{q}{k_F} \ll 1$ we find the well-known Thomas-Fermi dielectric function $\varepsilon(\boldsymbol{q}) = 1+(\kappa/q)^{d-1}$, where $\kappa = 2\left[e^2\nu/4\varepsilon_b\right]^{1/(d-1)}$ is the Thomas-Fermi screening wave vector. In the limit of Boltzmann statistics [Eq.

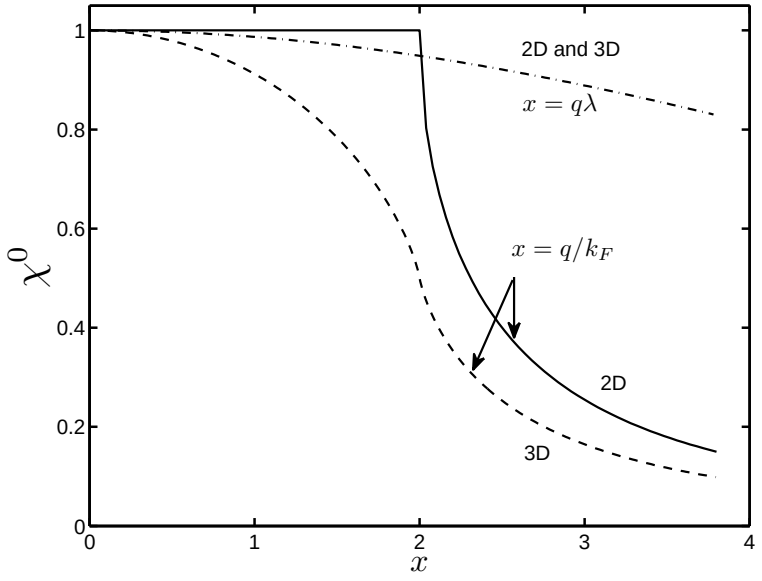

Figure 3.7: *Normalized static polarizability $\chi^0(x,0)/\chi^0(0,0)$ as a function of normalized wave vector x. Curves with $x = \frac{q}{k_F}$ and $x = q\lambda$ correspond to Eq.(3.30) and Eq. (3.31), respectively.*

(3.31)] at $q\lambda \ll 1$ we obtain the Debye-Hückel screening wave vector by replacing ν by n_l/k_BT in κ. Note that the length scale $1/\kappa$ is the distance where electrons can screen a static long wave length potential. More generally we can write $\varepsilon(\boldsymbol{q},\omega) = 1 + (\widetilde{\kappa}/q)^{d-1}$ where $\widetilde{\kappa} = -\kappa\left[\chi^0(\boldsymbol{q},\omega)/\chi^0(0,0)\right]^{1/(d-1)}$, which introduces the frequency and wave vector dependent screening wave vector $\widetilde{\kappa}$ (see also Fig. 3.7).

The inversion of the RPA dielectric function in the general many-band case is a formidable task for an arbitrary system, even for the simplified model of Eq. (3.26). A physically transparent and useful model for arbitrary number (L) of sub-systems (or bands) is such where we assume the form of Eq. (3.28) for $\widehat{\chi}^0(\boldsymbol{q},\omega)$. If we further assume that all intra-band interactions and all inter-band interactions are similar, respectively, $[V_{ij} = \delta_{ij}V_{11} + (1-\delta_{ij})V_{12}]$ we find from Eq. (3.26)

$$\widehat{\varepsilon}^{-1}(\boldsymbol{q},\omega) = \varepsilon_S^{-1}(\boldsymbol{q},\omega)\widehat{Q}_S + \varepsilon_A^{-1}(\boldsymbol{q},\omega)\widehat{Q}_A, \tag{3.33}$$

where the scalar dielectric functions are $\varepsilon_S(\boldsymbol{q},\omega) = 1 - [V_{11} + (L-1)V_{12}]\,\chi_0^0(\boldsymbol{q},\omega)$ and $\varepsilon_A(\boldsymbol{q},\omega) = 1 - (V_{11} - V_{12})\,[\chi_0^0(\boldsymbol{q},\omega) + \chi_1^0(\boldsymbol{q},\omega)]$. We can recognize that these both have a similar form as the standard RPA dielectric function. Dielectric functions $\varepsilon_{S,A}(\boldsymbol{q},\omega)$ often appear in context to bi-layer Coulomb drag effect [58]. The poles of $\varepsilon_{S,A}^{-1}(\boldsymbol{q},\omega)$ are related to symmetric (optical) and asymmetric (acoustic) plasmons, respectively. [59, 60]

Note that if there exists asymmetric coupling to the external field then it may be that the charge responses of the bands are in opposite phase (due to inter-band Coulomb interaction), which tends to reduce the total density response and, therefore, also reduce the overall screening. This phenomenon resembles the conventional image charge effect and, therefore, it was referred as "internal image charge effect" in Paper VII. This effect quantitatively follows from Eq. (3.33) (from the properties of matrices $\widehat{Q}_i$) and it is schematically illustrated in Fig. 3.8.

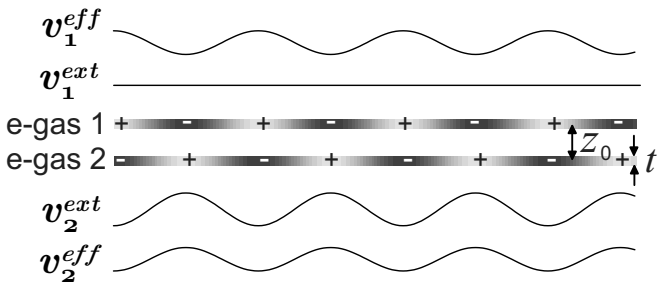

Figure 3.8: *Schematic cross-section of a 2D two-component electron system and illustration of reduction of screening under asymmetrically coupling field. The electron gases have thickness t and they are separated by a distance z_0. Note that $z_0 > 0$ describes a bi-layer, where as $z_0 = 0$ describes a many-valley/band system, where the components are separated in reciprocal space. The solid curves describe the external (v_l^{ext}) and effective (v_l^{eff}) scalar coupling potentials in the plane of electron gas $l = 1, 2$. The $\pm$ signs describe the charge build up due to the external (and effective) field in the two electron gases. After Paper VII.*

Chapter 4

Transport in quantum wells

This part of the Thesis is based on Papers I–V and it deals with 2D electronic transport phenomena in quantum wells. Electronic properties of 2D systems has been a topical subject since the early studies on bulk Si MOSFETs in the 1960's. [28] The understanding gathered from the subject from 1960's up to early 1980's is reviewed in Ref. [1]. Since then a lot of efforts have been concentrated around III-V compound semiconductor heterostructure based 2D systems due to their excellent electronic properties. In heterostructure quantum wells the low temperature mobility can exceed 1000 m^2/Vs leading to electron mean free paths of tens of microns. [61] Whereas, in Si MOSFETs the mobility seems to be fundamentally limited (due to the properties of the Si-SiO_2 interface) below 10 m^2/Vs, the record being around 7 m^2/Vs [62].

Ultra-high mobility is not always a necessity and profound effects can also be due to disorder. Therefore, both heterostructure quantum wells and Si MOSFETs are still utilized as a laboratory of 2D transport physics. High mobility of carriers means also high switching speed for the particular FET and for the circuit. Even so, compound semiconductor FETs are typically utilized only in high speed analog devices, while commercial integrated digital circuits, such as processors, are build from Si MOSFETs. This distribution of work between III-V's and Si is due to advanced silicon device processing technology, robust material properties of Si and existence of stable SiO_2 gate oxide. They have enabled reliable large scale integration of the transistors and FET scaling.

The quantum well system of interest here is the SiO_2-Si-SiO_2 structure introduced in Sections 2.1.1 and 3.1.2. This Si heterostructure, where single crystalline Si film is sandwiched between amorphous SiO_2 layers, is enabled by the development of silicon-on-insulator technology. [3, 4] The SiO_2-Si-SiO_2 heterostructure provides a new quantum well system, which enables insertion of both a metallic top gate and back gate electrode forming a double-gate Si MOSFET. Si-based double-gate FET structures are intensively explored at the moment. [4, 5] They are regarded as a promising solution to the problems

faced when the device/gate length is down-scaled into sub-50 nm regime. Double-gate geometry gives a superior electrostatic gate control of the transistor channel charge, which reduces the so-called short channel effects. In addition of boosting the gate control such devices provide also another benefit in the form of enhanced electron mobility in comparison to similar single-gate FETs. [63] From the viewpoint of low temperature 2D transport physics development double-gate Si MOSFETs provides a Si quantum well system where spatial sub-bands and electron wave functions can be easily adjusted.

Here we first review simple Drude-Boltzmann transport theory, which provides qualitative understanding for the experimental findings at low magnetic fields. Then we discuss the experimental low temperature transport properties of double-gate SiO_2-Si-SiO_2 FETs with $\sim$ 5–20 nm Si layer. The maximum single-sub-band mobility of the fabricated devices is found to be above 2 m^2/Vs, which is comparable to maximum mobilities found in high-mobility bulk Si MOSFETs. The double-gate structure enables the occupation the second spatial sub-band even at low electron densities and it is demonstrated that the number of quantum mechanical spatial 2D sub-bands has a strong effect on the transport. Such effects are washed away at elevated temperatures. The most relevant effect at room temperature is the above mentioned mobility enhancement, which we demonstrate at the end of this part.

4.1 Conductivity and mobility within Drude-Boltzmann picture

At small driving electric fields $\boldsymbol{E}$ we expect that the current density $\boldsymbol{J}$ is given by Ohm's law

$$\boldsymbol{J} = \sigma \boldsymbol{E}, \tag{4.1}$$

where σ is the conductivity. Simplest model for the conductivity is known as the Drude model. It assumes that the density of current carrying electrons is n_e and that there exist a (some kind of) frictional damping force. The damping is described by parameter τ in such a way that the model gives $\exp(-t/\tau)$ decay of the electron velocity if we set $\boldsymbol{E} = 0$ at $t = 0$, which gives the name relaxation time for τ. The Drude model gives for the conductivity [19]

$$\sigma = e\mu n_e \tag{4.2a}$$

$$\mu = e\tau/m, \tag{4.2b}$$

where μ is the mobility and it relates the average (drift) velocity v_D of the carriers to electric field according to $v_D = \mu\,|E|$.

The above model merely introduces an extra parameter (the relaxation time), which is used to determine the conductivity. More complete picture requires the knowledge electron distribution functions $f_l(\boldsymbol{k})$ (of band l) under driving electric field, whence we can calculate the current density from the microscopic definition

$$\boldsymbol{J} = -e \int \frac{d^d k}{(2\pi)^d} \sum_l \boldsymbol{v}_{l\boldsymbol{k}} f_l(\boldsymbol{k}), \tag{4.3}$$

where $\boldsymbol{v}_{l\boldsymbol{k}}$ is the electron velocity. The distribution functions can be obtained from a set of coupled continuity equations in $2d$-dimensional phase space known as Boltzmann transport equation (BTE) [33, 34]

$$\frac{\partial f_l(\boldsymbol{k})}{\partial t} + \mathbf{v} \cdot \nabla_r f_l(\boldsymbol{k}) + \frac{1}{\hbar} \boldsymbol{F} \cdot \nabla_k f_l(\boldsymbol{k}) = \left(\frac{\partial f_l(\boldsymbol{k})}{\partial t} \right)_c . \tag{4.4}$$

Here $\boldsymbol{F} = -e\boldsymbol{E}$ is the force acting on carriers. The term on the right-hand-side of BTE is the collision integral, which introduces (internal) scattering events in the BTE and coupling between the bands. The collision integral is given by the balance equation [33]

$$\left(\frac{\partial f_l(\boldsymbol{k})}{\partial t} \right)_c = \sum_{l'\boldsymbol{k}'} \left\{ [1 - f_l(\boldsymbol{k})] \, W_{l\boldsymbol{k},l'\boldsymbol{k}'} f_{l'}(\boldsymbol{k}') - [1 - f_{l'}(\boldsymbol{k}')] \, W_{l'\boldsymbol{k}',l\boldsymbol{k}} f_l(\boldsymbol{k}) \right\}, \tag{4.5}$$

where $W_{l\boldsymbol{k},l'\boldsymbol{k}'}$ are the transition rates introduced in Section 3.2. Factors $f_{l_i}(\boldsymbol{k}_i)$ and $1 - f_{l_f}(\boldsymbol{k}_f)$ guarantee that the initial and final states are filled and empty, respectively. Approximate analytical solution to BTE can be found at small fields by linearization. The solution which is linear in $\boldsymbol{F}$ is given by [64]

$$f_l(\boldsymbol{k}) = f^0(\mathcal{E}_{l\boldsymbol{k}}) - \frac{\partial f^0(\mathcal{E}_{l\boldsymbol{k}})}{\partial \mathcal{E}_{l\boldsymbol{k}}} \boldsymbol{v}_{l\boldsymbol{k}} \cdot \boldsymbol{F} \tau_l(\boldsymbol{k}), \tag{4.6}$$

where$f^0(\mathcal{E})$ is the Fermi distribution. At this point we set $d = 2$, whence the relaxation time $\tau_l(\boldsymbol{k})$ in the case of elastic or quasi-elastic scattering is defined by system of linear equations [1, 64, 65]

$$\tau_l = k_l^{-1} \sum_{l'} \left\{ \widehat{K}^{-1} \right\}_{ll'} k_{l'} \tag{4.7a}$$

$$\widehat{K}_{ll'} = \delta_{ll'} \sum_m \gamma_{lm}^{\mathrm{qu}} - \gamma_{ll'}^{\mathrm{qu}} + \gamma_{ll'}^{\mathrm{tr}} \tag{4.7b}$$

$$\gamma_{lm}^{\mathrm{qu}} = \frac{m_\parallel}{2\pi\hbar^3} \int_0^{2\pi} d\phi \, |M_{lm}^{\mathrm{scr}}(\boldsymbol{q})|^2 \tag{4.7c}$$

$$\gamma_{lm}^{\mathrm{tr}} = \frac{m_\parallel}{2\pi\hbar^3} \int_0^{2\pi} d\phi (1 - \cos\phi) \, |M_{lm}^{\mathrm{scr}}(\boldsymbol{q})|^2 . \tag{4.7d}$$

Momentum $\boldsymbol{q}$ is defined by in plane momentum transfer in the 2DEG and we have assumed ideal 2D density of states. Angle ϕ is the scattering angle and $M_{lm}^{\mathrm{scr}}(\boldsymbol{q})$ is the screened scattering matrix element. The time scales $1/\gamma_{lm}^{\mathrm{qu}}$ and $1/\gamma_{lm}^{\mathrm{tr}}$ are typically

referred as quantum life time and transport life time, respectively. By substituting Eq. (4.6) into Eq. (4.3) leads to [64]

$$\sigma = e\sum_l \mu_l n_l \tag{4.8a}$$

$$\mu_l = \frac{e\eta_l}{m_\parallel n_l}\int \frac{d^2k_l}{(2\pi)^2}\left[\mathcal{E}_{l\boldsymbol{k}} - E_l\right]\left(-\frac{\partial f^0}{\partial \mathcal{E}_{l\boldsymbol{k}}}\right)\tau_l, \tag{4.8b}$$

where η_l is the number of equivalent bands and $\tau_l(\boldsymbol{k}) = \tau_l(\mathcal{E}_{l\boldsymbol{k}})$. At low temperatures $[(\mathcal{E}_F - E_l)/k_BT \gg 1]$ the sub-band mobility is given by

$$\mu_l = \frac{e}{m_\parallel}\tau_l(k_{F,l}), \tag{4.9}$$

which resembles the standard Drude result with the exception that the transport relaxation time τ_l is evaluated at Fermi level $\mathcal{E}_{F,l} = \mathcal{E}_F - E_l = \left(\hbar k_{F,l}\right)^2/2m_\parallel$.

4.2 Low temperature transport

4.2.1 Single sub-band conductivity and mobility

If the quantum well width is sufficiently small and/or electron density is low only single 2D sub-band is populated, in which case the conductivity is defined by the transport relaxation rate $\tau^{-1} = \gamma_{11}^{\mathrm{tr}}$:

$$\begin{aligned}\tau^{-1} &= \frac{m_\parallel}{2\pi\hbar^3}\int_0^{2\pi} d\phi(1-\cos\phi)\left|M^{\mathrm{scr}}(\boldsymbol{q})\right|^2 \\ &= \frac{m_\parallel}{2\pi\hbar^3}\int_0^2 \frac{dx}{\sqrt{1-(x/2)^2}}\left(\frac{x}{2}\right)^2\left|M^{\mathrm{scr}}(xk_F)\right|^2.\end{aligned} \tag{4.10}$$

The relevant scattering mechanisms at low temperatures are surface roughness scattering and Coulomb scattering, which are described by Eqs. (3.10)–(3.12). If we assume that these scatterers are statistically uncorrelated the total screened matrix element entering Eq. (4.10) is given by the sum $\left|M^{\mathrm{scr}}_{\mathrm{tot}}(\boldsymbol{q})\right|^2 = \left|M^{\mathrm{SR}}(\boldsymbol{q})/\varepsilon(\boldsymbol{q})\right|^2 + \left|M^{\mathrm{C}}(\boldsymbol{q})/\varepsilon(\boldsymbol{q})\right|^2$. We exclude the effect of inter-valley scattering, which has been a widespread practice in the studies Si based 2DEGs.[1]

For screened Coulomb matrix element we have $\left|M^{\mathrm{C}}(\boldsymbol{q})/\varepsilon(\boldsymbol{q})\right|^2 = (N_C e^2/2\varepsilon_b) \times \left|F(q,z_0)/\left[q+\kappa F(q)\right]\right|^2$, where the form factors $F(q,z_0) = \int dz \exp(-q\left|z-z_0\right|)\left|\psi(z)\right|^2$ and $F(q) = \int dz\left|\psi(z)\right|^2 F(q,z)$ (we have assumed uniform dielectric background). Si based 2DEGs are strongly screening systems ($\kappa > k_F$) for realistic carrier densities (n_e

[1] However, recently some progress has been made: a theory of quantum corrections of resistivity, which includes inter-valley scattering, has been developed and utilized in interpretation of experimental data. [66]

below $\sim 50 \times 10^{16}$ m^{-2}). This suggests that the q dependency of the screened Coulomb matrix element is determined by the ratio $F(q, z_0)/F(q)$, which decreases as a function of q. [1] As a result Coulomb scattering limited mobility μ_C increases as a function of k_F or n_e. This makes the Coulomb scattering most effective scattering mechanism at low carrier densities. From Eq. (3.12) for surface roughness scattering we have $\left|M^{\rm SR}(\boldsymbol{q})/\varepsilon(\boldsymbol{q})\right|^2 = \frac{V_0^2|\Delta(\boldsymbol{q})|^2|\psi(0)|^2}{|1+F(q)\kappa/q|^2}$ (for interface at $z = 0$). The magnitude of the electron wave function $|\psi(0)|$ increases at the barrier-well (SiO_2-Si) interfaces as a function the carrier density due to electron-electron interaction and/or external gate potential. Now as $|\Delta(\boldsymbol{q})|^2 = \frac{\pi\Delta^2 L_c^2}{(1+q^2L^2/2)^{3/2}}$ [Eq. (3.14)] the screened surface roughness matrix element has relatively weak q-dependency and, as a result, the k_F-dependency is actually dominated by $|\psi(0)|$. This leads to opposite density dependency in comparison to Coulomb scattering: surface roughness scattering limited mobility $\mu_{\rm SR}$ decreases as a function of k_F or n_e.

The very different density dependency of $\mu_{\rm SR}$ and $\mu_{\rm C}$ leads to well-known behavior of the total mobility $\mu = \mu_{\rm SR}\mu_{\rm C}/(\mu_{\rm SR} + \mu_{\rm C})$ in a FET: the mobility first increases at low carrier densities and then decreases at higher densities. This behavior is experimentally demonstrated in Fig. 4.1 which shows low temperature mobility of two devices in a single sub-band regime. The mobility of the thicker device with $t_W = 16.5$ nm is plotted as a function of the carrier density [Fig. 4.1(a)]. The two curves in the Figure are obtained by controlling the electron density by the top gate (back gate) while keeping the back gate (top gate) at zero, which pulls the 2DEG against the top gate oxide -Si interface (back gate oxide -Si interface). The top interface maximum mobility goes above 2 m^2/Vs below 1 K. The difference in the top/back interface mobility curves arises mainly from a larger interface roughness of the back gate oxide -Si interface. If finite bias is applied to both gates second sub-band gets populated even at relatively low carrier density in thick Si wells (see next Sub-sections). If t_W is sufficiently small single sub-band transport is maintained at arbitrary gate balance. Figure 4.1(b) shows mobility and carrier density contours as a function of the top and back gate voltages measured from such a device ($t_W = 7.0$ nm). Note that if we adjust the gate voltages along an arbitrarily chosen straight line (direction) in Fig. 4.1(b) in such a fashion that n_e increases the mobility shows exactly the similar $\mu(n_e)$ behavior as the thicker device which is due to the interplay of surface roughness and Coulomb scattering. However, the peak mobility in the thinner device is significantly lower than in the thicker one due reduced average distance to the elastic scatterers. See Paper I for t_W dependency of the peak mobility.

4.2.2 Two sub-band conductivity and mobility

If thermal and disorder broadening are sufficiently small the onset of the second sub-band can have a strong effect on the conductivity and mobility. In fact, in the ideal

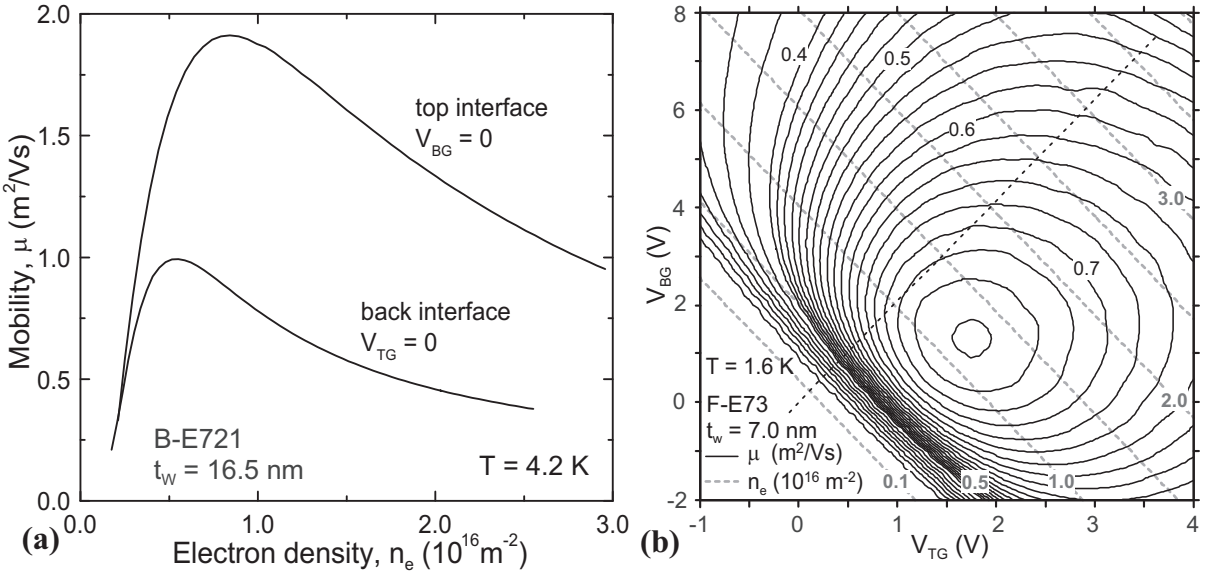

Figure 4.1: *(a) Top and back interface mobility μ as a function of carrier density n_e at 4.2 K. The difference between the curves reflects the different disorder the top and back gate oxide–Si interfaces. (b) Contour plot of μ (black thin curves with black labels) and n_e (gray thick dashed curves with gray bold labels) measured from the 7.0 nm thick Si well at 1.6 K. The contour spacing for μ above (below) 0.4 m^2/Vs is 0.02 m^2/Vs (0.05 m^2/Vs). The dashed line is the symmetric gate bias line $V_{BG} = V_{TG} t_{BOX}/\ t_{OX}$. Carrier density is dermined from the Hall effect and quantum oscillations of resistivity in (a) and (b), respectively [see Section 4.2.3]. After papers III and IV.*

case of zero broadening (and temperature), a discontinuity in the conductivity/mobility is expected due to the jump in the density of states [see Eq. 3.4]. This can be observed by inverting $\widehat{K}$ in Eq. (4.7b) and thereby obtaining τ_1 and τ_2:

$$\begin{pmatrix} \tau_1 \\ \tau_2 \end{pmatrix} = \frac{1}{K_{11}K_{22} - K_{12}^2} \begin{pmatrix} K_{22}/k_1 & -K_{12}/k_1 \\ -K_{12}/k_2 & K_{11}/k_2 \end{pmatrix} \begin{pmatrix} k_1 \\ k_2 \end{pmatrix}. \tag{4.11}$$

If the Fermi level is just above E_2 we have $0 < k_2 \ll k_1$. Furthermore, it is expected that the intra-band terms $K_{11,22}$ dominate over inter-band term K_{12} and we find from Eq. (4.11) $\tau_1^{-1} \simeq K_{11} = \gamma_{11}^{\rm tr} + \gamma_{12}^{\rm qu}$. When k_2 is close to zero $\gamma_{12}^{\rm qu} \simeq \frac{m_\parallel}{\hbar^3} |M_{12}^{\rm scr}(k_1)|^2$, which gives the magnitude of the jump in τ_1^{-1} at the threshold of the second sub-band. At the threshold $n_2 = 0$ and the total conductivity $\sigma = e n_1 \mu_1 = e^2 n_1 \tau_1 / m_\parallel$, which results in an abrupt drop also in σ. Figure 4.2 shows sub-band densities and conductivity as a function of the back gate voltage at constant top gate bias $V_{\rm TG} = 1.75$ V of a Si well with $t_W = 17$ nm. The data exhibits the suggested conductivity degradation when the second sub-band starts to populate. A similar effect has been observed in a III-V heterostructure quantum wells. [67] Note that despite the low temperature there is no sudden drop in σ. The smooth behavior is most likely due to disorder broadening.

Even though we explained the conductivity drop in Fig. 4.2 by BTE-based considerations (Sec. 4.1), it should be noted that for very small n_2 BTE-description is actually expected to fail. This is because at low n_2 we inevitably have for the 2nd sub-band $k_F l_e \lesssim 1$, which indicates strong disorder, and the validity of the semiclassical BTE-approach requires the opposite limit (weak disorder) $k_F l_e \gg 1$. [34] In the limit of strong disorder close to $n_2 = 0$ the carriers in the 2nd sub-band are expected to reside in the localized band tail states. [68–70] Therefore, close to $n_2 = 0$ we can actually view the behavior of the total system in such a way that due to electron-electron interactions the electrons in the localized band tail states of the 2nd sub-band scatter the mobile electrons in the first sub-band, which leads to reduction in μ_1 (and σ) as originally discussed by A. B. Fowler [68] in context with bulk MOSFET mobility experiments.

Figures 4.3(a) and 4.3(b) show contour plot of conductivity as a function of gate voltages measured from a thin well device with $t_{\rm w} = 7$ nm and a thicker well device with $t_{\rm w} = 14$ nm, respectively. The $\sigma(V_{\rm TG}, V_{\rm BG})$ contours of the single sub-band thin

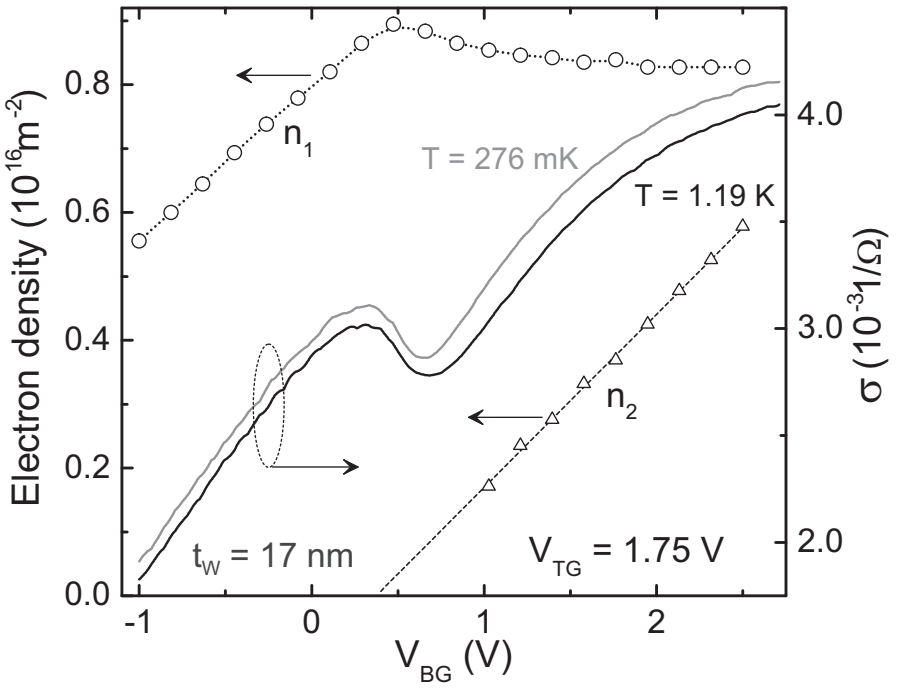

Figure 4.2: *Left axis: Symbols are experimental sub-band densities (n_1, n_2) measured as a function of the back gate voltage from a 17 nm thick Si well (device B-E711) at constant top gate bias $V_{TG} = 1.75$ V at 270 mK. The dotted curve is a spline fit to n_1 and it serves as a guide to the eye. The dashed line is a least of squares fit to n_2. The densities are determined from the quantum oscillations of diagonal resistivity [see Section 4.2.3]. Below $V_{BG} \sim 1$ V n_2 cannot be detected due to large level broadening. Right axis: Experimental conductivity as a function of the back gate voltage.*

well device, which here serves merely as a reference, behave perfectly smoothly [Fig. 4.3(a)].The conductivity of the thicker device [Fig. 4.3(b)] shows strong non-monotonic features, e.g., close to $V_{\rm TG} \approx 0$ and $V_{\rm BG} \approx 0$, which are due to the onset of the 2$^{\rm nd}$ sub-band population as discussed above. There is also another feature which distinguishes $\sigma(V_{\rm TG}, V_{\rm BG})$ of the thin and the thicker device. Around balanced gate bias line ($V_{\rm BG} = V_{\rm TG} t_{\rm BOX}/t_{\rm OX}$) some extra curvature develops above $V_{\rm TG} \approx 1.5$ V in the σ contours of the thicker device, while again no such effect is observed for the thinner one. The origin of this feature is related to the sub-band wave function delocalization in the Si quantum well: at balanced gate bias the effective self-consistent potential in the well forms a symmetric double well structure and the sub-band wave functions spread throughout the well [see Figs. 3.4(a) and (b)]. If the external gates are not biased according to $V_{\rm BG} = V_{\rm TG} t_{\rm BOX}/t_{\rm OX}$ then the effective potential is asymmetric and, according to the rules of quantum mechanics, the wave functions are localized to the different sides of the Si well. The reason why this localization/delocalization leads to such a strong feature in $\sigma(V_{\rm TG}, V_{\rm BG})$ is due to the fact that the different Si-SiO$_2$ interfaces have different disorder; at $V_{\rm BG} = V_{\rm TG} t_{\rm BOX}/t_{\rm OX}$ both sub-bands feel the higher disorder Si-back gate oxide interface leading to reduction in conductivity. This effect has been observed also

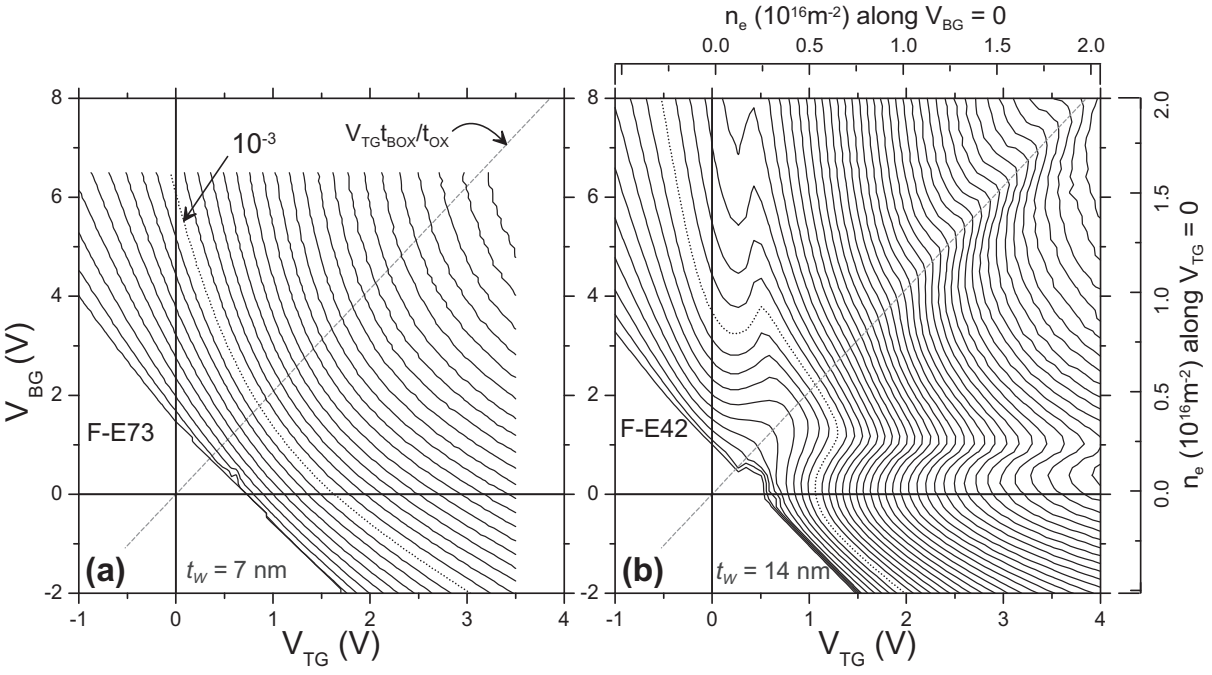

Figure 4.3: *Contour plot of conductivity as a function of the top and back gate voltages of devices (a) F-E73 ($t_w = 7$ nm) and (b) F-E42 ($t_w = 14$ nm) at $T = 270$ mK. The contour spacing is $10^{-4} 1/\Omega$ and the dashed curve is $\sigma = 10^{-3} 1/\Omega$ contour. The outer axis in (b) show the carrier density of F-E42 along $V_{TG,BG} = 0$. The carrier density of device F-E73 is roughly the same [exact values with mobility are plotted in Fig. 4.1 (b)]. (b) is After Paper V.*

in III-V heterostructure bi-layer quantum well systems and it is often referred as the resistance resonance [6–8]. In the III-V systems the double well potential is (mainly) due to stacking materials with different band gaps, whereas here it is solely due to Coulomb interaction.

4.2.3 Magneto transport

At low magnetic fields the effect of finite magnetic flux density $\boldsymbol{B}$ can be included within the BTE picture by introducing a Lorentz force term $-e\boldsymbol{v}_{l\boldsymbol{k}} \times \boldsymbol{B}$ in the force $\boldsymbol{F}$ in Eqs. (4.4) and (4.6). In the case of isotropic bands the components of the resistivity tensor for a 2DEG are given by [65]

$$\rho_{xx} = \frac{m_\parallel}{e^2} \mathrm{Re} \left\{ \frac{1}{\mathrm{Tr}\widehat{N} \left(\widehat{K} - i\omega_c \widehat{1} \right)^{-1}} \right\}, \tag{4.12a}$$

$$\rho_{xy} = \frac{m_\parallel}{e^2} \mathrm{Im} \left\{ \frac{1}{\mathrm{Tr}\widehat{N} \left(\widehat{K} - i\omega_c \widehat{1} \right)^{-1}} \right\}, \tag{4.12b}$$

where the elements of matrix $\widehat{N}$ are $\{\widehat{N}\}_{ij} = \eta k_i k_j / 2\pi = \sqrt{n_i n_j}$ (η is the valley degeneracy) and $\omega_c = eB/m_\parallel$ is the cyclotron frequency. Here T is 0 K, $\boldsymbol{B} = B\boldsymbol{e}_z$, $\boldsymbol{E} = E\boldsymbol{e}_x$, and n_i (k_i) is the density (Fermi momentum) of sub-band i. In the case of single occupied 2D sub-band Eq. (4.12) reduces to the familiar form

$$\rho_{xx} = \sigma^{-1} = (en_e\mu)^{-1} \tag{4.13a}$$

$$\rho_{xy} = -B/en_e. \tag{4.13b}$$

The above equation for the Hall resistance ρ_{xy} results also by simply calculating the field which cancels Lorentz force $-e\boldsymbol{v}_D \times \boldsymbol{B}$. The Hall resistance depends only on B and n_e, which provides the standard method to determine the carrier density by measuring $\rho_{xy} = E_y/J_x$.[2] Generally we define that the Hall carrier density is defined through $n_H = -B/e\rho_{xy}$. It should be noted, however, that Eq. (4.13b) is only a special case where n_H just happens to be equal with the physical total density. For example, if two 2D sub-bands with different mobilities (μ_1 and μ_2) are occupied then Eq. (4.12b) gives in the limit $B \longrightarrow 0$ [65]

$$n_H = \frac{(\sigma_1 + \sigma_2)^2}{(\sigma_1 + \sigma_2)^2 + e^2 n_1 n_2 (\mu_1 - \mu_2)^2} n_e, \tag{4.14}$$

where $\sigma_i = e\mu_i n_i$ ($i = 1, 2$) are the separate conductivities of the sub-bands (total conductivity $\sigma = \sigma_1 + \sigma_2$). This equation gives $n_H = n_e = n_1 + n_2$ only if $\mu_2 = \mu_1$, which

[2] J_x is produced by E_x and E_y is measured while $J_y = 0$.

is seldom the case, or if the second sub-band has zero population. Note that we can obtain Eq. (4.14) also by considering two parallel channels which produce independently Hall fields $-J_xB/en_{1,2}$ and performing a standard circuit analysis to this system.

Figure 4.4 shows n_H measured as a function the gate voltages from Si well with $t_{\rm w} = 16.5$ nm. When $V_{\rm BG} \lesssim 0.4$ V or $V_{\rm TG} \lesssim 0.1$ V the Hall density is a linear function of the both gate voltages and the Hall density corresponds accurately to the physical electron density n_e. In the bias window $V_{\rm BG} \gtrsim 0.4$ V and $V_{\rm TG} \gtrsim 0.1$ V n_H behaves strongly non-monotonically and seems to be less than the physical total n_e. The behavior of n_H can be understood on the basis of Eq. (4.14): in the linear gate bias windows there is only single sub-band populated and in the non-monotonic bias window there are two sub-band populated with different mobilities. This interpretation is consistent with Sec. 4.2.2.

If the cyclotron frequency ω_c is larger than the relaxation rate τ^{-1} electrons can oscillate several periods on the cyclotron orbit without scattering and Landau level formation [with eigen energies $\hbar\omega_c(N+\frac{1}{2})$] starts to affect the transport. In the ideal case $\omega_c\tau \to \infty$

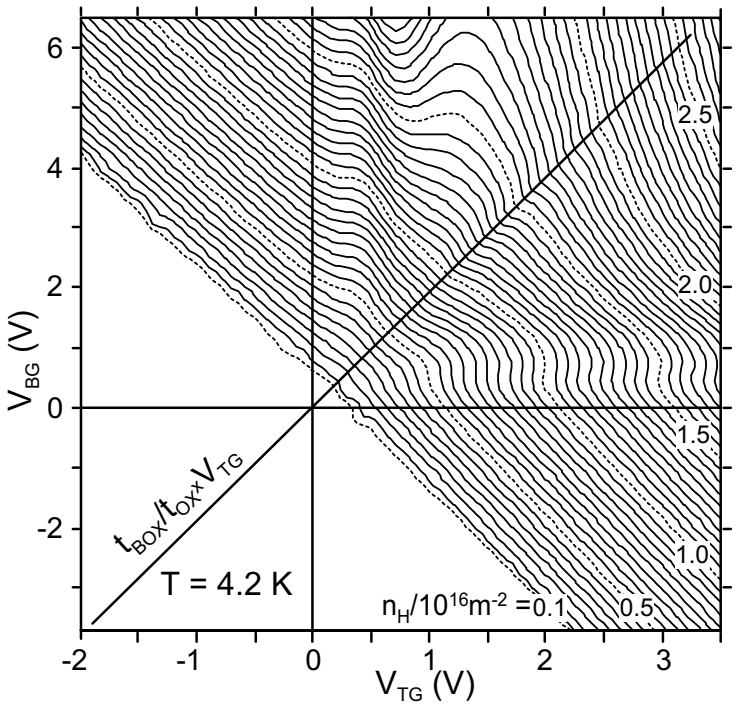

Figure 4.4: *Contour plot of Hall electron density measured as a function of the top gate voltage V_{TG} and the back gate voltage V_{BG} from device B-E721 with $t_w = 16.5$ nm. The contour spacing is $0.5\times10^{15}m^{-2}$ and the labels are for the dashed contours. After Paper III.*

(ignoring all broadening effects) the step-like 2D density of states changes into [71]

$$\nu(\mathcal{E}) = \frac{2\eta eB}{h} \sum_{N=0}^{\infty} \delta\left(\mathcal{E} - E_1 - \hbar\omega_c(N + \frac{1}{2})\right), \tag{4.15}$$

where E_1 is the threshold of the first 2D sub-band (η arises from valley degeneracy and factor 2 comes from spin degeneracy). In reality the Landau levels have finite width and the δ-function spikes are smeared. For example, if $\omega_c\tau$ is not too high $\nu(\mathcal{E})$ shows only small oscillations whose amplitude depends level broadening. These quantum oscillations are also seen in $\rho_{xx,xy}$ and they are referred as Shubnikov-de Haas (SdH) oscillations. [72] The period of the main component of the SdH oscillations is equal to the one in Eq. (4.15), which suggests oscillations with period $\hbar\omega_c$. As a result if we change the electron density n_e by Δn_e in such away that ρ_{xx} makes one full cycle then $\Delta n_e = e2\eta B/h$. If, on the other hand, we alter B instead of n_e then $\rho_{xx}(1/B)$ oscillates with period $2\eta e/hn_e$ due to factor $2\eta eB/h$ in $\nu(\mathcal{E})$. Furthermore, if there are several sub-systems present in the 2DEG, which have different densities n_i, they cause oscillating components to $\rho_{xx}(1/B)$ with periods $2\eta_i e/hn_i$ (see Ref. [73] for higher order effects). This feature is extremely useful as it enables determination of the carrier density of a 2DEG in the multi sub-band regime, where Hall method typically fails.

SdH oscillations measured from a Si well in single and two sub-band regime are shown in Fig. 4.5. If we look at the low field region we clearly observe only single oscillation in $\rho_{xx}(B)$ with monotonic increase in the oscillation amplitude in the upper curve. In the lower curve the amplitude varies as a function of B (see, e.g., the maximum close to $B = 1$ T), which suggest that there are more oscillating components present. By performing Fourier transform to $\rho_{xx}(1/B)$ (see the inset in Fig. 4.5), we indeed see that there are two components in the lower curve and only one in the upper curve. The peaks in the Fourier transform amplitude give the corresponding densities. The SdH densities presented in Figures 3.5 and 4.2 are simply positions of such peaks.

Above $B \sim 1.5$ T the magnetic field starts to generate significant energy difference between different spin orientations (Zeeman effect) which splits the maxima in $\rho_{xx}(B)$. [1] The last minima in the upper $\rho_{xx}(B)$ in Fig. 4.5 goes to zero. When $\omega_c\tau \gg 1$ $\nu(\mathcal{E})$ indeed shows the gaps suggested by Eq. (4.15) and if Fermi level $\mathcal{E}_F$ lies in such gap $\rho_{xx} = 0$ and ρ_{xy} is equal to quantized value $h/e^2\nu_f$, where ν_f is integer describing full Landau levels referred as Landau level (LL) filling factor. [74] This is the integer quantum Hall effect discovered in 1980. [75] Figure 4.6 shows the diagonal resistivity ρ_{xx} as a function of the voltages measured from two devices F-E73 ($t_{\mathrm{W}} =$ 7.0 nm) and F-E42 ($t_{\mathrm{W}} =$ 14 nm) at strongly quantizing field of $B = 9.0$ T.The bright and dark color correspond to low and high ρ_{xx}, respectively. In the white regions $\rho_{xx} \sim 0$ and Hall resistance ρ_{xy} is equal to quantum Hall value $h/e^2\nu_f$. Note that the positions of constant LL form continues trajectories (the ρ_{xx} minima) in the thinner device F-E73 [Fig. 4.6(a)], which is the

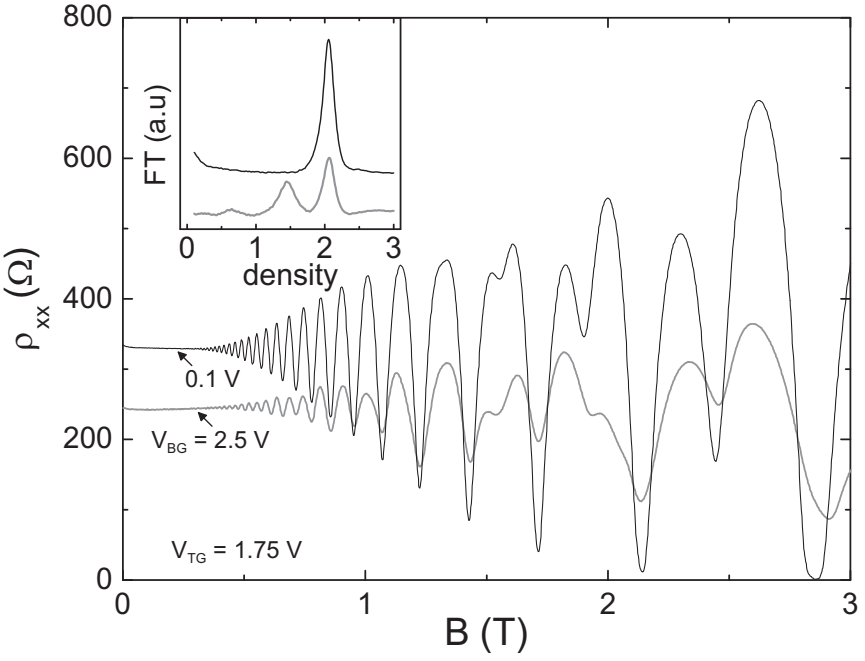

Figure 4.5: *Diagonal resistivity of device B-E711 (t_W = 17 nm) as a function of magnetic field at two gate biasing points at 290 mK. Inset: Fourier transform (FT) amplitude of $\rho_{xx}(1/B)$ as a function of the electron density (in units 10^{15} m^{15}). The FT frequency is converted to density (per degeneracy) by multiplying by e/h. Taking into account the spin and valley degeneracy the peaks in the FT give $n_1 \approx 8.2 \times 0^{15}$ m^{15} for the single sub-band curve ($V_{BG} = 0.1$ V). For the two sub-band curve ($V_{BG} = 2.5$ V) we find $n_1 \approx 8.3 \times 0^{15}$ m^{15} and $n_2 \approx 5.8 \times 0^{15}$ m^{15}.*

indication of single sub-band transport. These trajectories are constant carrier density contours.[3] The thick sample F-E42 [Fig.4.6(b)] behaves similarly in single sub-band bias regimes (when electron density is low or $V_{\rm BG} \lesssim 0.5$ V or $V_{\rm TG} \lesssim 0.25$ V). In the bias region where $V_{\rm BG} \gtrsim 0.5$ V, $V_{\rm TG} \gtrsim 0.25$ V and $\nu_f > 4$ the constant ν_f trajectories are broken into a 2D pattern in Fig. 4.6(b) , which is due to appearance of the second spatial sub-band. In single sub-band regimes the trajectories with $\nu_f = 4(k+1)$ (here $k = 0, 1, 2...$) are related to the cyclotron gaps $\hbar\omega_c$ of Eq. (4.15) (the factor 4 arises from two valleys and two spins). Large B splits the spin degeneracy (as already pointed above) and also the valley degeneracy, which introduces more oscillatory components in $\rho_{xx}(B)$ in the spirit of the two sub-band case discussed above. If valley and spin splittings are of the same magnitude as in bulk MOSFETs then $\nu_f = 2k + 3$ and $\nu_f = 4k + 2$ can be related to valley and spin gaps, respectively. [1] Finite valley splitting has been investigated and observed in bulk Si MOSFET devices also at low magnetic fields (and at high ν_f). [76] Furthermore, in high disorder (low mobility) SiO_2-Si-SiO_2 systems with thin Si layer ($\sim 8 - 10$ nm) valley splitting can depend strongly on the position of the electron gas

[3]The carrier density in Fig. 4.1(b) is determined on the basis of similar trajectories at $B = 2.5$ T.

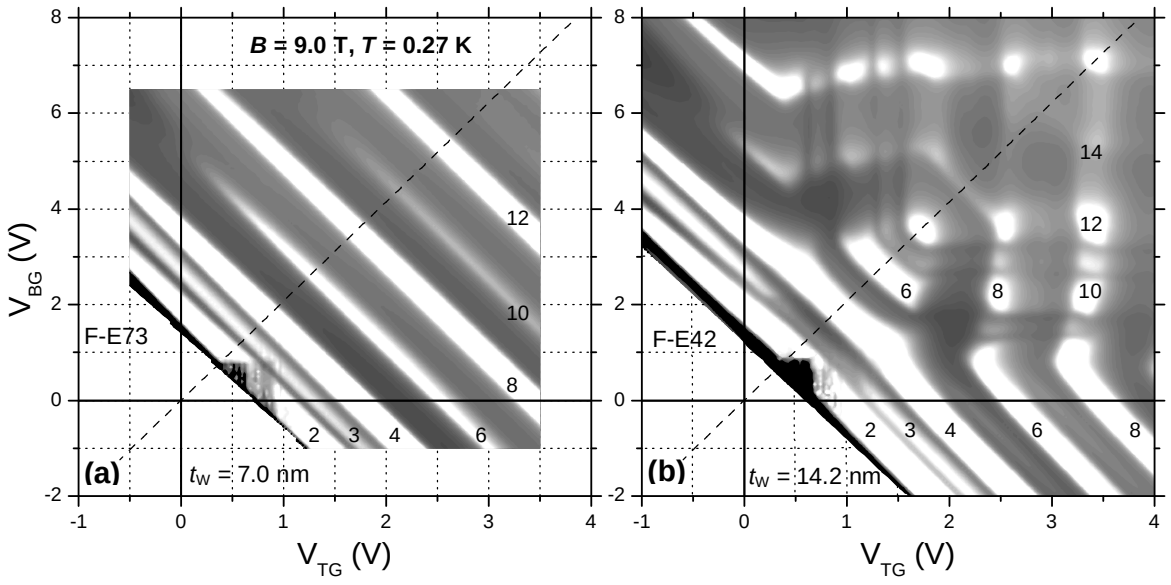

Figure 4.6: *Gray scale plot of diagonal resistivity ρ_{xx} of two double-gate devices at B = 9.0 T at 0.27 K. The dashed line is the symmetric gate bias line $V_{BG} = V_{TG} t_{BOX}/\ t_{OX}$. The gray scale is proportional to ρ_{xx}: dark and light color correspond to high and low resistance, respectively. The regions showing the grid are excluded in the measurements. The numbers inside the axis indicate the Landau level filling factors ν_f. Only few ν_f are indicated in (b) and missing values can be simply obtained by counting the minima. Note that conductivity of these devices is plotted in Fig. 4.3 and mobility of F-E42 (together with carrier density) is shown in Fig. 4.1(b).After Paper IV.*

inside the Si well [77, 78] and splitting has been observed even at zero field [79].

4.3 Room temperature transport

In addition of the elastic scattering mechanisms discussed above a significant electron-phonon momentum relaxation is present due to thermal phonon population at room temperature. At low carrier densities phonon scattering is the most effective mechanism limiting the mobility; at higher densities also surface roughness starts to limit the mobility. Typical approach to estimate the magnitude of the acoustic phonon limited mobility at elevated temperatures is to make the so-called quasi-elastic approximation $\hbar\omega_{\boldsymbol{q}} \ll k_B T, \mathcal{E}_{n\boldsymbol{k}}, \mathcal{E}_{n'\boldsymbol{k}'}$ in Eq. (3.15). [29, 33, 80] Under these assumptions the *e-ph* transition rate reduces to[4] $W^{\boldsymbol{q}}_{n\boldsymbol{k},n'\boldsymbol{k}'} = \frac{4\pi}{\hbar}\frac{k_B T}{\hbar\omega_{\boldsymbol{q}}} \left|\mathcal{M}^{+\boldsymbol{q}}_{n\boldsymbol{k},n'\boldsymbol{k}'}\right|^2 \delta(\mathcal{E}_{n\boldsymbol{k}} - \mathcal{E}_{n'\boldsymbol{k}'})$. Thus, $M_{nn'}(\boldsymbol{q})$

[4]Note that the total transition rate is $W^{\boldsymbol{q}}_{n\boldsymbol{k},n'\boldsymbol{k}'} = W^{+\boldsymbol{q}}_{n\boldsymbol{k},n'\boldsymbol{k}'} + W^{-\boldsymbol{q}}_{n\boldsymbol{k},n'\boldsymbol{k}'}$

entering Eq. (4.7) is given by [81]

$$|M_{nn'}(\boldsymbol{q})|^2 = \frac{\hbar}{2\pi}\sum_{\boldsymbol{q}}\frac{4\pi}{\hbar}\frac{k_BT}{\hbar\omega_{\boldsymbol{q}}}\left|\mathcal{M}^{+\boldsymbol{q}}_{n\boldsymbol{k},n'\boldsymbol{k}'}\right|^2 = \frac{k_BT}{(2\pi)^2\hbar\rho v_s^2}\Xi^2\widetilde{\mathcal{F}}_{n,n'} \quad (4.16a)$$

$$\widetilde{\mathcal{F}}_{n,n'} \equiv \int\frac{dq_z}{2\pi}\left|\mathcal{F}_{n,n'}\right|^2 = \int dz\,|\psi_n(z)|^2\,|\psi_{n'}(z)|^2\,. \quad (4.16b)$$

We have assumed standard linear dispersion relations $\omega_{\boldsymbol{q}} = v_s q$ and, for the sake of simplicity, an isotropic deformation potential constant $\{\widehat{\Xi}\widehat{S}\boldsymbol{e}_{\boldsymbol{q}}\}_{bb} = \Xi$.[5] Furthermore, we neglect screening which is a common approximation for room temperature *e-ph* scattering in 2DEG [29]. As $|M_{nn'}(\boldsymbol{q})|^2 \propto \widetilde{\mathcal{F}}_{n,n'}$ the *e-ph* scattering depends strongly on the electron confinement: the smaller is the width of the electron gas the larger is the phonon scattering rate (provided that $\psi_n(z)$ and $\psi_{n'}(z)$ have sufficient overlap). The situation is transparently illustrated in the case of single sub-band, whence the (acoustic) phonon limited mobility is $\mu_{ph} \propto \tau_l^{ph} \propto 1/\widetilde{\mathcal{F}}_{11}$. The dependency of the *e-ph* scattering on the confinement of the 2DEG can viewed as a consequence of Heisenberg uncertainty relation: the smaller space in the z-direction the 2DEG occupies the more uncertain is the z-direction momentum, which enables larger phase space of phonons to interact with the electrons.

At room temperature several 2D sub-bands from different valleys of Si conduction band are occupied even in devices with sub-10 nm Si well thickness. [63] This complicates the analysis of the mobility. However, still the electron density dependency of Coulomb and surface roughness scattering limited mobility (and its magnitude) is roughly the same as at low temperatures [29, 63]. Furthermore, these elastic scattering mechanisms are at minimum at symmetric bias $V_{\mathrm{BG}} = V_{\mathrm{TG}}t_{\mathrm{BOX}}/\,t_{\mathrm{OX}}$ [63, 82] as in the case of single sub-band transport at low temperatures (see Sec. 4.2.1). Thus, all scattering mechanisms at room temperature are at minimum at symmetric bias and mobility enhancement is expected. Note that the population in the valleys with heavier transport mass increases towards the symmetric bias, which reduces the mobility, but this is a minor effect. [63, 82]

Figure 4.7 shows experimental total electron density $n_e = \sum_l n_l$ and effective Drude mobility $\mu = \sigma/en_e$ contours of two double-gate devices with $t_{\mathrm{W}} = 6.8$ nm (F-E741) and $t_{\mathrm{W}} = 17.3$ nm (B-E742) as a function of top gate voltage V_{TG} and back gate voltage V_{BG} at 300 K. This data clearly shows the predicted enhancement of mobility towards $V_{\mathrm{BG}} = V_{\mathrm{TG}}t_{\mathrm{BOX}}/\,t_{\mathrm{OX}}$. Despite the large difference in t_{W} both devices behave qualitatively in same fashion. Note that due to thermal broadening the sub-band coupling effects, which were evident at low temperatures, can not be distinguished in Fig. 4.7.

[5] Eq. (4.16b) follows from Parseval's theorem. [25]

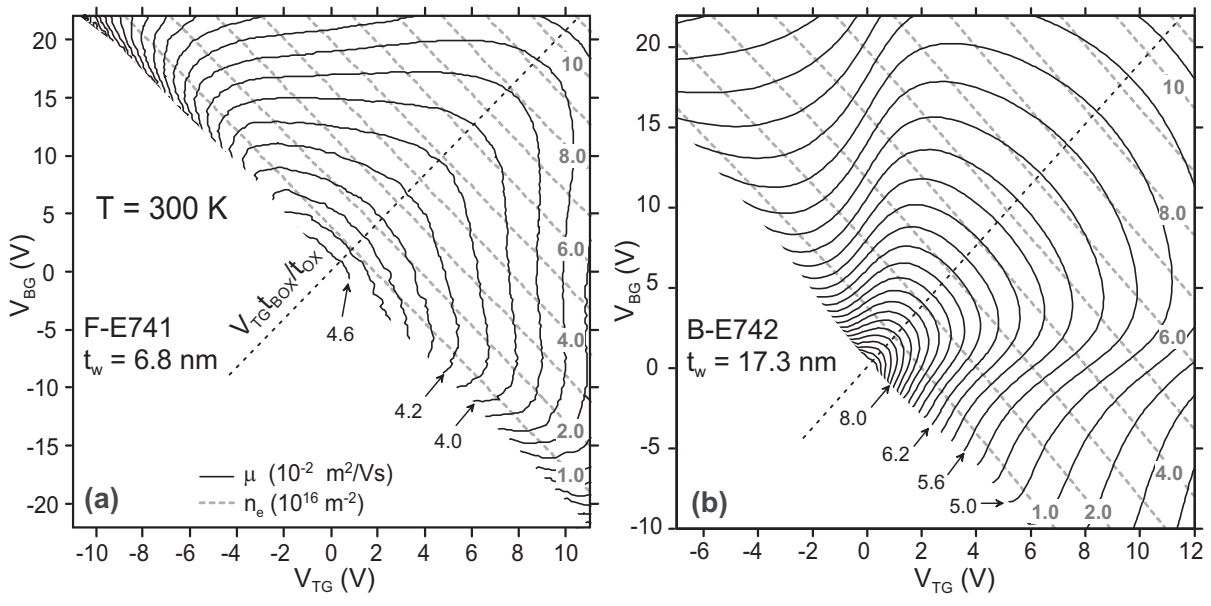

Figure 4.7: *Effective electron mobility μ (black thin curves) and electron density n_e (gray thick dashed curves with gray bold labels) measured as a function of the gate voltages V_{TG} and V_{BG} from (a) 6.8 nm thick and (b) 17.3 nm thick device at 300 K. n_e is determined by the split capacitance voltage method. The contour spacing for n_e is $1.0\times10^{16} m^{-2}$. For μ the spacing is 0.1 and 0.2×10^{-2} m^2/Vs in (a) and (b), respectively. The dashed line is the symmetric gate bias line $V_{BG} = V_{TG}t_{BOX}/\ t_{OX}$. After Papers II and IV.*

Chapter 5

Electron-phonon energy relaxation

In this part of the thesis we deal with electron-lattice energy loss in 3D and 2D semiconductor systems (Papers VI and VII). This topic has attained a great deal of interest during the last few decades. [9] One reason for the extensive studies of electron-phonon (*e-ph*) energy relaxation arises from device applications. For example, at high temperatures *e-ph* energy loss processes are directly linked to transistor performance. In low temperature bolometer and microcooler applications thermal *e-ph* coupling is the key parameter of interest. [18] Another driving force for the energy relaxation studies is that it is connected to the versatile physics of microscopic electron-phonon interaction. Here the main focus is on the low temperature effects and acoustic phonons.

The *e-ph* energy loss is highly sensitive to various parameters of the coupled *e-ph* system. The most important parameter is of course the nature of the electron-phonon interaction. In single-valley semiconductors the electron-phonon interaction can be typically described by deformation potential or piezoelectric coupling constants. [2] In quantum wells also other types of coupling due to heterointerface [83] or electric field [84] induced quantum confinement may be important. In the above-mentioned electron lattice coupling mechanisms the dependence of the *e-ph* matrix elements on the electronic variables, such as momentum, can be typically ignored. The situation is different, e.g., in metals where momentum dependency must be included due to the high Fermi level. [33, 85] However, by simply setting the *e-ph* matrix elements to a constant is not the whole story even for deformation potential coupling in semiconductors as discussed in Section 3.2.2. The fact that certain strain components lift the valley degeneracy lead to important role of the valley degree of freedom in elastic and ultrasonic properties of bulk many-valley semiconductors. [45, 86–88]

Interaction between electrons and phonons is strongly affected also by the disorder of the electron system and, therefore, the problem is commonly divided into two special cases: pure and impure (or diffusive) limit of *e-ph* interaction. The cross-over between

these two regions is defined as $q_T l_e = 1$, where $q_T = k_B T/\hbar v_s$ is the thermal phonon wave vector (T is the temperature of the lattice and v_s the sound velocity) and l_e is the carrier mean free path. Recent theory for single-valley semiconductors [12] predicts that the *e-ph* energy relaxation is strongly enhanced when the system enters from the pure limit ($q_T l_e > 1$) to the diffusive limit ($q_T l_e < 1$). The behavior is the opposite in comparison to metals where it is well known, since the pioneering work by A. B. Pippard [89], that the disorder of the electron system tends to suppress the *e-ph* energy relaxation (see also Ref. [90]). The disorder dependency of the *e-ph* energy loss also depends strongly on microscopic nature of the interaction, which explains the difference between isotropic semiconductors and metals. [12]

Here we discuss on *e-ph* energy relaxation in semiconductors on the basis of Papers VI and VII. We first introduce some general aspects of the problem and give heuristic derivation for the power loss. Then we sketch a more detailed theory and give microscopic many-band power loss formula for the case where phonons cannot directly couple different bands. We show some special cases of the formula and, finally, view the experimental data of Paper VI on n-type Si.

5.1 Carrier-lattice thermal resistance and energy relaxation time

We are interested in the total steady state *e-ph* energy flow rate (or power flow) between coupled carrier and lattice sub-systems. We assume that these sub-systems are in separate internal equilibrium, respectively. Within this so-called temperature model[10, 91] the total energy loss rate can be quite generally described by a symmetric power loss formula

$$P = F(T_e) - F(T_{ph}), \tag{5.1}$$

where T_e and T_{ph} are the electron and phonon temperatures, respectively (see Refs. [9–12, 92], Papers VI,VII and also next Sub-section). The energy loss rate (function) $F(T)$ can be easily linked to the *e-ph* energy relaxation time τ_{e-ph} by heuristic approach. This time scale is roughly equivalent to the thermal RC time constant defined by $R_{e-ph}C_e$, where $R_{e-ph}^{-1} = \delta F(T)/\delta T$ is the macroscopic electron-phonon thermal resistance and C_e is the electron heat capacity (see Fig. 5.1). At low temperatures $\tau_{e-ph}^{-1} \propto T_e^p$ and $C_e \propto T_e$[19], which leads us to well-known power law

$$F(T) \propto T^n, \tag{5.2}$$

where $n = p + 2$. This type of temperature dependency has been experimentally verified in various semiconductors [9, 93–98, VI] and also metals [99–101]. The prefactor and power n depend on the microscopic physics of the coupled *e-ph* system.

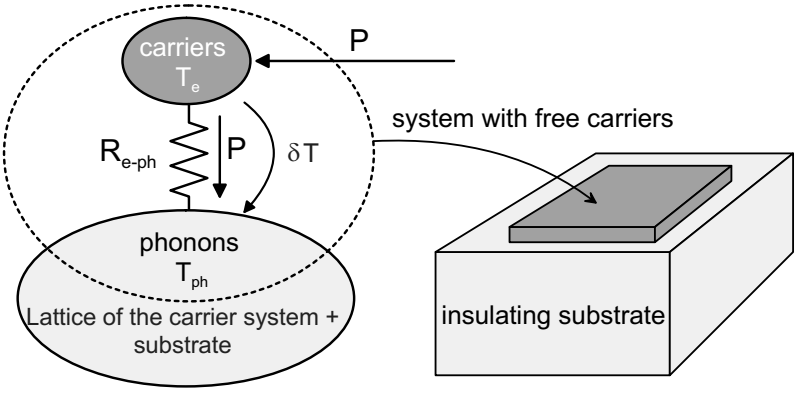

Figure 5.1: *Illustration of the power flow between coupled electron and phonon systems. R_{e-ph} is the e-ph thermal resistance. Power flow P induces a temperature difference $\delta T = R_{e-ph}P$.*

5.2 Microscopic power loss formula

When electron system emits a phonon with frequency $\omega = \omega_{\boldsymbol{q}}$ it looses energy $\hbar\omega$ to the phonon system. In the absorption electrons gain $\hbar\omega$ from the phonon system. The power absorption/emission is the occurrence rate of the event multiplied by this energy. Therefore, the total power loss is

$$P = \frac{1}{V_e}\sum_{\boldsymbol{q}} \hbar\omega_{\boldsymbol{q}} \left[W_{em}(\boldsymbol{q}) - W_{ab}(\boldsymbol{q})\right], \tag{5.3}$$

where $W_{em}(\boldsymbol{q})$ and $W_{ab}(\boldsymbol{q})$ are phonon emission and absorption rates. Equivalently P could be viewed as the energy average of the electron-phonon or phonon-electron collision integral. [102] In the former case the collision integral would be the one given by Eq. (4.5) with *e-ph* scattering rates of Eq. (3.15). The rates $W_{em,ab}(\boldsymbol{q})$ can be obtained from the golden rule formula Eq. (3.9) in the spirit of Refs. [10, 91] and Paper VII, whence we obtain

$$F(T) = \sum_{\boldsymbol{q}} \omega_{\boldsymbol{q}} N_T(\omega_{\boldsymbol{q}}) 2\boldsymbol{e}_{\boldsymbol{q}}^\dagger \widehat{M}_{\boldsymbol{q}}^\dagger \mathrm{Im}\left\{-\widehat{\chi}(\boldsymbol{q},\omega_{\boldsymbol{q}})\right\} \widehat{M}_{\boldsymbol{q}} \boldsymbol{e}_{\boldsymbol{q}} \tag{5.4}$$

with $P = F(T_e) - F(T_{ph})$ [Eq. (5.1)], where $\widehat{\chi}(\boldsymbol{q},\omega)$ is the density response function. This result relies on the long wavelength assumption where the phonons cannot couple different bands. In other words, we assume that the *e-ph* matrix elements satisfy $\mathcal{M}^{\boldsymbol{q}}_{l,l'} = \mathcal{M}^{\boldsymbol{q}}_{l,l'}\delta_{l,l'}$, when we need only the intra-band matrix elements $\mathcal{M}_{\boldsymbol{q},l} \equiv \mathcal{M}^{\boldsymbol{q}}_{l,l}$. We have introduced a matrix notation where the coupling matrix $\widehat{M}_{\boldsymbol{q}}$ is related to $\mathcal{M}_{\boldsymbol{q},l}$ through relation

$$\mathcal{M}_{\boldsymbol{q},l} = \sum_{i=x,y,z} \{\widehat{M}_{\boldsymbol{q}}\}_{l,i} e_i, \tag{5.5}$$

where e_i are components of the phonon polarization vector $\boldsymbol{e}_{\boldsymbol{q}}$ ($|\boldsymbol{e}_{\boldsymbol{q}}| = 1$). Note that if $\mathcal{M}_{\boldsymbol{q},l} = \mathcal{M}_{\boldsymbol{q},m}$ for all l, m or the number bands $L = 1$ then Eq. (5.4) reduces to power

loss formula of Refs. [10, 91].[1] In the case of deformation potential coupling to bulk acoustic phonons (in a volume V_{ph}) the coupling matrix is determined by Eqs. (3.19) and (3.21a) resulting

$$\widehat{M}_{\boldsymbol{q}} = i\sqrt{\frac{\hbar}{2V_{ph}\rho\omega}}q\widehat{\Xi}\widehat{S}, \tag{5.6}$$

where we have set the *e-ph* form-factors [Eq. (3.22)] to unity.

The response function $\widehat{\chi}(\boldsymbol{q},\omega)$ can be expressed using the mean field result $\widehat{\chi}(\boldsymbol{q},\omega) = \widehat{\chi}^0(\boldsymbol{q},\omega)\widehat{\varepsilon}^{-1}(\boldsymbol{q},\omega)$ in the spirit of Refs. [45, 47] (see also Sec. 3.2.3). If we further assume that $\widehat{\chi}^0(\boldsymbol{q},\omega)$ and $\widehat{\varepsilon}(\boldsymbol{q},\omega)$ are given by Eqs. (3.28) and (3.33), we can divide $F(T)$ [Eq. (5.4)] into symmetric (F_S) and asymmetric (F_A) terms:

$$F(T) = F_S(T) + F_A(T), \tag{5.7a}$$

$$F_i(T) = \sum_{\boldsymbol{q}} \omega_{\boldsymbol{q}} N_T(\omega_{\boldsymbol{q}}) 2\mathrm{Im}\left\{-\chi_i\right\} \frac{M_i^2}{\left|\varepsilon_i(\boldsymbol{q},\omega_{\boldsymbol{q}})\right|^2} \tag{5.7b}$$

$$M_i^2 = \boldsymbol{e}_{\boldsymbol{q}}^\dagger \widehat{M}_{\boldsymbol{q}}^\dagger \widehat{Q}_i \widehat{M}_{\boldsymbol{q}} \boldsymbol{e}_{\boldsymbol{q}} \tag{5.7c}$$

where $i = S, A$, $\chi_S = \chi^0(\boldsymbol{q},\omega)$ and $\chi_A = \chi_0^0(\boldsymbol{q},\omega) + \chi_1^0(\boldsymbol{q},\omega)$ [see Eq. (3.28)]. This equation introduces yet another notation: the effective matrix elements M_i^2, which are defined by quadratic forms and screened with the scalar dielectric functions $\varepsilon_i(\boldsymbol{q},\omega)$ of Eq. (3.33). The matrix elements compactly describe the contributions of symmetric (M_S^2) and asymmetric (M_A^2) *e-ph* coupling. Note that from the properties of $\widehat{Q}_i$ it follows that the effective matrix elements obey $M_i^2 \geq 0$ and, therefore, also $F_i(T) \geq 0$. If the *e-ph* interaction is mediated through deformation potential coupling [Eqs. (3.19), (3.21a) and (5.6)] then quadratic form $\Xi_{S,A}^2 = \boldsymbol{e}_{\boldsymbol{q}}^\dagger \widehat{S}^\dagger \widehat{\Xi}^\dagger \widehat{Q}_{S,A} \widehat{\Xi}\widehat{S}\boldsymbol{e}_{\boldsymbol{q}}$ can be interpreted as a square of the deformation potential "constant". The asymmetric part $F_A(T)$ arises from many-band nature and it can be non-zero even with diagonal $\widehat{\chi}^0(\boldsymbol{q},\omega)$, which follows from the inter-band Coulomb interaction as discussed in Sec. 3.2.3 and Paper VII.

5.3 Single and many-valley semiconductors

Table 5.1 shows asymptotic low temperature expressions of Eq. (5.7) deep below the Bloch-Grüneisen limit $q_T = 2k_F$ for different systems.[2] We have divided the results in Table 5.1 into four category: 3D pure, 2D pure, 3D diffusive and 2D diffusive. These are described with a common $F_S(T)$, respectively. In the pure limit $q_T l_e \gg 1$ the formulas

[1] Sometimes the single-band version of Eq. (5.4) is referred as Kogan's formula after the Author of Ref. [10].

[2] The dielectric function $\varepsilon_A(\boldsymbol{q},\omega)$ is set to unity. Therefore, the results of Table 5.1 apply for single and many-valley semiconductors, with full spatial overlap of the electronic states for the latter. Furthermore, linear dispersion relations $\omega_{\boldsymbol{q}} = v_s q$ are assumed.

Table 5.1: *Symmetric $F_S(T)$ and asymmetric $F_A(T)$ contributions of energy loss rate of Eqs. (5.7). The pure and diffusive regimes are defined by $q_T l_e \gg 1$ and $q_T l_e \ll 1$, respectively. The Limits column gives additional assumptions used in calculating F_A. Temperature dependency arises from thermal phonon wave vector $q_T = \frac{k_B T}{\hbar v_s}$. The length scale $l_s = l_e v_F / v_s d$ and the effective deformation potential constant $\Xi_i^2 = \boldsymbol{e}_{\boldsymbol{q}}^\dagger \widehat{S}^\dagger \widehat{\Xi}^\dagger \widehat{Q}_i \widehat{\Xi} \widehat{S} \boldsymbol{e}_{\boldsymbol{q}}$. The bracket $\langle \cdots \rangle$ stands for an average over a solid angle and θ is the angle between $\boldsymbol{q}$ and the normal of the 2D electrons. The F_A with $\ln(q_T)$ factors are derived using isotropic $\Xi_A^2 = \Xi_0^2$. Both $F_{S,A}(T) \propto q_T^n$ are normalized with $\frac{\hbar \nu v_s}{2\pi^2 \rho v_F} B_{n-1}$, where $B_{n-1} = \Gamma(n)\zeta(n) = \int dx x^{n-1} / [\exp(x) - 1]$. After Paper VII.*

Category	$F_S(T)$	$F_A(T)$	F_A/F_S	Limits
3D pure	$\frac{\pi}{2\kappa^4} \langle \Xi_S^2 \rangle q_T^9$	$\frac{\pi}{2} \langle \Xi_A^2 \rangle q_T^5$	$\left(\frac{\kappa}{q_T}\right)^4$	–
3D diffusive	$\frac{3}{l_e \kappa^4} \langle \Xi_S^2 \rangle q_T^8$	$\frac{3}{l_e} \langle \Xi_A^2 \rangle q_T^4$	$\left(\frac{\kappa}{q_T}\right)^4$	$\sqrt{\frac{\gamma}{\overline{\gamma}}} q_T l_e, q_T l_s \gg 1$
		$\frac{v_F}{v_S} l_s \langle \Xi_A^2 \rangle q_T^6$	$\left(\frac{\kappa^2 l_s}{q_T}\right)^2$	$\sqrt{\frac{\gamma}{\overline{\gamma}}} q_T l_e, (q_T l_s)^{-1} \gg 1$
		$\frac{v_F}{\overline{\gamma}} \langle \Xi_A^2 \rangle q_T^6$	$\frac{\gamma}{\overline{\gamma}} \left(\frac{\kappa^2 l_e}{q_T}\right)^2$	$\sqrt{\frac{\gamma}{\overline{\gamma}}} q_T l_e, k_B T / \hbar \overline{\gamma} \ll 1$
2D pure	$\frac{1}{\kappa^2} \langle \sin\theta \Xi_S^2 \rangle q_T^7$	$\left\langle \frac{\Xi_A^2}{\sin\theta} \right\rangle q_T^5$	$\left(\frac{\kappa}{q_T}\right)^2$	–
2D diffusive	$\frac{2}{l_e \kappa^2} \left\langle \frac{\sin^2\theta \Xi_S^2}{(l_s\kappa)^{-2} + \sin^2\theta} \right\rangle q_T^6$	$\frac{1}{l_e} \Xi_0^2 q_T^4 \ln(q_T l_s)$	$\left(\frac{\kappa}{q_T}\right)^2$	$\sqrt{\frac{\gamma}{\overline{\gamma}}} q_T l, q_T l_s \gg 1$
		$\frac{v_F}{v_S} l_s \langle \sin^2\theta \Xi_A^2 \rangle q_T^6$	$(\kappa l_s)^2$	$\sqrt{\frac{\gamma}{\overline{\gamma}}} q_T l, (q_T l_s)^{-1} \gg 1$
		$\frac{v_F}{\overline{\gamma}} \langle \Xi_A^2 \rangle q_T^6$	$\frac{\gamma}{\overline{\gamma}} (\kappa l_e)^2$	$\sqrt{\frac{\gamma}{\overline{\gamma}}} q_T l, k_B T / \hbar \overline{\gamma} \ll 1$

for $F_{S,A}(T)$ are obtained by utilizing Eq. (3.29). In the diffusive limit $q_T l_e \ll 1$ they are obtained by utilizing Eqs. (3.32). The sound velocity v_s refers to both transversal and longitudinal modes of the crystal and, therefore, all expressions must be summed over these modes (if coupling to both type of modes exists). The dimensionality affects the Coulomb interaction (as described in Sec. 3.2.3) and as a result the screening wave vector $\kappa = 2\left[e^2 L\nu/4\varepsilon_b\right]^{1/(d-1)}$. Note that $F_S(T)$ is calculated assuming strong screening, but in many cases $F_A(T)$ is simply the weak/zero screening limit of $F_S(T)$. The symmetric component $F_S(T)$ is equivalent to the conventional single-band energy loss rate in the literature. Indeed, if we assume coupling only to longitudinal phonons all symmetric energy loss rates $F_S(T)$ agree with the expressions given in Refs. [9–12]. Note that the importance of the dynamical effects in the diffusive $\chi^0(\boldsymbol{q},\omega)$ are determined by the threshold $\omega/D_0 q^2 = 1$ or equivalently by $q_T l_s = 1$, which introduces the length scale $l_s = l_e v_F/v_s d$.

Let us next inspect the asymmetric part of $F(T)$, which is the novel result. First notice that in pure cases the ratio $F_A/F_S = (\kappa/q_T)^m$ where $m = 4(2)$ in 3D (2D). Thus, if screening is strong $F_A \gg F_S$, as we would intuitively expect. In the diffusive limit there are two competing internal relaxation mechanisms in the electron system, elastic inter-valley scattering and diffusion. When diffusion dominates over inter-valley scattering $\sqrt{\gamma/\overline{\gamma}} q_T l_e \gg 1$ and in the opposite situation $\sqrt{\gamma/\overline{\gamma}} q_T l_e \ll 1$. Note that despite the finite mean free path and inter-valley scattering rate $F_A \gg F_S$ still holds in Table 5.1. Furthermore, actually all F_A depend only very weakly on dimensionality, and when inter-band scattering dominates ($\sqrt{\gamma/\overline{\gamma}} q_T l_e, k_B T/\hbar\overline{\gamma} \ll 1$) the 3D and 2D rates are similar with $F_A(T) \propto \frac{v_F}{\overline{\gamma}} \langle \Xi_A^2 \rangle q_T^6 \propto T^6$. This type of temperature dependency is experimentally demonstrated in Fig. 5.2, which shows power density P as a function of the electronic temperature response T_e in n^+ Si. By assigning $F(T) = F_A(T)$ in Eq. (5.1), using the typical free electron values for the density of states (see Sec. 3.1.1), and acoustic properties of bulk Si we can estimate the intervalley relaxation rate $\overline{\gamma}$. This rate is related to the time τ_2, which is the scattering time between the different classes of Si valleys (see Fig. 3.1), according to $\tau_2^{-1} = \tau_{iv}^{-1}/6 = \overline{\gamma}/3$. For carrier densities $n_e = 3.5 - 16.0 \times 10^{25}$ m^{-3} we find that $\tau_2 \approx 0.2 - 0.35$ ps . These values fit well to the τ_2 values obtained from ultrasonic attenuation data of Ref. [88]. Further details can found from Papers VI and VII.

Finally, we want to point out that Eq. (5.7) and the results of Table 5.1 qualitatively describe also closely spaced electron-electron/hole bi-layers with different deformation potential coupling constants.[3] One such system is the 2DEG bi-layer realized in a double AlAs quantum well [103, 104], where the two electron gases are from conduction

[3]In this case we assume that $(V_{11} - V_{12}) \approx 0$ $[\varepsilon_A(\boldsymbol{q},\omega) \approx 1]$ and $\widehat{\chi}_0(\boldsymbol{q},\omega)$ is diagonal, whence $\mathrm{Im}\chi_{S,A} \simeq \mathrm{Im}\left\{Tr[\widehat{\chi}_0(\boldsymbol{q},\omega)]\right\}$.

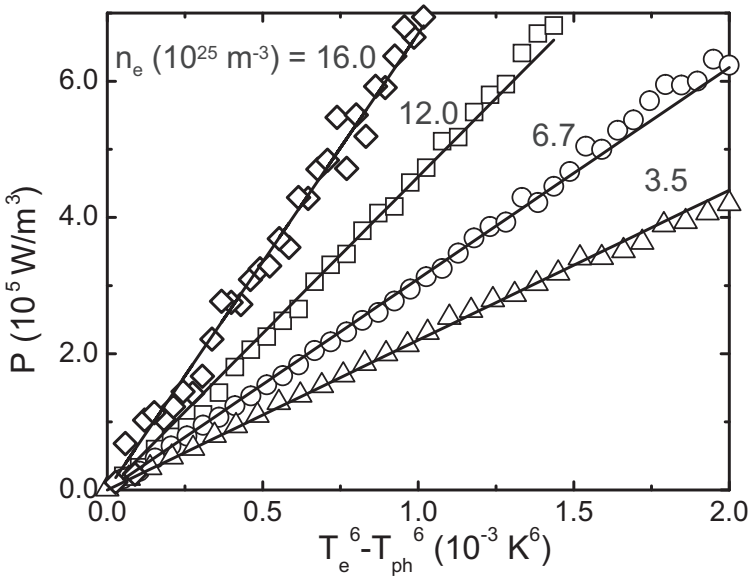

Figure 5.2: *The heating power density P vs. $T_e^6 - T_{ph}^6$ for n^+ Si samples with different carrier concentrations at bath temperature of 265 mK. The experiments were performed adopting the power flow scheme depicted in Fig. 5.1. After paper VI.*

band valleys with different symmetry. Such a 2DEG bi-layer systems can also be tuned between two component and single-component systems by external gate(s) in the spirit of the devices discussed in Chapter 4. Provided that screening is strong and the sub-systems (or layers) have different deformation potential coupling constants, the external gate can strongly tune the thermal *e-ph* resistance. This kind of system is a heat switch. If we, e.g., assume clean 2D system the switching ratio according to Table 5.1 is $\sim (\kappa/q_T)^2 \gg 1$. This line of thought suggests that actually any charge carrier system, which can be adjusted between single and multi-component "phase" by some external parameter, works as such a switch. The carrier coupling to environment (lattice) can be tuned provided that (*i*) screening is strong (*ii*) there exists a strongly asymmetric *e-ph* coupling in the multi-component "phase".

Chapter 6

Summary

Electronic properties of semiconductor based systems and devices depend on the host lattice of the semiconductor and quantum confinement. We can loosely say that the atomic lattice gives rise to energy bands and the confinement leads to spatial quantization of the electronic motion and spatial sub-bands. In this Overview the bands of interest were the conduction band valleys of many-valley semiconductors and spatial sub-bands of two-dimensional-electron gas in a quantum well. Different aspects of band degree of freedom were explored in 2D electron transport and electron-phonon energy relaxation in 2D and 3D electron gases.

In the studies of 2D electronic transport the experiments were focused on the single-gate (Paper I) and double-gate (Papers II–V) SiO_2-Si-SiO_2 quantum well field-effect-transistors (FETs), which links this Thesis also closely to silicon-on-insulator (SOI) technology. The Si quantum well thicknesses in this Thesis were in the range $\sim$ 5–60 nm. The device fabrication utilized wafer bonding, which provided thermal SiO_2 layers and resulted in excellent electronic properties. For example, the maximum low temperature mobility of the SOI FETs fabricated in this Thesis is comparable to the values measured from high-mobility bulk Si inversion layers. SOI-based FETs and, especially, the double-gate devices are intensively explored at the moment due to their prospects in microelectronics. On the other hand, from the viewpoint of 2D physics, the SiO_2-Si-SiO_2 structure provides a quantum well system with strong electronic (and optical) confinement, many-valley conduction band and indirect energy gap. However, most importantly, the inclusion of the back gate electrode enables the adjustment of the electron wave functions and the occupancy of the spatial 2D sub-bands inside the Si quantum well. The contrast between single and two-sub-band transport was studied at low temperatures. Population of the second spatial sub-band can be recognized in conductivity/mobility [V], Hall effect [III] and high-field magneto transport [III, IV]. For example, the conductivity shows a significant drop at the threshold of the second spatial sub-band, which is due to inter-sub-band coupling. Furthermore, the high break-down field of thermal

SiO_2 enable 2D carrier density control in a broad range and at high carrier densities Coulomb interaction drives the effective potential inside the Si well towards that of a bi-layer quantum well. When the effective potential is made symmetric (by adjusting the double-gate bias) the sub-band wave functions delocalize across the Si well and we observed a local minimum in the conductivity of a 14 nm-thick Si well. [V] This behavior resembles the resistance resonance effect observed in III-V bi-layer quantum wells. At room temperature several sub-bands are inevitably populated and the most relevant observed effect was the mobility enhancement towards symmetric quantum well potential. [II, IV] This mobility enhancement, sometimes referred as the volume inversion effect, is due to double-gate field adjustment of electron wave functions. It follows mainly from minimization of surface roughness matrix elements and phonon form factors. The enhancement is one of the benefits of double-gate FETs in comparison to similar single-gate FETs.

In the studies of electron energy relaxation we explored the situation where 2D/3D electron gas cools itself by radiating long wavelength acoustic phonons. (Papers VI and VII) We especially considered the case where the phonons do not directly couple the bands of the electron system. Now if the microscopic electron-phonon interaction is the same for different bands the band degree of freedom is irrelevant. However, in many systems the situation is the opposite: the interaction depends on the band index, which leads to interesting results. We developed a mean field theory for this type of electron-phonon (*e-ph*) energy loss rate. [VI, VII] The theory allows elastic inter and intra-band scattering and Coulomb interaction. Our model reproduced the long wavelength single-band *e-ph* energy loss rate results found in the literature. In the multi-band regime we found a set of new results. In this regime there exists a strong enhancement of the energy loss rate if phonons couple asymmetrically to different bands and the single-band interaction is strongly screened. The latter condition is fulfilled provided that the thermal phonon wavelength exceeds the screening length of the electron system. A canonical example of such many-band *e-ph* energy loss occurs when conduction band electrons in a many-valley semiconductor radiate long wavelength acoustic phonons. The effect was experimentally explored in heavily doped n-type Si samples at low temperatures. [VI] In the experiments the electron gas was heated above lattice temperature by electrical current while the electron temperature was measured with tunnel junction thermometry. The experimental temperature response of the electrons agreed with the theoretical predictions. Finally, we pointed out that our findings enable a design of a novel electron-phonon heat switch.

Bibliography

[1] T. Ando, A. B. Fowler, and F. Stern, "Electronic properties of two-dimensional electron systems," *Rev. Mod. Phys.*, vol. 54, pp. 337–432, 1982.

[2] J. Singh, *Physics of Semiconductors and Their Heterostructures*. New York: McGraw-Hill, 1993.

[3] J.-P. Colinge, *Silicon-on-insulator technology: Materials to VLSI*. Kluver, Boston, 2nd ed., 1997.

[4] G. K. Celler and S. Cristoloveanu, "Frontiers of silicon-on-insulator," *J. Appl. Phys.*, vol. 93, pp. 4955–4978, 2003.

[5] H.-S. P. Wong, "Beyond the conventional transistor," *IBM J. Res. & Dev.*, vol. 46, pp. 133–168, 2002.

[6] A. Palevski, F. Beltram, F. Capasso, L. Pfeiffer, and K. W. West, "Resistance resonance in coupled potential wells," *Phys. Rev. Lett.*, vol. 65, pp. 1929–1932, 1990.

[7] Y. Ohno, M. Tsuchiya, and H. Sakaki, "Gigantic negative transconductance and mobility modulation in a double-quantum-well structure via gate-controlled resonant coupling," *Appl. Phys. Lett.*, vol. 62, pp. 1952–1954, 1993.

[8] Y. Berk, A. Kamenev, A. Palevski, L. N. Pfeiffer, and K. W. West, "Resonant transport in coupled quantum wells: A probe for scattering mechanisms," *Phys. Rev. B.*, vol. 50, pp. 15420–15423, 1994.

[9] B. K. Ridley, "Hot electrons in low-dimensional structures," *Rep. Prog. Phys.*, vol. 54, pp. 169–256, 1991.

[10] S. M. Kogan, "On the theory of hot electrons in semiconductors," *Fiz. Tverd. Tela*, vol. 9, pp. 2474–2484, 1962. [Sov. Phys.–Solid State **4**,1813–1819 (1963)].

[11] P. J. Price, "Hot electrons in a GaAs heterolayer at low temperature," *J. Appl. Phys.*, vol. 53, pp. 6863–6866, 1982.

[12] A. Sergeev, M. Y. Reizer, and V. Mitin, "Deformation electron-phonon coupling in disordered semiconductors and nanostructures," *Phys. Rev. Lett.*, vol. 94, pp. 136602–1–4, 2005.

[13] J. W. Mayer and S. S. Lau, *Electronic Materials Science: For integrated circuits in Si and GaAs*. New York: Macmillan, 1990.

[14] M. Madou, *Fundamentals of Microfabrication*. New York: CRC press LLC, 2 ed., 2002.

[15] M. Bruel, B. Aspar, and A. J. Auberton-Herve, "The history, physics, and applications of the Smart-Cut process," *Jpn. J. Appl. Phys.*, vol. 36, pp. 1636–1642, 1997.

[16] C. G. Sodini, T. W. Ekstedt, and J. L. Moll, "Charge accumulation and mobility in thin dielectric MOS transistors," *Solid-State Electronics*, vol. 25, pp. 833–841, 1982.

[17] F. Pobell, *Matter and Methods at Low Temperatures*. Springer-Verlag, 1996.

[18] F. Giazotto, T. T. Heikkilä, A. Luukanen, A. M. Savin, and J. P. Pekola, "Opportunities for mesoscopics in thermometry and refrigeration: Physics and applications," *Rev. Mod. Phys.*, vol. 78, p. 217, 2006.

[19] N. W. Ascroft and N. D. Mermin, *Solid State Physics*. New York: Saunders, 1976.

[20] J. R. Chelikowsky and M. L. Cohen, "Nonlocal pseudopotential calculations for the electronic structure of eleven diamond and zinc-blende semiconductors," *Phys. Rev. B*, vol. 14, pp. 556–582, 1976.

[21] O. Madelung, ed., *Semiconductors, Group IV Elements and III-V Compounds*. Heidelberg: Springer-Verlag, 1991.

[22] L. J. Sham and M. Nakayama, "Effective-mass approximation in the presence of an interface," *Phys. Rev. B*, vol. 20, pp. 734–747, 1979.

[23] M. A. Green, "Intrinsic concentration, effective densities of states, and effective mass in silicon," *J. Appl. Phys.*, vol. 67, no. 6, pp. 2944–2954, 1990.

[24] M. Plischke and B. Bergersen, *Equilibrium Statistical Physics*. Singapore: World Scientific, 2 ed., 1994.

[25] G. Arfken, *Mathematical Methods for Physicists*. New York: Academic Press, 1970.

[26] S.M. Sze, *Physics of Semiconductor Devices*. New York: John Wiley & Sons, 1981.

[27] M. N. Alexander and D. F. Holcomb, "Semiconductor-to-Metal Transition in n-Type Group IV Semiconductors," *Rev. Mod. Phys.*, vol. 40, pp. 815–829, 1968.

[28] F. Stern and W. E. Howard, "Properties of semiconductor surface inversion layers in the electric quantum limit," *Phys. Rev.*, vol. 163, pp. 816–835, 1967.

[29] M. V. Fischetti and S. E. Laux, "Monte Carlo study of electron transport in silicon inversion layers," *Phys. Rev. B*, vol. 48, pp. 2244–2274, 1993.

[30] G. Bastard, *Wave mechanics applied to semiconductor heterostructures*. Paris: EDP Sciences, 1992.

[31] A. Rahman, M. S. Lundstrom, and A. W. Ghosh, "Generalized effective-mass approach for n-type metal-oxide-semiconductor field-effect transistors on arbitrarily oriented wafers," *J. Appl. Phys.*, vol. 97, p. 053702, 2005.

[32] F. Mandl, *Quantum Mechanics*. Chichester Wiley, 1992.

[33] V. F. Gantmakher and Y. B. Levinson, *Carrier Scattering in Metals and Semiconductors*. Amsterdam: North-Holland Physics Publishing, 1987.

[34] D. K. Ferry and S. M. Goodnick, *Transport in Nanostructures*. Cambridge University Press, 1997.

[35] F. Gamiz, F. Jimenez-Molinos, J. B. Roldan, and P. Cartujo-Cassinello, "Coulomb scattering model for ultrathin silicon-on-insulator inversion layers," *Appl. Phys. Lett.*, vol. 80, pp. 3835–3837, 2002.

[36] T. Ando, "Screening effect and quantum transport in a silicon inversion layer in strong magnetic fields," *J. Phys. Soc. Jpn*, vol. 43, pp. 1616–1626, 1977.

[37] R. E. Prange and T.-W. Nee, "Quantum spectroscopy of the low-field oscillations in the surface impedance," *Phys. Rev.*, vol. 168, pp. 779–786, 1968.

[38] D. Esseni, "On the modeling of surface roughness limited mobility in SOI MOSFETs and its correlation to the transistor effective field," *IEEE Transactions on Electron Devices*, vol. 51, pp. 394–401, 2002.

[39] S. M. Goodnick, D. K. Ferry, C. W. Wilmsen, Z. Liliental, D. Fathy, and O. L. Krivanek, "Surface roughness at the Si(100)-SiO_2 interface," *Phys. Rev. B*, vol. 32, pp. 8171–8186, 1985.

[40] G. H. Kruithof, T. M. Klapwijk, and S. Bakker, "Temperature and interface-roughness dependence of the electron mobility in high-mobility Si(100) inversion layers below 4.2 K," *Phys. Rev. B*, vol. 43, pp. 6642–6649, 1991.

[41] C. Herring and E. Vogt, "Transport and deformation-potential theory for many-valley semiconductors with anisotropic scattering," *Phys. Rev.*, vol. 101, pp. 944–961, 1956.

[42] D. Pines and P. Nozieres, *The Theory of Quantum Liquids*, vol. I. New York: W. A. Benjamin, 1966.

[43] G. Mahan, *Many-Particle Physics*. New York: Plenum Press, 1981.

[44] S.-C. Lee and I. Galbraith, "Intersubband and intrasubband electronic scattering rates in semiconductor quantum wells," *Phys. Rev. B*, vol. 59, pp. 15796–15805, 1999.

[45] T. Sota and K. Suzuki, "Phonon attenuation in heavily doped many-valley semiconductors," *J. Phys. C: Solid State Phys.*, vol. 15, pp. 6991–7002, 1982.

[46] T. Sota and K. Suzuki, "Acoustic properties of heavily doped many-valley semiconductors in the weak localization regime," *Phys. Rev. B*, vol. 33, pp. 8458–8467, 1986.

[47] L. Swierkowski, J. Szymanski, and Z. W. Gortel, "Linear-response theory for multicomponent fermion systems and its application to transresistance in two-layer semiconductor structures," *Phys. Rev. B*, vol. 55, pp. 2280–2292, 1997.

[48] J. Lindhard, "On the properties of a gas of charged particles," *Kgl. Danske Videnskab. Selskab Mat.-Fys. Medd.*, vol. 28, pp. 1–57, 1954.

[49] F. Stern, "Polarizability of a two-dimensional electron gas," *Phys. Rev. Lett.*, vol. 18, pp. 546–548, 1967.

[50] J. K. Jain and S. Das Sarma, "Elementary electronic excitations in a quasi-two-dimensional electron gas," *Phys. Rev. B*, vol. 36, pp. 5949–5952, 1987.

[51] R. Fletcher, E. Zaremba, M. D'Iorio, C. T. Foxon, and J. J. Harris, "Persistent photoconductivity and two-band effects in GaAs/$Al_xGa_{1-x}As$ heterojunctions," *Phys. Rev. B*, vol. 41, no. 15, pp. 10649–10666, 1990.

[52] S. Das Sarma, "Theory of finite-temperature screening in a disordered two-dimensional electron gas," *Phys. Rev. B.*, vol. 33, pp. 5401–5405, 1986.

[53] P. F. Maldague, "Many-body corrections to the polarizability of the two-dimensional electron gas," *Surface Science*, vol. 73, pp. 296–302, 1978.

[54] A. L. Fetter, "Electrodynamics and thermodynamics of a classical electron surface layer," *Phys. Rev. B*, vol. 10, pp. 3739–3745, 1974.

[55] R. Zimmermann, *Many-Particle Theory of Highly Excited Semiconductors*. Leipzig: Teubner Verlagsgesellschaft, 1988.

[56] N. D. Mermin, "Lindhard dielectric function in the relaxation-time approximation," *Phys. Rev. B*, vol. 1, pp. 2362–2363, 1970.

[57] R. Kragler and H. Thomas, "Dielectric function in the relaxation-time approximation generalized to electron multiple-band systems," *Z. Phys. B*, vol. 39, pp. 99–107, 1980.

[58] A. G. Rojo, "Electron-drag effects in coupled electron systems," *J. Phys. Condens. Matter*, vol. 11, no. 5, pp. R31–R52, 1999.

[59] S. Das Sarma and A. Madhukar, "Collective modes of spatially separated, two-component, two-dimensional plasma in solids," *Phys. Rev. B*, vol. 23, pp. 805–815, 1981.

[60] G. E. Santoro and G. F. Giuliani, "Acoustic plasmons in a conducting double layer," *Phys. Rev. B*, vol. 37, pp. 937–940, 1988.

[61] L. Pfeiffer, K. W. West, H. L. Stormer, and K. W. Baldwin, "Electron mobilities exceeding 10^7 cm^2/v s in modulation-doped GaAs," *Appl. Phys. Lett.*, vol. 55, pp. 1888–1890, 1989.

[62] S. V. Kravchenko, G. V. Kravchenko, J. E. Furneaux, V. M. Pudalov, and M. D'Iorio, "Possible metal-insulator transition at B=0 in two dimensions," *Phys. Rev. B*, vol. 50, pp. 8039–8042, 1994.

[63] F. Gamiz and M. V. Fischetti, "Monte Carlo simulation of double-gate silicon-on-insulator inversion layers: The role of the volume inversion," *J. Appl. Phys.*, vol. 89, pp. 5478–5487, 2001.

[64] E. D. Siggia and P. C. Kwok, "Properties of electrons in semiconductor inversion layers with many occupied electric subbands. I. screening and impurity scattering," *Phys. Rev. B*, vol. 2, pp. 1024–1036, 1970.

[65] E. Zaremba, "Transverse magneto resistance in quantum wells with multiple subband occupancy," *Phys. Rev. B*, vol. 45, pp. 14143–14149, 1992.

[66] A. Y. Kuntsevich, N. N. Klimov, S. A. Tarasenko, N. S. Averkiev, V. M. Pudalov, H. Kojima, and M. E. Gershenson, "Intervalley scattering and weak localization in Si-based two-dimensional structures," *Phys. Rev. B*, vol. 75, p. 195330, 2007.

[67] H. L. Stormer, A. C. Gossard, and W. Wiegmann, "Observation of intersubband scattering in a 2-dimensional electron system," *Solid State Communications*, vol. 41, pp. 707–709, 1982.

[68] A. B. Fowler, "Substrate bias effects on electron mobility in silicon inversion layers at low temperatures," *Phys. Rev. Lett.*, vol. 34, pp. 15–17, 1975.

[69] D. Popovic, A. B. Fowler, and S. Washburn, "Metal-insulator transition in two dimensions: Effects of disorder and magnetic field," *Phys. Rev. Lett.*, vol. 793, pp. 1543–1546, 1997.

[70] X. G. Feng, D. Popovic, and S. Washburn, "Effect of local magnetic moments on the metallic behavior in two dimensions," *Phys. Rev. Lett.*, vol. 83, pp. 368–371, 1999.

[71] S. Datta, *Electronic Transport in Mesoscopic Systems*. Cambridge: Cambridge University Press, 1995.

[72] A. Isihara and L. Smrcka, "Density and magnetic field dependences of the conductivity of two-dimensional electron systems," *Journal of Physics C: Solid State Physics*, vol. 19, pp. 6777–6789, 1986.

[73] M. E. Raikh and T. V. Shahbazyan, "Magnetointersubband oscillations of conductivity in a two-dimensional electronic system," *Phys. Rev. B*, vol. 49, pp. 5531–5540, 1994.

[74] M. Janssen, O. Viehweger, U. Fastenrath, and J. Hajdu, *Introduction to the Theory of the Integer Quantum Hall Effect*. New York: VHC, 1997.

[75] K. von Klitzing, G. Dorda, and M. Pepper, "New method for high-accuracy determination of the fine-structure constant based on quantized hall resistance," *Phys. Rev. Lett.*, vol. 45, pp. 494–497, 1980.

[76] V. Pudalov, A. Punnoose, G. Brunthaler, A. Prinz, and G. Bauer, "Valley splitting in Si-inversion layers at low magnetic fields," *cond-mat/0104347*, 2001.

[77] K. Takashina, Y. Hirayama, A. Fujiwara, S. Horiguchi, and Y. Takahashi, "A silicon bi-layer system," *Physica E*, vol. 22, pp. 72–75, 2004.

[78] K. Takashina, A. Fujiwara, S. Horiguchi, Y. Takahashi, and Y. Hirayama, "Valley splitting control in SiO_2/Si/SiO_2 quantum wells in the quantum hall regime," *Phys. Rev. B*, vol. 69, p. 161304(R), 2004.

[79] K. Takashina, Y. Ono, A. Fujiwara, Y. Takahashi, and Y. Hirayama, "Valley polarization in Si(100) at zero magnetic field," *Phys. Rev. Lett.*, vol. 96, p. 236801, 2006.

[80] T. Kawamura and S. Das Sarma, "Phonon-scattering-limited electron mobilities in $Al_xGa_{1-x}As$/GaAs heterojunctions," *Phys. Rev. B*, vol. 45, no. 7, pp. 3612–3627, 1992.

[81] B. K. Ridley, "The electron-phonon interaction in quasi-two-dimensional semiconductor quantum-well structures," *Journal of Physics C: Solid State Physics*, vol. 15, pp. 5899–5917, 1982.

[82] F. Gamiz, J. B. Roldan, A. Godoy, P. Cartujo-Cassinello, and J. E. Carceller, "Electron mobility in double gate silicon on insulator transistors: Symmetric-gate versus asymmetric-gate configuration," *J. Appl. Phys.*, vol. 94, pp. 5732–5741, 2003.

[83] F. T. Vasko and V. V. Mitin, "Emission of transverse acoustic phonons by two-dimensional electrons due to heterointerface vibrations," *Phys. Rev. B*, vol. 52, pp. 1500–1503, 1995.

[84] B. A. Glavin, V. A. Kochelap, T. L. Linnik, and K. W. Kim, "Electron-phonon interaction via the pekar mechanism in nanostructures," *Phys. Rev. B*, vol. 71, p. 081305, 2005.

[85] F. S. Khan and P. B. Allen, "Deformation potentials and electron-phonon scattering: Two new theorems," *Phys. Rev. B*, vol. 29, pp. 3341–3349, 1984.

[86] R. W. Keyes, "The electronic contribution to the elastic contribution of germanium," *IBM J. Res. Dev.*, vol. 5, pp. 266–278, 1961.

[87] R. W. Keyes, "Electronic effects in the elastic properties of semiconductors," in *Solid State Physics: Advances in Research and Applications* (F. Seitz and D. Turnbull, eds.), vol. 20, pp. 37–90, New York: Academic Press, 1967.

[88] M. Dutoit, "Microwave phonon attenuation measurements in n-type silicon," *Phys. Rev. B*, vol. 3, pp. 453–459, 1971.

[89] A. B. Pippard, "Ultrasonic attenuation in metals," *Philos. Mag.*, vol. 46, pp. 1104–1114, 1955.

[90] A. Sergeev and V. Mitin, "Electron-phonon interaction in disordered conductors: Static and vibrating scattering potentials," *Phys. Rev. B*, vol. 61, pp. 6041–6047, 2000.

[91] S. Das Sarma, J. K. Jain, and R. Jalabert, "Many-body theory of energy relaxation in an excited-electron gas via optical-phonon emission," *Phys. Rev. B*, vol. 41, pp. 3561–3571, 1990.

[92] Y. Shinba, K. Nakamura, M. Fukuchi, and M. Sakata, "Hot electrons in Si(100) inversion layer at low lattice temperatures," *J. Phys. Soc. Jpn.*, vol. 51, pp. 157–163, 1982.

[93] Y. Kawaguchi and S. Kawaji, "A study of electron mobility and electron-phonon interaction in Si MOSFETs by negative magnetoresistance experiments," *Jpn. J. Appl. Phys.*, vol. 21, pp. L709–L711, 1982.

[94] K. Hirakawa and H. Sakaki, "Energy relaxation of two-dimensional electrons and the deformation potential constant in selectively doped AlGaAs/GaAs heterojunctions," *Appl. Phys. Lett.*, vol. 49, pp. 889–891, 1986.

[95] R. Fletcher, V. M. Pudalov, Y. Feng, M. Tsaousidou, and P. N. Butcher, "Thermoelectric and hot-electron properties of a silicon inversion layer," *Phys. Rev. B*, vol. 56, pp. 12422–12428, 1997.

[96] R. J. Zieve, D. E. Prober, and R. G. Wheeler, "Low-temperature electron-phonon interaction in Si MOSFETs," *Phys. Rev. B*, vol. 57, pp. 2443–2446, 1998.

[97] R. Fletcher, Y. Feng, C. T. Foxon, and J. J. Harris, "Electron-phonon interaction in a very low mobility GaAs/$Ga_{1-x}Al_xAs$ δ-doped gated quantum well," *Phys. Rev. B*, vol. 61, pp. 2028–2033, 2000.

[98] X. P. A. Gao, G. S. Boebinger, J. A. P. Mills, A. P. Ramirez, L. N. Pfeiffer, and K. W. West, "Strongly enhanced hole-phonon coupling in the metallic state of the dilute two-dimensional hole gas," *Phys. Rev. Lett.*, vol. 94, p. 086402, 2005.

[99] M. L. Roukes, M. R. Freeman, R. S. Germain, R. C. Richardson, and M. B. Ketchen, "Hot electrons and energy transport in metals at millikelvin temperatures," *Phys. Rev. Lett.*, vol. 55, pp. 422–425, 1985.

[100] M. E. Gershenson, D. Gong, T. Sato, B. S. Karasik, and A. V. Sergeev, "Millisecond electron-phonon relaxation in ultrathin disordered metal films at millikelvin temperatures," *Appl. Phys. Lett.*, vol. 79, pp. 2049–2051, 2001.

[101] J. T. Karvonen, L. J. Taskinen, and I. J. Maasilta, "Observation of disorder-induced weakening of electron-phonon interaction in thin noble-metal films," *Phys. Rev. B*, vol. 72, p. 012302, 2005.

[102] P. B. Allen, "Theory of thermal relaxation of electrons in metals," *Phys. Rev. Lett.*, vol. 59, no. 13, pp. 1460–1463, 1987.

[103] K. Vakili, Y. P. Shkolnikov, E. Tutuc, E. P. D. Poortere, and M. Shayegan, "Realization of an interacting two-valley AlAs bilayer system," *Phys. Rev. Lett.*, vol. 92, p. 186404, 2004.

[104] M. Shayegan, E. D. Poortere, O. Gunawan, Y. Shkolnikov, E. Tutuc, and K. Vakili, "Two-dimensional electrons occupying multiple valleys in AlAs," *cond-mat/0606158*, 2006.

Appendices of this publication are not included in the PDF version. Please order the printed version to get the complete publication (http://www.vtt.fi/publications/index.jsp).

Series title, number and
report code of publication

VTT Publications 666
VTT-PUBS-666

Author(s)
Prunnila, Mika

Title

Single and many-band effects in electron transport and energy relaxation in semiconductors

Abstract

In this Thesis different aspects of band degree of freedom are explored in 2D electron transport and electron-phonon (*e-ph*) energy relaxation in 2D and 3D electron systems. Here the bands of interest are the conduction band valleys of many-valley semiconductors and spatial sub-bands of two-dimensional-electron gas in a quantum well.

The experimental studies of electronic transport focus on double-gate SiO2-Si-SiO2 quantum well field-effect-transistors (FETs), which are fabricated utilizing silicon-on-insulator structures and wafer bonding. Double-gate FETs are intensively explored at the moment due to their prospects in microelectronics. The inclusion of a back gate electrode provides means to adjust the electron wave functions and the occupancy of the spatial 2D sub-bands. The contrast between single and two-sub-band transport is studied in low temperature conductivity/mobility and magneto transport. For example, the conductivity shows significant drop at the threshold of the second spatial sub-band due to inter-sub-band coupling and sub-band delocalization effect is observed at symmetric well potential. At room temperature several sub-bands are inevitably populated and the most relevant observed effect is the mobility enhancement towards symmetric quantum well potential. This mobility enhancement is one of the benefits of double-gate FETs in comparison to similar single-gate FETs.

In the studies of *e-ph* energy relaxation we focus on the case where the phonons cannot directly couple the bands of the electron system. If the e-ph matrix elements depend on the band index then the band degree of freedom plays an important role. We developed a mean field theory, which allows elastic inter and intra-band scattering and also Coulomb interaction. Our model reproduces the long wavelength single-band energy loss rate results found in the literature. In the multi-band regime we find a set of new results, which suggest that the energy loss rate is strongly enhanced if the phonons couple asymmetrically to different bands and the single-band interaction is strongly screened. The effect is tested experimentally in heavily doped n-type Si samples by low temperature heating experiments. We find good agreement between the theory and experiment. Our findings enable a design of a novel electron-phonon heat switch.

ISBN
978-951-38-7065-2 (soft back ed.)
978-951-38-7066-9 (URL: http://www.vtt.fi/publications/index.jsp)

Series title and ISSN	Project number
VTT Publications 1235-0621 (soft back ed.) 1455-0849 (URL: http://www.vtt.fi/publications/index.jsp)	16867

Date	Language	Pages
December 2007	English, Finnish abstr.	68 p. + app. 49 p.

Name of project	Commissioned by

Keywords	Publisher
two-dimensional electron gas, mobility, many-valley systems, electron-phonon interaction, SOI	VTT Technical Research Centre of Finland P.O. Box 1000, FI-02044 VTT, Finland Phone internat. +358 20 722 4520 Fax +358 20 722 4374

Julkaisun sarja, numero ja raporttikoodi

VTT Publications 666
VTT-PUBS-666

Tekijä(t)
Prunnila, Mika

Nimeke

Yhden ja monen vyön ilmiöitä sähkönkuljetuksessa ja elektronien energiarelaksaatiossa puolijohteissa

Tiivistelmä

Työssä tutkitaan elektronien energiavöistä aiheutuvan vapausasteen vaikutuksia 2D-kuljetusilmiöissä ja elektroni-fononi (*e-ph*) -energiarelaksaatiossa 2D- ja 3D-elektronikaasuissa. Tutkimukset keskittyvät lähinnä johtovyön laaksoihin monen vyön puolijohteissa sekä kvanttikaivojen 2D-alivöihin.

Kuljetusilmiöiden kokeelliset tutkimukset keskittyvät erityisesti SiO2-Si-SiO2-kvanttikaivoon perustuvaan kenttäefektitransistoriin (FET), jossa on kaksi hilaelektrodia ja joka on valmistettu SOI-kiekolle suoraliittämistekniikalla. Kaksoishilalliset FET-komponentit ovat tällä hetkellä suuren mielenkiinnon kohteena johtuen niiden potentiaalisista sovelluksista mikroelektroniikassa. Nämä komponentit ovat myös erinomaisia 2D-kuljetusilmiöiden laboratorioita, sillä kaksi hilaa mahdollistavat spatiaalisten alivöiden ja elektronien aaltofunktioiden sähköisen kontrollin. Työssä tutkitaan yhden ja kahden alivyön efektejä matalissa lämpötiloissa. Alivöiden välinen kytkentä heijastuu voimakkaasti Si-kvanttikaivon johtavuuteen ja galvanomagneettisiin kuljetuskertoimiin. Huoneen lämpötilassa useat alivyöt ovat miehitettyinä, ja oleellisin havaittu ilmiö on kokonaisliikkuvuuden kasvaminen, kun kvanttikaivon efektiivinen potentiaali asetetaan symmetriseksi ulkoisilla hiloilla. Havaittu liikkuvuuden kasvaminen on yksi ominaisuus, joka tekee tutkituista FET-rakenteista houkuttelevia sovellusten kannalta.

Elektronien energiarelaksaatiossa tutkimme tapausta, jossa fononit eivät kytke elektronikaasun vöitä. Tällöin vyöindeksillä on merkitystä vain, jos *e-ph*-matriisielementit riippuvat vyöindeksistä. Väitöskirjassa kehitetään *e-ph*-energiarelaksaatioteoria, joka sallii vöiden sisäisen ja vöiden välisen elastisen sironnan sekä varauksenkuljettajien välisen vuorovaikutuksen. Tämä teoria antaa erikoistapauksena kirjallisuudessa esiintyvät yhden vyön tapaukset. Monen vyön tapauksessa havaitaan *e-ph*-relaksaation voimakas kasvu, jos fononit kytkeytyvät asymmetrisesti eri vöihin ja yhdenvyönkytkentä on voimakkaasti varjostettu. Teoriaa testataan kokeellisesti n-tyyppisesti seostetussa piissä lämmittämällä elektroneja matalissa lämpötiloissa. Teoria ja kokeet antavat yhtenevän lämpötilavasteen elektroneille. Löydökset mahdollistavat esimerkiksi uudentyyppisen lämpökytkimen suunnittelun.

ISBN
978-951-38-7065-2 (nid.)
978-951-38-7066-9 (URL: http://www.vtt.fi/publications/index.jsp)

Avainnimeke ja ISSN	Projektinumero
VTT Publications 1235-0621 (nid.) 1455-0849 (URL: http://www.vtt.fi/publications/index.jsp)	16867

Julkaisuaika	Kieli	Sivuja
Joulukuu 2007	Englanti, suom. tiiv.	68 s. + liitt. 49 s.

Projektin nimi	Toimeksiantaja(t)

Avainsanat	Julkaisija
two-dimensional electron gas, mobility, many-valley systems, electron-phonon interaction, SOI	VTT PL 1000, 02044 VTT Puh. 020 722 4520 Faksi 020 722 4374

VTT PUBLICATIONS

Julkaisu on saatavana	Publikationen distribueras av	This publication is available from
VTT PL 1000 02044 VTT Puh. 020 722 4520 http://www.vtt.fi	VTT PB 1000 02044 VTT Tel. 020 722 4520 http://www.vtt.fi	VTT P.O. Box 1000 FI-02044 VTT, Finland Phone internat. + 358 20 722 4520 http://www.vtt.fi

ISBN 978-951-38-7065-2 (soft back ed.) ISBN 978-951-38-7066-9 (URL: http://www.vtt.fi/publications/index.jsp)
ISSN 1235-0621 (soft back ed.) ISSN 1455-0849 (URL: http://www.vtt.fi/publications/index.jsp)